Study of Surface Modified Silicon Nanoparticles for Printable Optoelectronics

Von der Fakultät für Ingenieurwissenschaften, Abteilung Maschinenbau und Verfahrenstechnik der

Universität Duisburg-Essen

zur Erlangung des akademischen Grades

DOKTOR-INGENIEUR

genehmigte Dissertation

von

Anoop Gupta
aus
Kanpur, India

Gutachter: Prof. Dr. rer.-nat. Christof Schulz/ Prof. Dr. Uwe Kortshagen

Tag der mündlichen Prüfung: 27.06.2011

Dedicated to the research community

The process of scientific discovery is, in effect, a continual flight from wonder.

- Albert Einstein

Acknowledgements

Four years ago, I started a journey in the fascinating and colorful world of nano silicon. It was the most memorable and exciting endeavor in my research career. This journey would not have been possible without the support of my supervisors, Prof. Christof Schulz and Dr. Hartmut Wiggers. I would like to give my sincere thanks to them for providing me the chance to do a Ph.D in their research group. Their contribution is invaluable. They assist me in all possible ways to mature myself not only scientifically but also professionally. They always encouraged me to present my work in various conferences around the world and to do collaborative research with other groups. These opportunities helped me to understand the current state-of-the-art and availed me with technical advances.

When I started, I knew almost nothing about silicon nanoparticles. At that time if someone asked me "why silicon nanoparticles are interesting": I could only answer- because it will give me a Ph.D degree. Well, in order to avoid this answer, I started to learn about it from papers and books. Also, I started to collaborate and discuss with people to learn from their experience and generate new ideas. I give my special thanks to Prof. Mark T. Swihart (University at Buffalo, USA) for giving me an opportunity to work in his research group for two months. I gained a lot of hands-on experience on silicon nanoparticles while working there. I am thankful to Prof. Markus Winterer, Prof. Axel Lorke and Prof. Michael Farle in our university for allowing me to do the characterization of particles in their labs. I also thank Prof. Carola Kryschi (Friedrich-Alexander-University Erlangen, Germany) and Prof. Ulrich Simon (RWTH Aachen University, Germany) for giving me an opportunity to do some experiments in their labs.

Although four years have passed, I still feel that it was just yesterday when I started my Ph.D. That is because I had such a great time with my wonderful colleagues and friends in Duisburg. Sonja- It was really fun doing crazy things like taking funny pictures and celebrating April fool with you. You tried to teach me German but finally you learned Hindi ☺. Ashrina, Helge, Nils and Malin– It was great listening your stories about "Tiger". Ali- Thanks for being so kind

and helping me with everything (writing letters in German, solving computer problems….well, it is a long list ☺). Khadijeh- Thanks for being so nice and helpful. It still makes me smile when I remember my discussion with you and Ali about “How evolution will change humans in future”. Ruzica- You are the person, whom I always see first in a conference. Thanks for being so recognizable. I never felt that I went to a wrong venue ☺. Oliver- It was really great to discuss with you about everything under (and in) the sky. Alessandro- Thanks for showing me beautiful Venice and the traditional graduate ceremony in your formal university. Robert- I can´t forget our funny and innovative discussion about the “Ink-jet printing technology” that we had after the workshop in Erlangen. Sebastian- It was a nice experience to supervise your bachelor thesis. Hans- Thanks for helping me with the Glove box connection. Ingo- Thanks for being so friendly and always helpful. Pascal- Thanks for teaching me synthesis and helping me to buy stuffs for my apartment. Barbara (Graft) and Barbara (Nota) ☺- Thanks for helping me with all the administrative work. Natascha and Beate- Thanks for being so nice and helpful with every little thing. Dieter- Thanks for all your lab security seminars and uploading the TEM video. Tim- Thanks for giving the memorable ride from Boston to New York. Ahmed- It was nice to crack jokes with you, Oliver and Alessandro after our lunch breaks. Klemens- Thank you for leaving your plasma reactor for us. Beril (aka Berelium)- It was really great (also tiring ☺) to do TEM of your series of samples. I still have those funny pictures of nanoparticles, which were nano but not nanoparticles.

There were also other people outside my group who directly or indirectly contributed in my research. I am thankful to Ralf and Marina (for helping with HR-TEM), Andreas (for teaching me FTIR), Jens and Matthias (for helping with PL measurement), Ryan (for proving QY data), Horst (for teaching me TEM), Andre (for providing EPR data) and Folarin (for helping me with my experiments at the University at Buffalo).

Worth mentioning names of my friends, Moazzam and Rehan for all those chilled and relaxed evenings. It was fun to discuss our special topics without ever reaching any conclusions. Gautam- Thanks for pushing me to think a short title for my thesis and all the useful discussions we had. Sanjeev- I thank you for motivating me when I was struggling in the lab with my experiments. Sanjubala- Thanks for tolerating us for never ending discussions on physics in your office. Erdal- Thanks for being so helpful with everything. Kartik- Thanks for your help in patiently reading and editing my thesis. Martin- Thanks for helping me to improve my German.

Though, it was always hectic and we could barely manage to practice it. Ahmed Khalil- It was great to work with you in collaboration. I remember those days in Hongkong when we were desperately searching for palatable food. Udo- I always took a chance to pass by your office to see your cheerful face.

Deepti- I really enjoyed your wonderful surprises on my birthdays. Reeta- Thanks for pushing me so hard with my thesis writing and taking some time to read it. It was always fun to argue with you on "Animal Conservation" topic ☺. Mummy and Papa- Thanks for all your constant support and encouragements. Swati and Arun- Thank you for your affection and support. Sangeeta- Thanks for all the funny and relaxing conversations. I hope one day you will be able to convince me to give you a Solitaire.

Hartmut, Ingo and Sonja- Thank you for coming to India to attend my marriage. It is a wonderful memory that we will always cherish ☺.

Last but not least, I would like to thank silicon nanoparticles for allowing me to explore some of their behavior ☺.

"Nanoparticles are really smart"- I lived four years with silicon nanoparticles but I still did not understand them. It's still a long way to go……

Table of contents

List of symbols, abbreviations and acronyms

Latin symbols

a	Lattice parameter
A	Absorbance
A_0	Baseline to peak area of the reference sample
A_1	Baseline to peak area of the hydrosilylated sample
A_c	Cross section area of the pellet
A_{SiHn}	Baseline to peak area of SiH_n absorption
A_{SiOSi}	Baseline to peak area of SiOSi absorption
B	Magnetic field strength
c	Speed of light
d_{hkl}	Interplanar distance
d_p	Mean particle diameter
d_{NP}	Nanoparticle diameter
e	Electronic charge
E	Energy
E_0	Band gap of bulk silicon
E_a	Activation energy
E_g	Band gap
E_D	Activation energy for diffusion

E_F	Functionalization efficiency
E_{PL}	Energy position at the maximum photoluminescence intensity
E_α	Energy of electron in a parallel alignment
E_β	Energy of electron in an antiparallel alignment
f_{osc}	Oscillator strength
$F(\omega)$	Fourier transformation function
g	Spectroscopic splitting factor
h	Planck's constant
I	Transmitted intensity
I_o	Incident intensity
$I(\lambda)$	Spectral irradiation
k	Reaction constant
k_0	Pre-exponential factor
k_b	Boltzmann constant
K	Absorption modulus
L	Crystallite size
m_o	Rest mass of the electron
m_s	Magnetic quantum number
n	Integer number
N	Number density of particles
N_p	Number density of precursor molecules
N_α	Number of electrons with α spins
N_β	Number of electrons with β spins
p	Partial pressure of primary growth species (monomers)

p_s	Equilibrium vapor pressure
r	Radius of cluster
r_{th}	Resolution limit
r^*	Radius of critical cluster
R	Universal gas constant
R_t	Total resistance
R_∞	Degree of reflection
s	Spin quantum number
S	Scattering modulus
S_o	Oxidation susceptibility index
t	Time
t_{et}	Etching time
T	Temperature
T	Transmittance
T_p	Thickness of the pellet
U	Accelerating voltage
V_m	Molar volume
Z	Total impedance
Z'	Real part of total impedance
Z''	Imaginary part of total impedance

Greek symbols

$\Delta E_{\alpha\text{-}\beta}$	Energy difference between α and β spin of electron
ΔE	Spectral width

σ	Specific conductivity
σ	Surface energy
σ_o	Specific conductivity at temperature $0K$
σ_g	Geometric standard deviation
σ_T	Specific conductivity at temperature T
β	Full width at half maximum
β_c	Collision frequency function
τ_c	Characteristic time for coagulation
τ_s	Characteristic time for coalescence
θ	Incident angle
ν	Frequency
$\tilde{\nu}$	Wavenumber
λ	Wavelength
ω	Angular frequency
μ_B	Bohr magneton

Abbreviations and acronyms

BP	Boiling point
BF	Bright field
D-centers	Dangling bonds in a disordered environment
DF	Dark field
EMP	Ethyl-2-methyl-4-pentenoate
EPR	Electron paramagnetic resonance
ETU	Ethyl undecylenate

FFT	Fast Fourier transformation
FTIR	Fourier transform infrared
FWHM	Full width at half maximum
HR-TEM	High resolution transmission electron microscope
IS	Impedance spectroscopy
LED	Light emitting diode
NMR	Nuclear magnetic resonance
P_b-center	Trivalent silicon atoms located at the Si/SiO_x interface
PL	Photoluminescence
PVDF	Polyvinylidene fluoride
QY	Quantum yield
SIMS	Secondary ion mass spectroscopy
STM	Scanning tunneling microscopy
TEM	Transmission electron microscope
TMR	Tunneling magnetoresistance
UV	Ultraviolet
VB	Vinyl benzoate
XRD	X-ray diffraction

1 Introduction

Nanoparticles, which are commonly defined as particles below 100 nm, are the fundamental building blocks of most nanomaterial based devices. Properties of bulk materials are typically constant as a function of size, however, nanomaterials exhibit size dependent physical, chemical, magnetic, electrical and optical properties [1, 2]. Nanomaterials have the potential to profoundly change our economy and to improve our standard of living. Most computer hard drives, for instance, contain giant tunneling magnetoresistance (TMR) heads that, through nano-thin layers of magnetic materials, allow a significant increase in the storage capacity [3, 4]. The use of nanostructure electrode in the lithium ion battery increases its energy capacity compared to conventional lithium ion batteries [5]. Coatings based on titanium dioxide nanoparticles have self cleaning properties [6]. High-power and high-energy storage capacitors can be designed by use of nanostructured carbon as electrode materials [7]. Numerous products featuring unique properties of nanoscale materials are already available in market. According to ScienceDaily [8], new products based on nanomaterials are entering into the market at the rate of 3–4 per week.

Silicon has been a material of great scientific and commercial interest for decades because of its high availability, cost effectiveness, biocompatibility, and compatibility with the well-established silicon-microelectronics technology. High-purity silicon is used in a variety of electronic devices, ranging from computer microchips, transistors, liquid-crystal displays, and semiconductor-based detectors. According to the US Geological Survey, the world's reserves of silicon exceeded five million tons in 2007 — the best indicator of its importance in today's technology [9]. Size reduction of silicon into the nano regime generates novel optical properties and therefore opens the way to new optoelectronic devices. Advanced applications of silicon nanoparticles (Si-NPs) in solar cells [10, 11], silicon laser [12], light emitting diodes (LEDs) [13] and in-vivo applications [14] make silicon a versatile material.

This work has been part of the project "*Study of Surface Modified Silicon Nanoparticles for Printable Optoelectronics*", which is a part of the Research Training Group GRK 1240 "*Na-*

notronics — Optoelectronics and Photovoltaics from Nanoparticles" that focuses on the development of printable optoelectronic devices from nanoparticles. For the manufacturing of silicon nanoparticles (Si-NPs)-based printable optoelectronic devices, the stable colloidal dispersion of particles is desired. Additionally, Si-NPs must provide stable optical and electrical properties in air to be applicable in the desired fields.

The commercial application of Si-NPs demands large quantities of particles. Although Si-NPs have been synthesized using various methods [15-26], gas-phase synthesis offers the possibility to synthesize particles with high production rates. In addition, it provides better control over the process and a ready path to larger scale production. Therefore, in this study, synthesis of Si-NPs is carried out in a gas-phase microwave plasma reactor. By altering the experimental conditions in the reactor (such as microwave power, pressure and precursor concentration), Si-NPs with various size and size distribution were produced.

Silicon is prone to oxidation and as a result a silicon oxide layer is formed around Si-NPs. Lot of surface defects are found at silicon/silicon oxide interface and within silicon oxide [27, 28]. There has been a long debate on the mechanism of light emission from Si-NPs whether it originates from quantum confined silicon or defects on the surface [29-36]. In this study, the photoluminescence (PL) behavior of Si-NPs is examined after removing the surface oxides (and hence most of the surface defects) using HF. In order to distinguish the contribution from the quantum confined effects and surface defects, emission spectra of Si-NPs are investigated during their size reduction (by etching them with a mixture containing HF and HNO_3 [37]) and surface oxidation.

It has been observed that surface oxidation of Si-NPs can deteriorate their optical and electrical properties [25, 38-40]. Additionally, oxygen deficient centers in oxide layer may also cause defect luminescence [35, 36]. In order to have Si-NPs based devices with stable optical and electrical properties, it is highly important to passivate the silicon surface against oxidation. It is reported that the hydrosilylation of silicon surface provides a promising route to stabilize their surface against oxidation as the Si-C bonds formed during this process are very stable in air due to high bond strength and low polarity of bonds [41, 42]. Hydrosilylation of the silicon surface with various organic molecules has been extensively practiced in past [43-51]. Additionally, the efficiency of the functionalization activated by different methods has been examined [52].

From the point of view of long-term stability of particles in air, it is also crucial to understand the effect of organic molecules on the functionalization efficiency and oxidation susceptibility of silicon. In this work, the influence of type of organic ligands on the surface coverage and long-term stability of functionalized Si-NPs is studied.

As the properties of nanomaterials in general are very sensitive to their surface composition, the realization of Si-NPs based optoelectronic devices cannot be accomplished without proper understanding of the effects connected to surface modification. As very few studies have been undertaken to understand the effect of surface modification on the properties of Si-NPs [40, 53], it still remains an open question of both scientific and technological interest that how the modification of silicon surface can alter its optoelectronic properties. In this study, the influence of surface modification on the optical and electrical properties of Si-NPs is examined.

In recent years, the interest in printable electronics has drastically increased because of cost effectiveness and the feasibility of large scale printing even on flexible substrates. Printing of different nanostructured materials such as Ag, Au, CdS and CdSe has been successfully demonstrated [54-59]. However, the printing of Si-NPs has received very little attention [60]. In this study, the functionalized Si-NP ink is used to fabricate thin films on glass substrate using ink-jet printing.

Printing of Si-NPs arrange particles in two- or three dimensions, however, they are not connected to each other. The interconnected particles show different properties compared to individual particles [61-63]. The cross linking of various nanoparticles including Au, Pd and Pt has already been demonstrated in past [62-64]. However, the preparation of cross-linked Si-NPs network has not been realized up to now. In this study, a novel approach to form Si-NPs network by the cross-linking of particles with organic spacer molecules is presented.

Hence, this work alleviates the missing progress in Si-NPs research and opens new avenues in silicon based printable optoelectronic device applications.

2 State of the art

Silicon is the second most abundant element on earth´s crust after oxygen. It has revolutionized our lives by underpinning much of the microelectronics technology. Despite its extreme success in electronics, bulk silicon has not been considered a suitable material for optoelectronic applications due to its poor optical property. This is due to the fact that bulk silicon is an indirect band semiconductor, therefore, the fast non-radiative recombination routes dominate the slower radiative recombination. Because of this reason scientists turned their interest to complex and direct bandgap materials such as GaAs and InP. However, these materials can not be easily integrated with existing silicon microelectronics and therefore are expensive [65]. In 1990, Cahnam discovered that it is possible to get efficient luminescence from nanoporous silicon [66]. This exciting discovery re-evoked intense research interest in silicon because it renewed the hope to integrate light-emitting devices based on silicon with the well-established microelectronics technology.

The quantum confinement model can explain the increased PL from nanosized silicon. According to this model, the localization of the electron wavefunction increases the momentum uncertainty (due to Heisenberg's uncertainty principle) and hence creates some supplement radiative channels via zero-phonon transition that makes silicon a pseudo direct bandgap material [67-71]. Although bulk silicon shows emission in the infrared regime (E_g = 1.17 eV), it has been observed that the emission from red to blue can be obtained from silicon by decreasing its particle size below 5 nm. While some researchers believe that quantum confinement is responsible for different PL emission due to increased band gap with decreasing particle size [29], it is also observed that carrier trapping and recombination at surface silicon-oxygen bonds in oxidized silicon can cause the visible emission [30]. The origin of blue emission from silicon is the most controversial. There are some reports in which authors believe that the blue emission originates from the radiative recombination of excitons in quantum confined silicon, while others believe that oxidation-induced defects at the surface of silicon is responsible for it. For example, Kang and co-workers [72] performed a controlled oxidation of 3 nm silicon quantum dots and tuned

the emission from red to blue. They confirmed that the blue emission originates from the silicon core, as their blue-emitting quantum dots sustained their bright blue emission even after being etched in HF. Wolkin et al. [32] also observed blue emission from porous silicon passivated with hydrogen. Similarly, blue PL from oxide-free, photochemically etched silicon was obtained by Mizuno et al. [33]. Chen and co-workers [34] also suggested that the silicon oxide layer is not responsible for the blue emission in silicon as they observed a change in peak position of blue band upon varying the excitation wavelength. In contrast to these observations, Zhu et al. [35] did not observe any change in peak position of blue PL with increasing annealing temperature and therefore argued that blue PL originates from defect centers. Kim et al. [36] also supported that the defects are responsible for blue emission in silicon. They observed that the oxidation of blue emitting porous silicon does not cause any shift in the PL wavelength. However, in contrast to the observation of Kim et al. [36], Wolkin et al. [32] recorded a red shift in blue emitting porous silicon after surface oxidation. Dovrat et al. [73] studied the luminescence of silicon nanowires and reported that the blue emission originates from the oxide defects of the cladding.

Because the nearly zero dimensional structure (nanoparticles or quantum dots) could have better optical properties compared to two dimensional (quantum well) and one dimensional (nanowire) structures due to increased confinement, scientists started to develop various techniques to synthesize silicon nanoparticles (Si-NPs). For instance, Lwayama et al. [15-17] have carried out the formation of luminescing silicon quantum dots by ion implantation of Si^+ into a silicon oxide matrix with subsequent annealing of the film. These particles show high quantum efficiency [74, 75], however, the major problem with this synthesis is that particles are embedded in the silicon oxide matrix and have a very low production yield. Liquid-phase and inverse micelles routes have also been employed to synthesize Si-NPs [18-24], however, the obvious drawback of this method is the low production yield as well. The gas-phase synthesis of nanoparticles has advantages in terms of high production rates. Li and co-workers [25] synthesized Si-NPs from the laser pyrolysis of silane and reported the production yield of 200 mg/h. Mangolini [26] also reported the production of Si-NPs from the pyrolysis of silane in non-thermal plasma reactor and obtained a production yield up to 50 mg/h. In spite of having very high production rates, it has been observed that freshly synthesized Si-NPs from the gas-phase synthesis show very weak or no luminescence [26, 76]. In case of laser pyrolysis synthesis of Si-NPs, the intense heating of particles probably removes the hydrogen from their surface. It is likely that dangling

bonds formed as a result of hydrogen desorption quench the PL. Researchers have found that particles start to luminesce after the oxidation of Si-NPs in air, which is probably due to the passivation of dangling bonds during surface oxidation. The dangling bonds can trap excitons from radiative recombination pathways and therefore decrease the PL emission. Similar behavior has been observed with Si-NPs synthesized in a gas-phase microwave plasma reactor in our group. Mangolini [26] synthesized particles in a non-thermal plasma, which helped them to obtain H-terminated Si-NPs. Despite having Si-H bonds on the Si-NP surface, the freshly synthesized particles show very weak luminescence. They attributed the weak PL from as-synthesized Si-NPs to the less perfect surface passivation compared to oxidized samples. Oxidation of the silicon surface also leads to the decrease in core size of silicon, and therefore causes the blue shift of the emission peak. However, the oxidation of the silicon surface is a self-limiting process that leads to final stabilization of the PL [26, 76].

It has been observed that the quantum yield of oxidized Si-NPs is not very high. Mangolini [26] reported the quantum yield of air oxidized Si-NPs below 10%. A lot of dangling bonds have been observed at the Si/SiO_x interface in oxidized Si-NPs [77], which can trap excitons from the crystalline silicon core and lead to a low quantum yield from particles. Etching of Si-NPs with HF improves the PL emission from Si-NPs due to removal of the most of the dangling bonds and the formation of a H-terminated surface (as will be discussed in this thesis). Pi et al. [28] observed that oxidation of freshly etched Si-NPs caused the formation of sub-stiochiometric silicon oxide on silicon surface compared to the oxidation of freshly synthesized particles. They found that a smaller ratio of O to Si in the oxides leads to a higher density of defects. As a result, re-oxidized Si-NPs show inferior properties compared to particles oxidized directly after the synthesis.

As the oxidized Si-NPs show poor optical properties compared to H-terminated particles and the oxygen deficient centers in oxide layer may also cause defect luminescence, scientists seek alternative ways to passivate the silicon surface. The surface passivation of Si-NPs with various organic molecules has been extensively examined in past by Fourier transform infrared spectroscopy, x-ray photoelectron spectroscopy and nuclear magnetic resonance spectroscopy [26, 37, 78, 79]. It has been observed that attachment of organic molecules on the silicon surfaces slows down its surface oxidation. Also, the organically capped silicon surface exhibits improved PL quantum yield compared to oxidized Si-NPs [26]. Nelles et al. [40] reported

that the functionalized particles are stable up to 300°C, therefore, they can also be used for higher temperature applications. Reboredo and Galli [53] studied the influence of surface modification on the optical property of Si-NPs. They found that the replacement of hydrogen with alkyl groups on silicon nanoclusters causes a change in their HOMO and LUMO energies. Their calculations suggest that the band gap of H-terminated silicon nanoclusters slightly decreases after alkyl termination.

To underpin the development of silicon based optoelectronic devices, it is also very important to understand and control of the electrical properties of Si-NPs. However, there have been only few reports related to the electrical properties of Si-NPs. This is due to the fact that a large quantity of Si-NPs is needed to form films or pellets for the electrical measurements. The gas-phase synthesis of Si-NPs offers the possibility to synthesize a large quantity of particles. Stegner et al. [38] studied the conductivity of Si-NPs, which were synthesized in a gas-phase microwave plasma reactor via pyrolysis of silane. They dispersed the nanoparticles in ethanol using a ball milling process and thereafter prepared a film of about 500 nm thickness via spin coating. They observed very poor conductivity of the film due to presence of an insulating oxide layer on the surface of the Si-NPs, however, there was an improvement in the electrical conductivity after the removal of the oxides by etching the film with HF. A further increase in conductivity of Si-NPs film has been observed after laser annealing [80]. The annealing increases the electrical contacts between particles due to partial melting and sintering, and therefore enhances the overall conductivity. They have also found that the electrical conductivity of Si-NPs can be further enhanced by doping Si-NPs with phosphorus and boron. However, they did not find any dependence of electrical conductivity with doping concentration up to 10^{18} atoms/cm^3 and thereafter the conductivity increases linearly. The presence of such a critical concentration has been explained with the requirement of a compensation of deep trap states in Si-NPs [77]. The charge compensation does not reduce the number of dangling bonds in Si-NPs, therefore, the increase in conductivity has not been observed up to the critical concentration of dopants. Because of the charge compensation, the effective doping concentration in Si-NPs was found to be at least one order of magnitude lower than the actual doping. However, it has seen that the effective doping concentration in Si-NPs with diameters smaller than 12 nm drops down below three orders of magnitude from the actual doping level. Secondary ion mass spectroscopy (SIMS) investigations on the phosphorus-doped Si-NPs reveal that about 5% of the phosphorus is located in the crystal-

line silicon core, which is probably due to segregation of dopant atoms to the particle surface during particle growth within the reactor and the subsequent oxidation of the highly doped shell. Such segregation was found to be independent of particle size. As the doping of small Si-NPs is very inefficient and etching removes 95% of dopants from Si-NPs, the doping of particles that luminesce in the visible (diameter < 5 nm) is not very advantageous for applications in optoelectronic devices. There is a recent study on the influence of surface modification on the electronic transport of Si-NPs by Nelles and co-workers [40]. They observed that the activation energy of electronic transport, which corresponds to the height of a barrier that an electron must overcome for a hopping event from one particle to the next neighbor, increases after surface oxidation of Si-NPs in air due to the formation of an isolating oxide shell. The removal of the oxide layer by etching of particles with HF decreases the activation energy, however, the functionalization of freshly etched surface with organic molecules further increases it. They have also shown that activation energy of electronic transport depends on the polarity of the organic functional groups.

In recent years, printing technology has attracted considerable attention due to simultaneous deposition and patterning of the different materials necessary to build the layers of an active device on any substrate, preferably without the need of a clean room or post-processing. Additionally, it enables new applications in the field of low cost printable electronic such as transistors [81], solar cells [82] and full color displays [83]. From the point of view of cost, availability, non-toxicity, and potential for integration into existing technologies, a high industrial demand exists on the use of Si-NP inks. However, the printing of Si-NPs has received little attention because of the lack of efficient routes to form stable silicon ink. Si-NPs usually tend to aggregate easily, especially when dispersed in an organic medium. Attaching organic molecules on Si-NPs surface improves its solubility in organic solvents. Liquid-phase synthesis of Si-NPs in the presence of coordinating ligands has advantages in terms of instantly forming stable colloidal dispersions [20], however, these synthesis processes are disadvantageous in terms of low production rates. Unlike wet chemical routes, the plasma-assisted synthesis of Si-NP ink offers the possibility of scale up the production but these particles do not show good optical properties [84].

3 Methodologies

3.1 Synthesis

3.1.1 Microwave plasma synthesis of Si-NPs

3.1.1.1 Background

In a microwave plasma reactor, particle formation and growth take place in the gas-phase. In this approach, gases (such as Ar and H_2) are injected into the reaction chamber and microwave energy is used to generate the plasma. When precursor gas is delivered into the reaction chamber, the decomposition of precursor molecules takes place mostly due to the high temperature of the plasma and a supersaturated vapor of the growth species is formed [85]. If the degree of supersaturation is sufficient, homogeneous nucleation occurs and particles nuclei are formed. Once nuclei are generated, the particles are formed by coagulation and coalescence process. Apart from these processes, undecomposed or partially decomposed precursors take part in the growth of particles by surface reaction. A schematic representation of the different processes in a microwave plasma reactor is shown in Fig. 3.1.

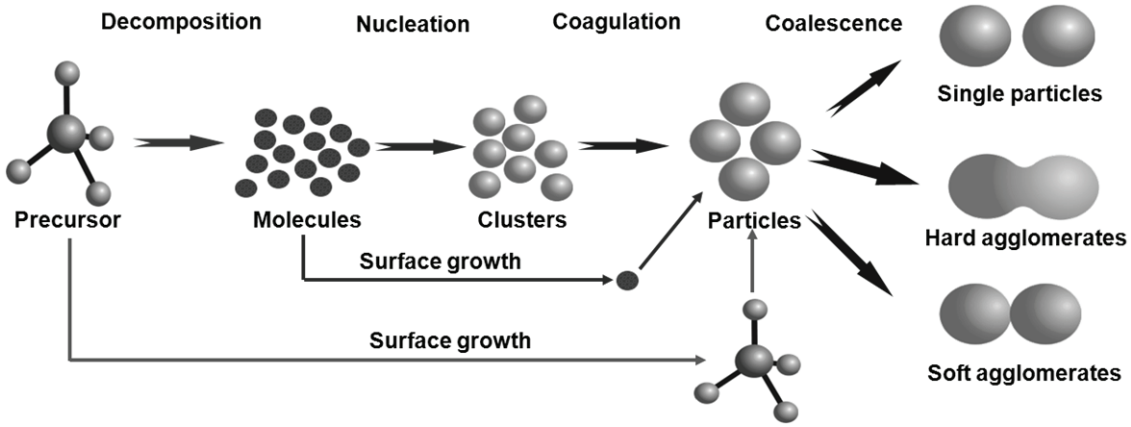

Fig. 3.1. Schematic representation of different processes in a microwave plasma reactor.

For the synthesis of Si-NPs, silane (SiH_4) is used as a precursor gas. The decomposition of silane can be summarized by the following simplified equation [86],

$$SiH_4 \xrightarrow{k} Si + 2H_2 \tag{3.1}$$

The reaction rate can be described by a first-order rate law, which can be written as,

$$\frac{dN_p}{dt} = -kN_p \tag{3.2}$$

where N_p is the number density of SiH_4 molecules and k is the reaction rate constant,

$$k = k_0 \exp\left(-\frac{E_a}{k_b T}\right) \tag{3.3}$$

where k_0 is the pre-exponential factor, E_a is activation energy, T is temperature and k_b is the Boltzmann constant. From shock-tube experiments, the values of k_0 and E_a/ k_b are determined to be $2 \cdot 10^8$ and 14140 K, respectively [87, 88].

After the pyrolysis of precursor, clusters (nuclei) are formed from the supersaturated vapor of primary growth species. Only the clusters with sizes greater than the critical cluster size grow further. The radius of critical cluster (r^*) is given by [89],

$$r^* = \frac{2\sigma V_m}{RT \ln(\frac{p}{p_s})} \tag{3.4}$$

where σ is the surface energy, V_m is the molar volume, R is the universal gas constant, p is the partial pressure of primary growth species and p_s is the equilibrium vapor pressure of clusters of radius r.

The particles inside the reaction chamber collide and stick to each other to form bigger particles. This process is known as coagulation. The characteristic time for coagulation (τ_c) is defined as the time needed to reduce the number density of the particles to half of its initial value and is given by [90],

$$\tau_c = \frac{1}{\beta_c N} \tag{3.5}$$

where β_c is the collision frequency function and N is the number density of particles.

The coagulation is followed by coalescence, which is a strong function of temperature, particle size and material property. The characteristic time for coalescence (τ_s) that is needed to reduce the excess surface area of agglomerate over that of a sphere of the same mass by a factor of 0.63 is given by [91],

$$\tau_s = \frac{T d_{NP}^4}{\sigma D_0 \exp\left(-\frac{E_D}{k_b T}\right)} \tag{3.6}$$

where d_{NP} is the primary particle diameter, E_D is the activation energy for diffusion and D_0 is the diffusion coefficient.

Depending on the characteristic time for coagulation (τ_c) and coalescence (τ_s), either soft agglomerates ($\tau_c \approx \tau_s$), hard agglomerates ($\tau_c < \tau_s$) or non-agglomerated spherical particles ($\tau_c >> \tau_s$) are formed [92].

3.1.1.2 Experimental details

In this synthesis approach, an Ar-SiH_4 gas mixture (1–10% SiH_4 in Ar) was used as a precursor gas. The operating pressure in the reaction chamber was maintained between 1 to 1000 mbar. The microwave generator with frequency of 2.45 GHz and the maximum microwave power of 6000 W was used. After the synthesis, the particles were collected from the filter for further investigations. The results of Si-NPs, synthesized using different experimental conditions, are presented in Sect. 4.1.1.

3.1.2 Etching of Si-NPs

3.1.2.1 Background

If silicon is exposed to air, the surface undergoes oxidation and a thin oxide layer is formed on it. One of the most widely used techniques to remove the oxide layer from the surface of silicon is to etch it with aqueous HF. HF is a weak acid and it does not fully dissociate in the solution. Fur-

thermore, it can dimerize and the dimers can release one proton (H^+). The equilibrium constants between the H^+, F^-, HF_2^- and H_2F_2 species at 25°C are [93, 94],

$$\frac{[H^+][F^-]}{[HF]} = 6.85 \cdot 10^{-4} \text{ mol/m}^3 \tag{3.7}$$

$$\frac{[HF_2^-]}{[HF][F^-]} = 3.963 \text{ m}^3/\text{mol} \tag{3.8}$$

$$\frac{[H_2F_2]}{[HF]^2} = 2.7 \text{ m}^3/\text{mol} \tag{3.9}$$

The etching of silicon surface with HF solution involves the dissolution of silicon oxide and the formation of H-terminated surface. The dissolution mechanism of silicon oxide is proposed by Konotter [95] and schematically presented in Fig. 3.2a. The presence of silanol groups ("A") on the surface of the oxide layer facilitates the etching process, which can be transformed to species "B" after the addition of a proton. The first reaction step involves the elimination of OH^- or H_2O from the surface silanol unit ("A" or "B") and the formation of reactive intermediate "C". The OH^- group is not easy to remove from the surface and the formation of Si^+ intermediate is also not very stable. The H_2F_2 and HF_2^- can assist the elimination of OH^- by coordination with the HF part parallel to the OH side of the silanol group (Fig. 3.2b), which brings the F atoms of H_2F_2 or HF_2^- close to the silicon atom. Therefore, the elimination and addition reaction take place consecutively and the reaction product "D" is formed. Monofluorides, such as HF and F^-, are not able to do this. Furthermore, HF_2^- ions are more reactive than H_2F_2 because the F-H-F angle is larger in the HF_2^- ion than in the square shaped H_2F_2 molecule. The larger angle brings the F^- ion closer to the reactive site. After the Si-F unit is formed, three subsequent nucleophilic substitution reactions will break SiF_4 units out of the silicon oxide matrix and bring the surface back into its initial form ("E"), where silanol group unit has to be replaced by a Si-F unit to continue the etching process. After complete dissolution of the oxide layer, an F-terminated silicon surface is formed.

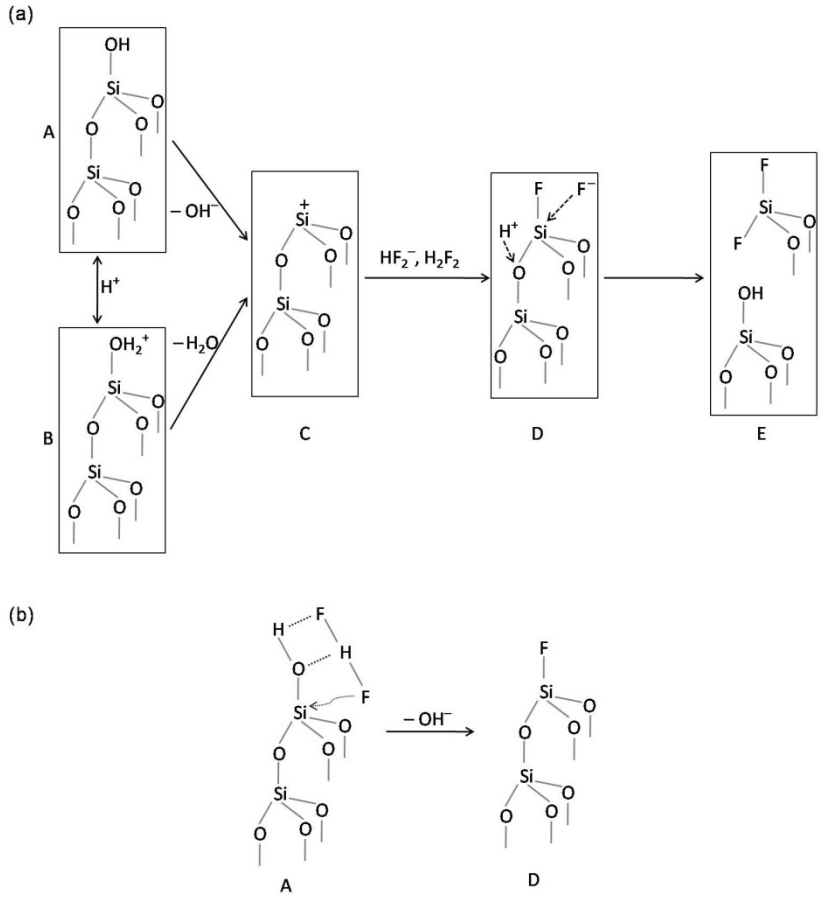

Fig. 3.2. (a) Reaction mechanism of the dissolution of silicon oxide in aqueous HF. (b) HF_2^- assisted OH^- elimination reaction with consecutive F^- addition.

The F-terminated silicon surface, which is formed after the dissolution of the oxide layer during etching with HF, is followed with the formation of H-terminated surface. The mechanism of H-termination from F-terminated surface is schematically depicted in Fig. 3.3 [96, 97]. The initial stage of the surface after complete removal of the oxide layer is shown in (A). Due to ionic nature of the Si-F bond, positive charge (δ+) is induced on the attached silicon atom and negative charge (δ-) on the second layer of silicon. This polarization allows the insertion of HF into the Si-Si bond leading to fluorination of the surface silicon and hydrogenation of second layer of silicon (B). The increasing fluorination of the SiF_2 group over SiF makes the silicon more electropositive and thereby increasing its proclivity with F^-. This leads to the formation of SiF_3 (C), which further increases the positive charge on silicon and enhances the propensity of F^- for the next attack. As a result, the H-terminated silicon surface is formed with the removal of surface silicon atoms as SiF_4 (D).

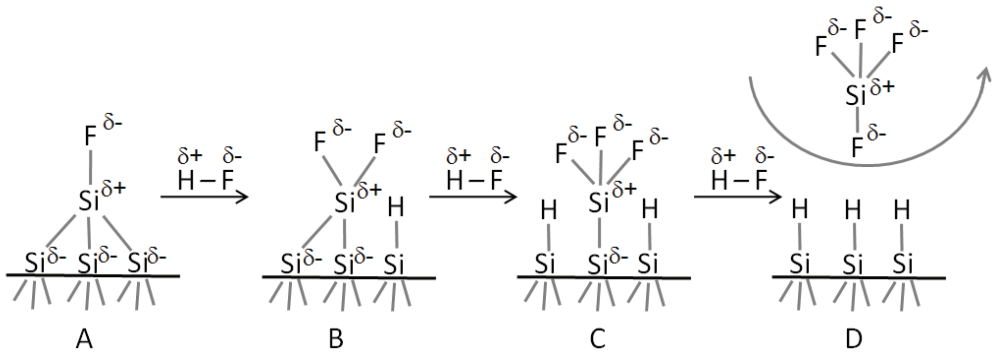

Fig. 3.3. Schematic representation of the formation of H-terminated silicon surface.

3.1.2.2 Experimental details

In this work, the etching of Si-NPs was carried out with HF in a glove box under a dry nitrogen atmosphere. In a typical experiment, 40 mg of as-synthesized Si-NPs were dispersed into 5 ml of methanol using mild sonication and thereafter they were etched inside the glove box with 10 ml of HF (49 wt. %). The dispersion was stirred for about 5 min at room temperature and then the particles were filtered on a polyvinylidene fluoride (PVDF) membrane filter (pore size 0.1 μm). For the size reduction of Si-NPs, a mixture containing HF (10 ml, 49 wt. %) and HNO_3 (1 ml, 69 wt. %) was added to the suspension of Si-NPs in methanol. The solution was vigorously stirred during the process to achieve homogeneous etching. The etching procedure was stopped by diluting the solution with methanol and immediate filtration of particles on a filter. After the filtration, particles were rinsed with HF and dispersed in a solvent. Thereafter, the suspension was transported from the glove box to the measurement setup within an airtight glass bottle in order to avoid air exposure. The experimental results of etched Si-NPs are presented in Sect. 4.1.2.

3.1.3 Surface functionalization of Si-NPs

3.1.3.1 Background

Attaching molecular layers on silicon surface has been the focus of much attention due to its ability to control the chemical, electrical and optical properties of the underlying silicon. Chemical properties, such as polarity or hydrophilicity can be tuned by engineering the functional

group attached to silicon surface [43, 98-100]. Electrical properties such as conductance through silicon-based circuits can be modulated with the absorption of unique organic molecules [101]. Additionally, it is seen that that the organic group on silicon surface alter its energy band and therefore change its optical properties [53].

Attachment of organic molecules can be carried out on the oxidized as well as H-terminated silicon surfaces [102-104]. The oxide layer on silicon surface is not desired for certain applications (e.g. solar cells) due to its insulating nature. Also, the formation of organic monolayer on the oxidized surface separates the underlying crystalline silicon from any functionality placed on the top. Hydrosilylation of H-terminated silicon surface with alkene or alkynes is one of the most effective and delicate method to synthesize organosilicon compounds as it allows the attachment of the chemical functionalities directly to the silicon through a Si–C bond.

The mechanism of hydrosilylation of silicon surface with alkenes is schematically presented in Fig. 3.4 [104]. The H-terminated silicon surface that is obtained directly after HF etching is shown in (A). The reaction starts with a homolytic cleavage of the surface Si-H bonds, which can be achieved by several methods such as free radical initiators, thermal energy (thermally induced hydrosilylation) and UV light (photoinitiated hydrosilylation). Due to homolytic cleavage of the surface Si-H bond, a silicon dangling bond is formed (B). The silicon dangling bond is believed to react with the C=C bond of an alkene to form the Si-C bond and leaving a β-CH radical on the immobilized organic molecule (C). Thereafter, the remaining carbon based radical abstracts hydrogen from the neighboring Si-H group (D) and the new silicon dangling bond allows the hydrosilylation reaction to proceed. This mechanism has been verified by a number of experimental studies. For example, scanning tunneling microscopy (STM) has been used to directly observe the growth of molecular island formation around isolated reaction initiation sites [105, 106]. Additionally, studies using deuterated silicon (with surface Si-D bonds) have shown that as the reaction proceeds, deuterium incorporation into the organic film (as C-D) occurs [106]. The white light activated hydrosilylation reaction based on the absorption of a photon from the silicon crystal, formation of an exciton and interaction of the free exciton with an alkene is also proposed [104].

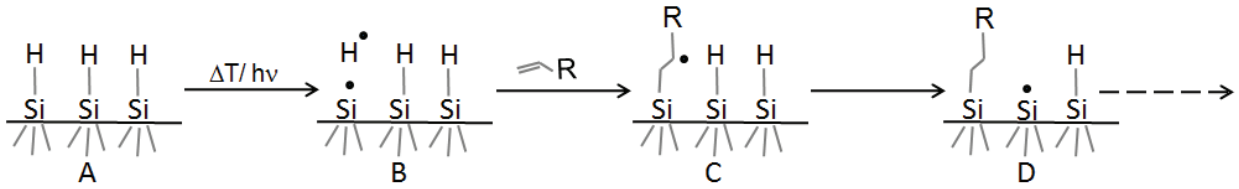

Fig. 3.4. Reaction mechanism for hydrosilylation of a H-terminated silicon surface with alkene.

Hydrosilylation of flat single crystalline silicon, porous silicon and Si-NPs surface has been extensively practiced in past. For example, Linford et al. [43] prepared a high-quality alkyl monolayers on Si(111) surface by reaction of alkenes and alkynes with the H-terminated silicon upon free-radical initiation with diacyl peroxides. Similar work has been done by Sieval et al. [99] to prepare stable Si-C linked functionalized monolayers on the H-terminated Si(100) surface. Fabre et al. [44] derivatized the Si(111) surface with a thiophene-terminated alkyl monolayer for preparing a conducting film. Buriak et al. [45] and Boukherroub et al. [46] coated H-terminated surfaces of Si(111) and porous silicon with alkenyl and alkyl functionalities in the presence of Lewis acid catalysts. They also conducted thermal reactions of alcohols and aldehydes with Si(111)-H to form Si-OH_2R films [47] and used UV irradiation to link ethyl undecylenate to Si(111) surface [48]. Schmeltzer et al. [49] prepared alkenyl- and alkyl-terminated surfaces by hydride abstraction with triphenylcarbenium cations in the presence of terminal alkynes and alkenes. Derivatization of porous silicon by Grignard reagents at room temperature was done by Kim et al. [107]. Stewart et al. [50, 51] applied white-light promoted reactions for hydrosilylation of alkenes and alkynes on silicon nanocrystals. Nelles et al. [52] showed the modification of free standing Si-NPs surface with thermal-, radical-, Lewis acid- and UV induced hydrosilylation and compared their hydrosilylation efficiency.

3.1.3.2 Experimental details

In the present work, surface functionalization of H-terminated Si-NPs was carried out by photoinitiated or thermally induced hydrosilylation with alkenes. For this purpose, freshly etched Si-NPs were dispersed in 5 ml of alkene inside a nitrogen filled glove box directly after filtration and the suspension was transported outside the glove box within an airtight glass bottle in order to avoid air exposure. Thereafter, the surface functionalization was accomplished by either exposing the above dispersion to UV light (photoinitiated hydrosilylation) or heating in an oil bath

(thermally induced hydrosilylation). The wavelength of UV light and the temperature used for functionalization is mentioned in each section of the results and discussion part separately. In photoinitiated hydrosilylation, the alkene and Si-NPs dispersion was exposed from all directions with UV light. A triangular shaped UV reactor, containing two NU81-254 nm/366 nm VWR UV light source at each triangular position, was used for this purpose. However, the surface functionalization of particles discussed in Sect. 4.2.2.1 was carried out using a Rayonet photochemical cylindrical reactor equipped with 16RPR-254 nm UV tubes. The dispersion was stirred continuously during the UV exposure/heating in oil bath for homogeneous reaction.

3.1.4 Ink-jet printing of Si-NPs

3.1.4.1 Background

A piezoelectric ink-jet printer was used for the printing of Si-NPs as schematic depicted in Fig. 3.5. The printer operates in drop-on-demand mode, where an acoustic pulse ejects ink droplets from a reservoir through a nozzle. In piezoelectric ink-jet printers, the deformation of piezoelectric material causes a sudden volume change and hence generates an acoustic pulse. The pressure wave in the ink chamber propagates to the nozzle orifice, where a droplet is ejected. To eject the droplet, the energy of the pressure wave should be greater than the surface tension energy of the droplet.

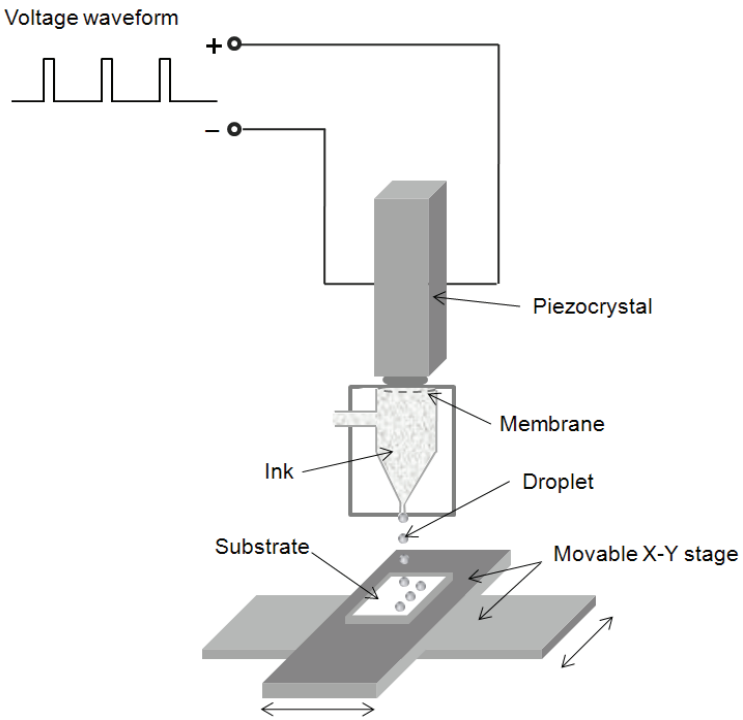

Fig. 3.5. Schematic diagram of piezoelectric ink-jet printer [108].

3.1.4.2 Experimental details

In the present study, a colloidal dispersion of functionalized Si-NPs in ethyl undecylenate was used to fabricate films on glass substrates using a piezoelectric Dimatix 2800 ink-jet printer. This printer can create and define patterns over an area of about 200 × 300 mm^2 and handle substrates up to 25 mm thick with an adjustable vertical height. Prior to printing, the glass substrates were cleaned in piranha solution (3:1 volumetric mixture of sulfuric acid and hydrogen peroxide) for 30 min followed by rinsing several times in water and dried in a stream of nitrogen. A very low concentration of particles in the ink (~ 0.4 wt. %) was prepared with a viscosity of 2.3 mPa/s and a surface tension of 31 mN/m. The cartridge was filled with 1.5 ml of Si-NPs dispersion and the droplet volume jetted from the cartridge was equal to 10 picoliter. The printing was carried out at 13 V and a frequency of 3 kHz. The substrate temperature was set at 60°C and multiple layers of Si-NPs were printed on the substrate in a layer-by-layer fashion. The computer controlled print head was moved in two dimensions to write structures on the substrate. There was a 10 min delay between two successively printed layers.

3.2 Characterization

3.2.1 X-ray diffraction (XRD)

3.2.1.1 Background

X-ray diffraction (XRD) is a characterization technique by which the arrangement of atoms within a crystal can be determined. Additionally, it can also provide other information about the material such as average crystallite size and residual stress. XRD is based on the phenomenon of the wave interferences, in which two electromagnetic waves with the same wavelength travelling in the same direction can either reinforce or cancel each other depending on their phase difference.

X-ray beam incident on a crystalline solid is diffracted by the crystallographic planes as illustrated in Fig. 3.6. According to Bragg law, the diffracted beam shows constructive interference if the following relation is satisfied,

$$2d_{hkl} \sin\theta = n\lambda \tag{3.10}$$

where d_{hkl} is the spacing between diffracting planes with Miller indices (*hkl*), θ is the incident angle, λ is the wavelength of x-ray and n is an integer number. The spacing between planes with Miller indices (*hkl*) are related to the lattice parameter of the crystal structure. For example, for a cubic crystal structure with lattice constant a, the relationship is given by,

$$d_{hkl} = \frac{a}{\sqrt{h^2 + k^2 + l^2}} \tag{3.11}$$

Combining equations (3.10) and (3.11), the following relationship is obtained,

$$\sin^2\theta = \frac{\lambda^2}{4a^2}(h^2 + k^2 + l^2) \tag{3.12}$$

This equation predicts, for a particular incident wavelength λ and a particular cubic crystal of unit cell with size a, all the possible Bragg angles at which diffraction can occur from plane (*hkl*).

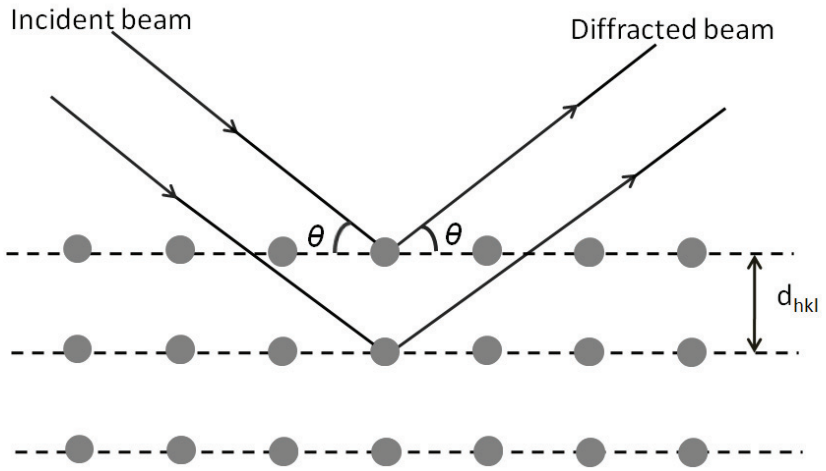

Fig. 3.6. Diffraction of x-rays from crystal planes. The dotted lines and solid circles represent the crystal planes and atom positions in a crystal, respectively.

In a powder material, all the diffraction directions of the lattice can be attained by varying the incident angle due to the random orientation of the powdered material. A spectrum of diffraction intensity versus the angle between incident and diffracted beam (2θ) is recorded by changing the incident angle (θ) of the x-ray beam. These relative intensities coupled with 2θ values can be assigned to a specific material, thus it is used as a material characterization technique. Furthermore, the crystallite size (L) of the material can be calculated from the full width at half maximum (FWHM) (β) of the diffraction peaks using Scherrer's equation,

$$L = \frac{0.9\lambda}{\beta \cos\theta} \tag{3.13}$$

Note that the average crystallite size of particle may differ from the mean particle size as it only gives the information about the ordered domains.

Rietveld refinement is a technique to analyze XRD data, which calculates the intensity profile using a model (I^{calc}) and refines it until it matches with the measured profile (I^{exp}). For this purpose a weighted profile R-factor (R_{wp}) is defined to compare the difference between the model and the measured data [109],

$$R_{wp} = \sqrt{\frac{\sum_{i=1}^{N}\left[w_i\left(I_i^{\exp} - I_i^{calc}\right)\right]^2}{\sum_{i=1}^{N}\left[w_i I_i^{\exp}\right]^2}} \tag{3.14}$$

where w_i is equal to $(I_i^{exp})^{-0.5}$. The value of R_{wp} indicates the quality of the fit. The lower the value of R_{wp}, the better the agreement between the model and the measured data.

3.2.1.2 Experimental details

In this study, the crystalline structure and crystallite size of Si-NPs were determined by XRD using a PANalytical x-ray diffractometer (X´Pert PRO). The diffractometer is equipped with Ni-filtered Cu-K_α (1.54 Å) x-ray radiation source operated at 40 kV and 40 mA. The diffraction data (2θ = 20° to 120°) were analyzed by Rietveld refinement with the help of the MAUD program [109].

3.2.2 Transmission electron microscopy (TEM)

3.2.2.1 Background

Transmission electron microscopy (TEM) is a powerful technique to investigate the crystallographic structure, defects, interfaces and grain boundaries as it provides resolution down to the atomic level. The transmission electron microscope functions similar to a light microscope. The main difference is that the electrons are focused on a substrate with the aid of the electromagnetic lens in the TEM instead of glass lenses for visible light in a light microscope. In TEM, the electrons are generated either by thermionic emission (e.g. electrically heated LaB_6 filament) or by field emission (e.g. tungsten filament). In thermionic emission, the electrons are generated by heating the cathode filament to a high temperature. If the thermal energy is sufficiently high that electrons can overcome the work function, then the electrons can leave the material. In field emission, electrons tunnel out of the material when an intense field is applied to it, therefore, it requires a very sharp, needle-shaped cathode.

In TEM, image contrast arises because of the scattering of the incident beam by the sample. The electron wave can change both the amplitude and phase as it transverses the sample, and both kinds of change give rise to image contrast. In TEM different types of contrasts can be arise, such as diffraction contrast, mass-thickness contrast and phase contrast. Coherent elastic interaction of electrons with crystalline object produces diffraction contrast in the TEM image. The mass-thickness contrast arises from incoherent (Rutherford) elastic scattering of electrons. A phase contrast image requires the selection of more than one beam (two or more beams). The contrast in image is formed by either constructive or destructive interference of beams.

TEM can be used in different imaging modes. These modes can be chosen by selecting either the undiffracted beam or the diffracted beam or both (Fig. 3.7). If the objective aperture is selected such that it only allows the direct beam to pass, a bright field (BF) image is formed. If the diffracted beam is only allowed to pass through the objective aperture, a dark field (DF) image is formed. Mass thickness and diffraction contrast contribute to the image in these modes. Areas belonging to crystalline regions selecting their Bragg beams appear with bright contrast in DF mode and dark in BF imaging mode. A high resolution TEM (HR-TEM) image is formed by allowing the directed beam together with diffracted beams through the aperture. In HR-TEM, only phase contrast contributes to the image.

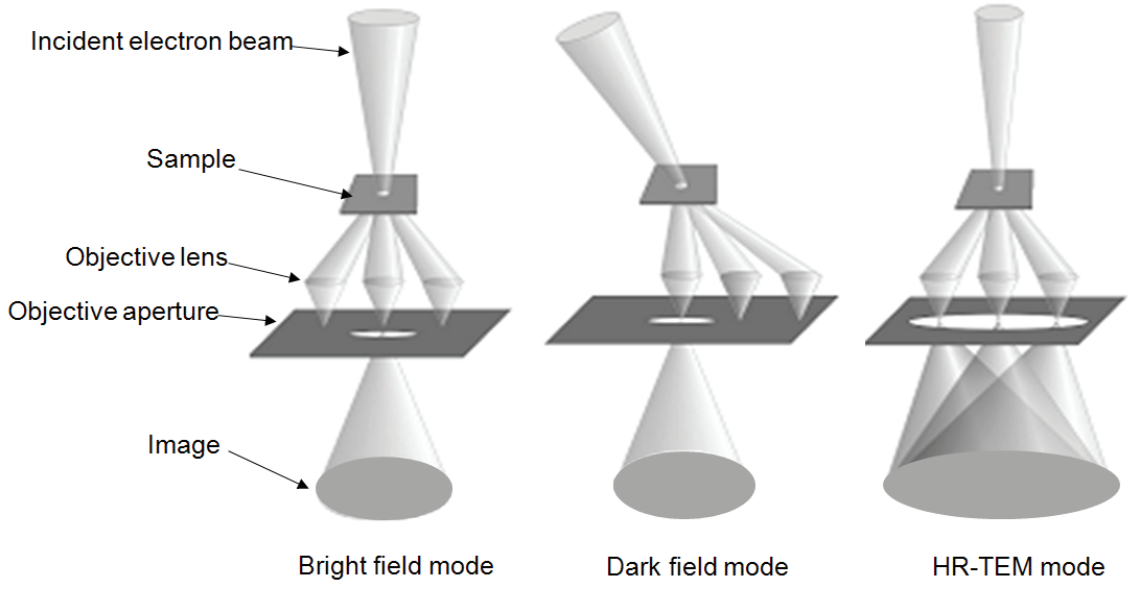

Fig. 3.7. Schematic illustration of the formation of bright field image (left), dark field image (middle) and HR-TEM image (right). Reproduced from [110].

3.2.2.2 Experimental details

In the present work, the crystallinity, size, shape and morphology of Si-NPs were analyzed by using conventional TEM (Philips CM-12, operating at 120 kV) and HR-TEM (Philips CM-20, operating at 200 kV). Samples for TEM were prepared by immersing the carbon-coated copper grids into a dispersion of the Si-NPs in methanol/chloroform, followed by evaporation of the solvent.

3.2.3 Impedance spectroscopy (IS)

3.2.3.1 Background

Impedance spectroscopy (IS) is a technique to study electrical properties of a material. In this process, an electrical AC stimulus (a known AC voltage or current) is applied to a material (deposited between two electrodes) and the corresponding response (voltage or current) is analyzed [111]. It is assumed that the properties of electrode-material system are time invariant. Several methods exist to induce stimuli for impedance measurement. However, the most common approach involves the measurement of impedance directly in the frequency domain by applying a single-frequency AC voltage to the interface. The measurements can be performed over a wide frequency range from mHz to MHz. Each measurement is consequently followed by measuring the phase shift as well as the amplitude of the resulting signal at that frequency.

The electric transport through a percolation network of Si-NPs (e.g. a compressed powder) can be represented by a simplified sketch as shown in Fig. 3.8a. The total impedance measured from Si-NPs pellets should come from three different contributions; particle-electrode contact, particle core and particle-particle contacts. Figure 3.8b shows the equivalent circuit diagram of different contributions of impedance. The resistors R_c account for the contribution of the core of Si-NPs, whereas, the particle-particle contacts can be represented by a resistor $R_{p\text{-}p}$ and a capacitor $C_{p\text{-}p}$ in parallel. Similarly, the particle-electrode contact can be represented by a resistor $R_{p\text{-}e}$ and a capacitor $C_{p\text{-}e}$ in parallel. A typical representation of the total impedance (Z) is composed of a real part (Z′) and an imaginary part (Z′′). If the real part is plotted on the horizontal axis and the imaginary part on the vertical axis, this representation is called “Nyquist plot”.

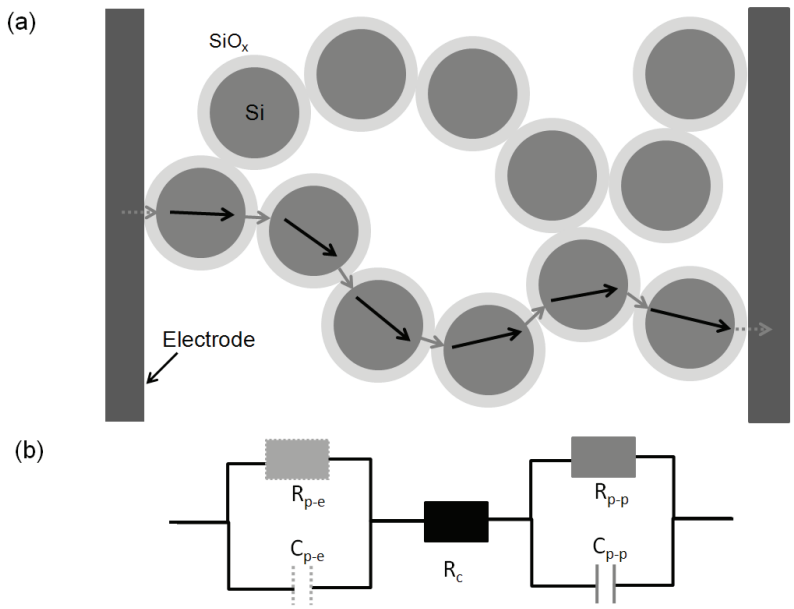

Fig. 3.8. (a) A schematic representation of electric transport through Si-NPs, and (b) the equivalent AC circuit diagram of different contributions of impedance.

3.2.3.2 Experimental details

In this study, the electrical conductivity of Si-NPs was measured with an impedance spectrometer (HP 4192A) in the frequency range between 10 Hz and 10 MHz with 20 frequency points per decade. For the measurements, thin pellets of Si-NPs were prepared by pressing about 10 mg of the powder uniaxially into thin pellets of 5 mm diameter using a hydraulic press and applying a force of 20 kN for 30 min. The thickness of the pellet is about 0.2 mm and the green density turned out to be about 60% of bulk density. The compressed pellets were sandwiched between two platinum disks and mounted in the measurement cell between two platinum electrodes. The diameter of the compressed pellets exactly matches the diameter of the platinum disks to prevent the short cuts between the disks. The complete measurement setup consists of the measurement cell (Fig. 3.9), which was placed into a gas-tight ceramic tube with gas inlet and outlet at its ends. The ceramic tube was heated in a temperature-controlled tube furnace to adjust the temperature of the sample. The impedance measurements were performed in hydrogen (Air Liquide 5.0) and argon (Air Liquide 5.0) atmospheres. For the temperature dependent conductivity, pellets were heated from 100 to 400°C with a step size of 25°C and the impedance was measured at each temperature point after the temperature has stabilized. Each sample did undergo three ramp

cycles. The first ramp was performed for annealing the sample under hydrogen atmosphere. Then the pellet was allowed to cool down to 50°C in the same atmosphere and thereafter the second and third ramp were performed to collect and verify the data, respectively.

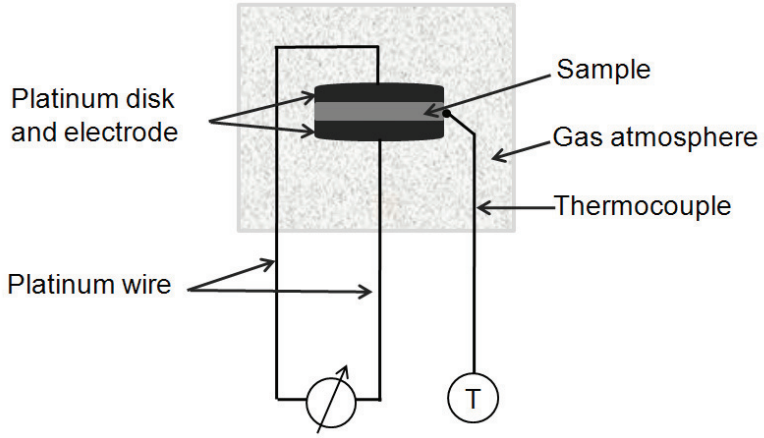

Fig. 3.9. A schematic representation of the measurement setup for impedance spectroscopy.

3.2.4 Fourier transform infrared (FTIR) spectroscopy

3.2.4.1 Background

Infrared spectroscopy is based on the phenomenon of infrared absorption due to molecular vibrations. When a molecule is irradiated by electromagnetic waves within the infrared frequency range, one particular frequency may match the vibration frequency of the molecule. Consequently, that frequency is absorbed by the molecule to excite the molecular vibration. In infrared spectroscopy, the electromagnetic waves are characterized by the wavenumber $\tilde{\nu}$ which is defined as the reciprocal of wavelength λ and in the unit of cm^{-1},

$$\tilde{\nu} = \frac{1}{\lambda} \tag{3.15}$$

The energy E of the electromagnetic wave can be given by,

$$E = \frac{hc}{\lambda} = h\nu \tag{3.16}$$

where ν is the frequency of electromagnetic wave, h is the Planck´s constant and c is the speed of light. Therefore, the wavenumber can also be expressed as,

$$\tilde{\nu} = \frac{\nu}{c} = \frac{E}{hc} \tag{3.17}$$

It is clear from the above expression that the wavenumber is directly proportional to the energy of the electromagnetic wave. The infrared spectrum ranges from 4000 to 400 cm^{-1}.

Fourier transform infrared spectroscopy (FTIR) is an infrared spectroscopy technique in which the Fourier transformation method is used to obtain an infrared spectrum in the whole range of wavenumber simultaneously. It differs from the dispersive method, which entails creating a spectrum by collecting signals at each wavenumber separately. The principle of FTIR is based on the Michelson interferometer, as schematically illustrated in Fig. 3.10. The infrared beam splits into two beams by a beam splitter. The two beams strike a fixed mirror and a moving mirror, respectively. The recombination of the two beams caused interference before passing the sample. The function of the moving mirror is to change the path length between two split beams. The two beams show constructive and destructive interference periodically with continuous change in the path length. The plot of sum of all interference intensity, created by each wavelength in the beam, as a function of optical path difference is called interferogram. The Fourier transformation is performed by a computer to convert the interferogram into an infrared spectrum. The Fourier transformation between a function in time (t) domain and its corresponding one in the frequency (ω) domain is given by,

$$F(\omega) = \frac{1}{\sqrt{2\pi}} \int_{-\infty}^{\infty} f(t) e^{-i\omega t} dt \tag{3.18}$$

The Fourier transformation converts the intensity versus the optical path difference to the intensity versus the wavenumber. The optical path difference can be considered to be in the time domain because it is obtained by multiplying time with the speed of a moving mirror. The wavenumber can be considered in the frequency domain as it is equal to the frequency divided by the speed of light.

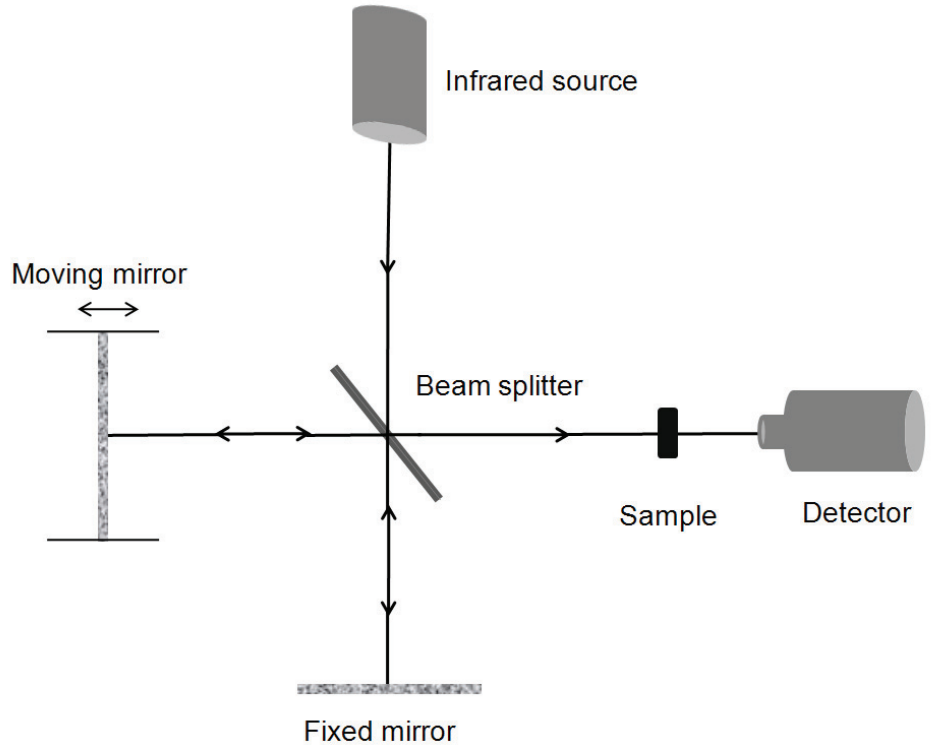

Fig. 3.10. Schematic diagram of a FTIR spectrometer with a Michelson interferometer.

The vertical axis in the FTIR spectrum is often presented by the transmittance T or the absorbance A. The transmittance is the ratio of intensities transmitted by the sample (I) to the incident intensity I_o,

$$T = \frac{I}{I_o} \tag{3.19}$$

The transmission if often expressed as %T. The absorbance can be calculated from the transmittance using following relationship,

$$A = -\log_{10} T \tag{3.20}$$

The diffuse reflectance method is primarily used to acquire the infrared spectra of powders and solids with rough surface. The description of diffuse reflectance is based on a one dimensional model, where the optical properties of the sample are given by two relevant constants, i.e. the absorption and the scattering coefficients. This phenomenon is accounted by the Kubelka-Munk equation [112],

$$f(R_\infty) = \frac{(1-R_\infty)^2}{2R_\infty} = \frac{K}{S} \tag{3.21}$$

where K denotes the absorption modulus, S is the scattering modulus and R_∞ is the degree of reflection on the sample with sufficient thickness that no radiation reaches the back surface.

3.2.4.2 Experimental details

In the present work, FTIR measurements on Si-NPs were carried out at room temperature using a Bruker IFS66v/S spectrometer. The spectra were measured in the wavenumber range from 800 cm^{-1} to 3100 cm^{-1}. An average of 100 scans was acquired at a spectral resolution of 2 cm^{-1}. The measurements in transmission mode were performed by making thin pellets of potassium bromide (KBr) and Si-NPs mixture. The mixture was prepared by spreading a few drops of chloroform dispersion of Si-NPs onto a mortar and blending with KBr powder after the evaporation of chloroform. The diffused reflectance measurements were performed directly on dry powders. FTIR spectra of functionalized Si-NPs were taken after separating the particles from their respective alkene solution by centrifugation, subsequent washing with methanol and drying in vacuum.

3.2.5 Electron paramagnetic resonance (EPR) spectroscopy

3.2.5.1 Background

Electron paramagnetic resonance (EPR) spectroscopy is based on the interaction between electromagnetic radiation and magnetic moment of electrons. In this method, the resonance absorption of microwave radiation by paramagnetic molecules or ion centers, containing at least one unpaired electron, is studied in the presence of a magnetic field.

The basic physical concepts of EPR are analogous to those of nuclear magnetic resonance (NMR), but it is electron spins that are excited instead of spins of atomic nuclei. Every electron has a magnetic moment and spin quantum number $s = 1/2$, with magnetic components $m_s = +1/2$ and $m_s = -1/2$. In the presence of an external magnetic field, the magnetic moment of electron aligns itself either antiparallel ($m_s = +1/2$) or parallel ($m_s = -1/2$) to the field. This effect is called Zeeman effect. The antiparallel and parallel alignments correspond to the higher energy

(E_α) and lower energy (E_β) state, respectively (Fig. 3.11). The energy separation $\Delta E_{\alpha\text{-}\beta}$ between parallel and antiparallel alignments depends on the magnetic field B according to the following equation,

$$\Delta E_{\alpha-\beta} = E_\alpha - E_\beta = g\mu_B B \tag{3.22}$$

where μ_B is the Bohr magneton and g is called g-factor (spectroscopic splitting factor). For an electron in vacuum, g is equal to 2.00232 [113].

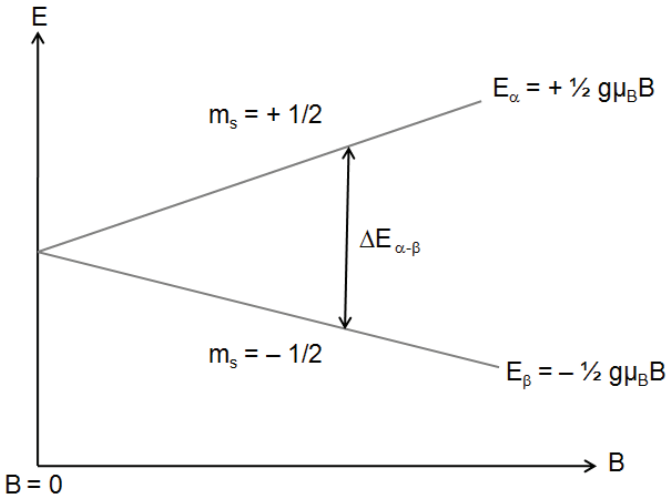

Fig. 3.11. Energy-level diagram for a single electron in vacuum as a function of external magnetic field.

In thermal equilibrium, the α and β states are distributed in such a way that more electrons are in the lower state. The ratio between number of α spins (N_α) and number of β spins (N_β) depends on temperature and is given by the Boltzmann distribution law,

$$\frac{N_\alpha}{N_\beta} = \exp\left(-\frac{\Delta E_{\alpha-\beta}}{k_b T}\right) = \exp\left(-\frac{g\mu_B B}{k_b T}\right) \tag{3.23}$$

where k_b is the Boltzmann constant and T is the absolute temperature. When the sample is placed in a magnetic field and microwave radiation with frequency ν is applied, then the electron spin in the β state absorbs this energy if the energy of the microwave radiation ($h\nu$) coincides with the energy difference between α and β,

$$h\nu = g\mu_B B \tag{3.24}$$

where h is Planck's constant and ν is the frequency of the microwave radiation. The equation (3.24) suggests that two possible ways for performing EPR experiment as illustrated in Fig. 3.12. The first method consists of placing a spin ensemble in a constant magnetic field B_o and irradiating the sample with a linearly variable frequency (Fig. 3.12a). When the frequency matches the resonance conditions for the magnetic field B_o, microwave radiation is absorbed and the absorption is revealed by a microwave detector. In an alternative way, the sample is irradiated with a constant microwave frequency (ν_o) in a linearly variable magnetic field (Fig. 3.12b). When the magnetic field reaches the resonance condition, the microwave radiation is absorbed. In practice, the measurements are performed by keeping the microwave frequency constant and recording its absorption by varying the magnetic field.

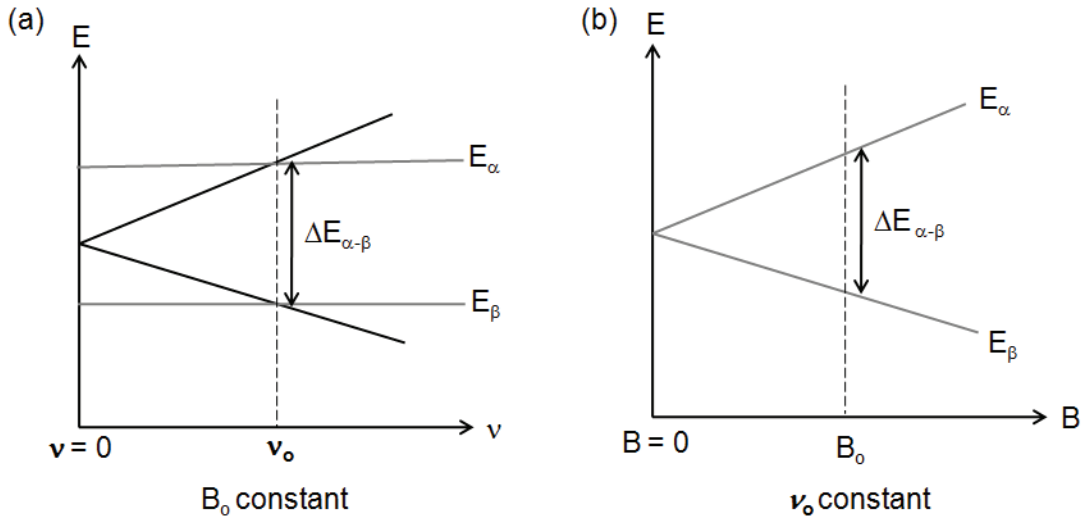

Fig. 3.12. Two alternative ways to measure the EPR spectrum: (a) placing the sample in a constant magnetic field and varying the microwave frequency, and (b) irradiating the sample with a constant microwave frequency in a linearly variable magnetic field.

3.2.5.2 Experimental details

In the present study, the EPR measurements on Si-NPs were performed at room temperature with a conventional continuous wave X-band spectrometer and a TE_{102} cavity (Bruker). For EPR measurements, about 1 mg of particles were filled into small teflon tubes which were then placed in a conventional Suprasil quartz EPR sample holder. A lock-in amplifier was used for the detection of the EPR signal with a modulation of the magnetic field at 100 kHz. All spectra were normalized to the mass of the sample.

3.2.6 Photoluminescence (PL) spectroscopy

3.2.6.1 Background

Photoluminescence (PL) is the emission of radiation induced by the optical excitation of a substance with an external source of light. The PL emission from nanosized silicon has been extensively studied in past [114-118]. Meier et al. [114], developed a model to compute the PL emission spectra of Si-NPs from a given size distribution. They observed that the oscillator strength, which is proportional to the recombination rate of excitons, increases with increasing PL emission energy due to strong confinement in smaller nanoparticles. The energy dependence of the oscillator strength (f_{osc}) for Si-NPs is given by,

$$f_{osc} = 1.4 \cdot 10^{-6} + 5.80 \cdot 10^{-8} \exp\left(\frac{E_g}{0.332} \right) \tag{3.25}$$

where E_g is electronic band gap of Si-NP in eV. According to Deleure et al. [119], the particle size-dependent band gap of Si-NPs can be written as,

$$E_g = E_0 + \frac{3.73}{d_{NP}^{1.39}} \tag{3.26}$$

where E_0 is the electronic band gap of bulk silicon in eV and d_{NP} is the diameter of Si-NP in nm. By introducing the effect of size dependent change in the lattice parameter of Si-NPs on the band gap, Ledoux et al. [120] proposed a modified size dependent band gap for Si-NPs,

$$E_g = E_0 + \frac{3.73}{d_{NP}^{1.39}} + \frac{0.881}{d_{NP}} - 0.245 \tag{3.27}$$

Meier et al. used equation (3.26) to calculate the size dependence of the oscillator strength,

$$f_{osc} = 1.4 \cdot 10^{-6} + 1.7 \cdot 10^{-6} \exp\left(\frac{11.24}{d_{NP}^{1.39}} \right) \tag{3.28}$$

For the particle size distribution, they assumed a lognormal size distribution,

$$\frac{dn(d_{NP}, d_p, \sigma_g)}{dd_{NP}} = \frac{1}{\sqrt{2\pi}} \frac{1}{d_{NP} \ln \sigma_g} \exp\left(-\frac{\ln^2 d_{NP} / d_p}{2 \ln^2 \sigma_g} \right) \tag{3.29}$$

where d_p is the mean particle diameter and σ_g is the geometrical standard deviation. Assuming that each nanoparticle at room temperature acts as an inhomogeneous broadened emitter with a spectral width of ΔE, which is in the order of few meV,the PL intensity of a single particle (I_{NP}) with a peak emission energy of E_g can be given by,

$$I_{NP}(h\nu, E_g, \Delta E) \propto \frac{1}{\Delta E\sqrt{2\pi}} \exp\left(-\frac{(h\nu - E_g)^2}{(2\Delta E)^2}\right) \tag{3.30}$$

The PL emission of a nanoparticles ensemble with mean particle diameter d_P and geometrical standard deviation σ_g is given by,

$$I(h\nu) = \int_0^\infty f_{osc}(d_{NP}) \frac{dn(d_{NP}, d_p, \sigma_g)}{dd_{NP}} I_{NP}(h\nu, E_{g,\Delta E}(d_{NP}))dd_{NP} \tag{3.31}$$

It has been shown that measured PL spectra of Si-NPs and those calculated using above model fit nicely with each other [114].

3.2.6.2 Experimental details

In this study, different PL measurements on Si-NPs were performed at room temperature using either a Nd:YAG laser as an excitation source operated at a wavelength of 532 nm, or a diode laser operated at wavelength of 405 nm or a Perkin-Elmer LS 50 fluorescence spectrometer with 350 nm excitation. All the PL measurements were done at room temperature. All photographs of luminescing Si-NPs were taken by exposing them with the UV lamp (λ = 366 nm).

3.2.7 Photoluminescence quantum yield (QY)

3.2.7.1 Background

The photoluminescence quantum yield (QY) gives the efficiency of the photoluminescence process. It is defined as the ratio of the number of photons emitted to the number of photons absorbed.

$$\text{QY} = \text{number of photons emitted/ number of photons absorbed} \tag{3.32}$$

3.2.7.2 Experimental details

In order to measure the quantum yield of colloidal Si-NPs, a blue LED (λ = 390 nm) was used to excite the sample. First, the baseline PL measurement was performed using pure solvent in which the particles were dispersed. The baseline measurement only shows the excitation peak of the blue LED at 390 nm. In the second step, the PL of colloidal Si-NPs was measured, which has a reduced intensity of the excitation peak at 390 nm due to absorption by Si-NPs and a PL emission peak. For the calculation of QY, the integration of the excitation and luminescence spectra was performed. The following quantities were obtained,

$$L_{s,b} = \int_{\text{excitation}} \lambda I(\lambda) d\lambda \tag{3.33}$$

and,

$$P_{b,s} = \int_{\text{luminesce}} \lambda I(\lambda) d\lambda \tag{3.34}$$

where $I(\lambda)$ is the spectral irradiation and λ is the wavelength. The subscript s and b denote the sample and the baseline, respectively. If there is no luminescence signal in the baseline measurement ($P_b = 0$), then the quantum yield can be calculated using following equation [121],

$$\text{QY} = \frac{P_s}{-(L_s - L_b)} \tag{3.35}$$

4 Results and discussion

4.1 Synthesis and surface modification of Si-NPs

In this section, the synthesis of Si-NPs using a microwave plasma reactor is presented. Additionally, the influence of etching and surface functionalization on the structural and surface properties of Si-NPs is examined.

4.1.1 Synthesis of Si-NPs

The microwave plasma reactor used for the synthesis of Si-NPs is schematically depicted in Fig. 4.1. The synthesis setup mainly consists of a quartz tube, microwave source and the gas delivery system. Along with the diluent gases (Ar and H_2), the precursor gas (SiH_4 in Ar) is injected coaxially into the reaction chamber. The quartz tube is mounted within the microwave cavity, where the microwave energy is coupled with gases and forms plasma. The decomposition of the precursor takes place within the plasma, which eventually forms Si-NPs by nucleation and growth processes (see Sect. 3.1.1 for details).

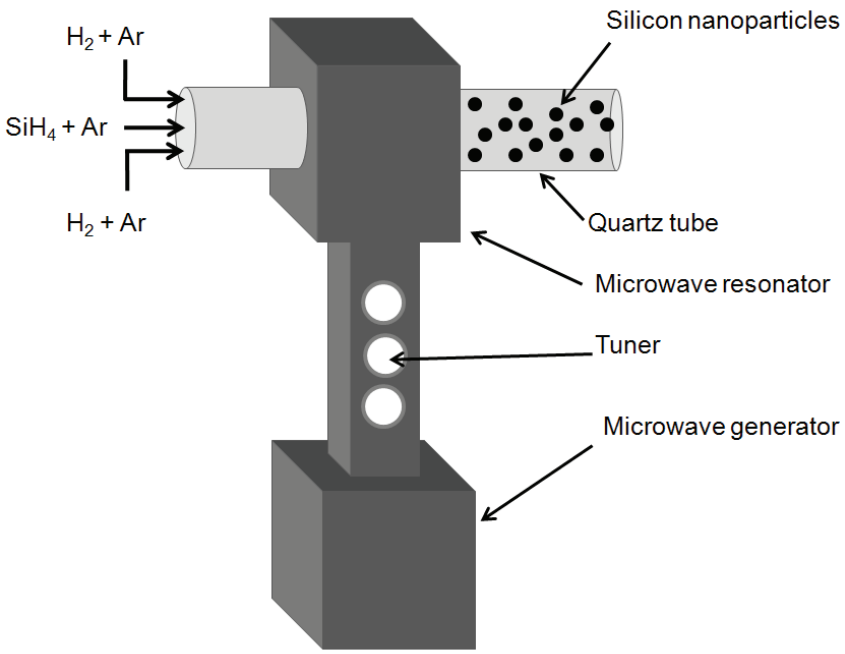

Fig. 4.1. Schematic diagram of experimental setup for the synthesis of Si-NPs in a microwave plasma reactor.

With this synthesis approach, single crystalline Si-NPs can be synthesized with high production rates (0.1–10 g/h). The size of the Si-NPs can be tailored by changing the total gas pressure in the reaction chamber, SiH_4 concentration and the microwave power. The influence of these parameters on the size of Si-NPs has been reported previously [122]. For the present research, Si-NPs with the following experimental conditions were synthesized,

Experimental condition I:

Microwave power (W)	1800
Total gas pressure (mbar)	200
SiH_4 concentration (ppm)	15873

Experimental condition II:

Microwave power (W)	1500
Total gas pressure (mbar)	40
SiH_4 concentration (ppm)	260

Experimental condition III:

Microwave power (W)	900
Total gas pressure (mbar)	20
SiH_4 concentration (ppm)	4195

The TEM images of Si-NPs synthesized using the experimental condition I are shown in Fig. 4.2. It is clear from the TEM images that the particles have spherical and facetted morphologies (Fig. 4.2a). The lattice fringes in the HR-TEM images indicate that particles are crystalline in nature. Due to surface oxidation, the Si-NPs are covered with a roughly 1-2 nm thick oxide shell, as manifested by the amorphous layer around the crystalline core. Due to collision of particles inside the reaction chamber, soft and hard agglomerated particles can be formed (Fig. 4.2a, Fig. 4.2b). Additionally, the particles can be aggregated outside the reactor upon oxidation due to formation of wrapping oxide shell around softly agglomerated particles as revealed in Fig. 4.2c. The particles have a very broad size distribution. The particle size distribution was measured from the TEM images with the help of image processing software Digital Micrograph. The size distribution of particles was found to fit well to a lognormal size distribution with mean particle diameter (d_p) of 52 nm and geometric standard deviation (σ_g) of 1.5 (Fig. 4.2d).

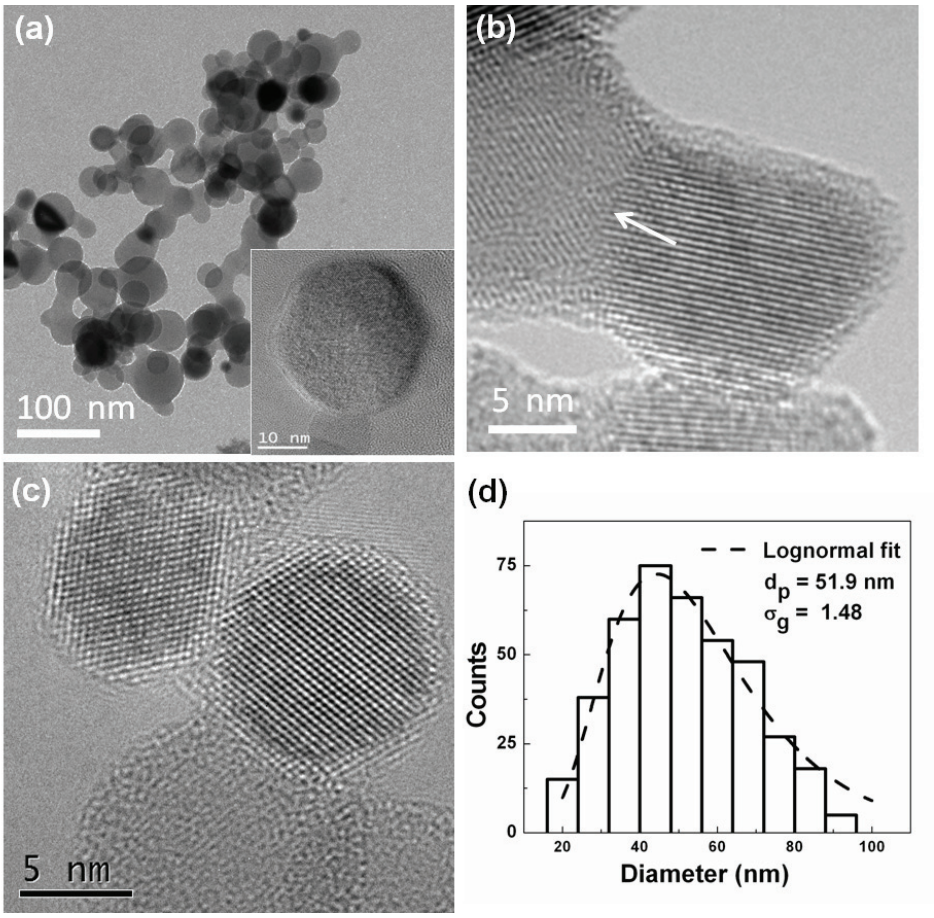

Fig. 4.2. (a) Bright field TEM image of as-synthesized Si-NPs. Inset is an HR-TEM image of non-agglomerated particle covered with an amorphous oxide shell on the circumference. (b) The HR-TEM image shows the grain boundary of agglomerated crystalline particles (indicated by an arrow). (c) The HR-TEM image reveals the agglomeration of particles due to the formation of an oxide layer. (d) Histogram of the particle size distribution of as-synthesized Si-NPs.

The crystal structure and crystalline size of as-synthesized Si-NPs is determined by XRD. The measured XRD pattern of as-synthesized Si-NPs with their miller indices is shown in Fig. 4.3 The diffraction data (2θ = 20° to 120°) were analyzed by Rietveld refinement using the program MAUD [109]. The findings reveal that as-synthesized Si-NPs are crystalline in nature and have a diamond cubic structure. The calculated average crystalline diameter of as-synthesized Si-NPs is 75.4±0.2 nm, which is different from the mean particle diameter calculated from the TEM image analysis. The deviation of particle size determined by TEM and XRD can be explained in terms of different quantities assessed by two different techniques. For example, the XRD measurement gives crystalline size of the particles, whereas the size distribution calculated from the TEM image analysis also includes particles with amorphous structure and

amorphous surface layers. Additionally, small particles are difficult to distinguished in agglomerates from TEM and big particles are overemphasized in XRD measurement [123].

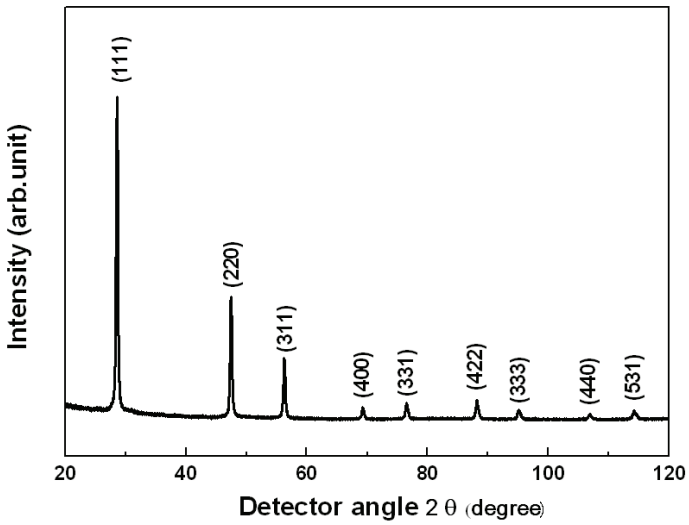

Fig. 4.3. XRD pattern of as-synthesized Si-NPs. The Bragg peaks are labeled with their Miller indices.

TEM images of Si-NPs synthesized using the experimental conditions II are shown in Fig. 4.4. These particles are crystalline in nature and have an apparent spherical shape. The Fast Fourier Transformation (FFT) analysis (Fig. 4.4c) of the HR-TEM image (Fig. 4.4b) reveals that the Si-NPs have diamond structure with a lattice parameter of 0.557±0.003 nm. A statistical analysis of 735 Si-NPs gives a lognormal particle size distribution with d_p of about 13.2 nm and σ_g of 1.4 (Fig. 4.4d).

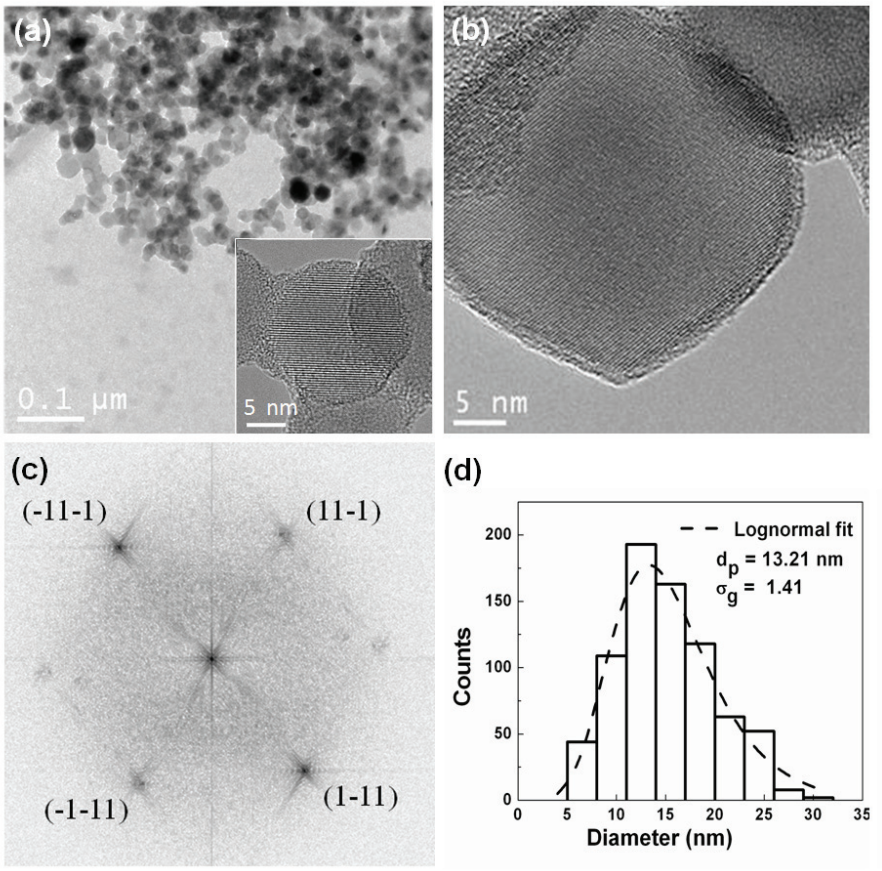

Fig. 4.4. (a) Bright field TEM image of as-synthesized Si-NPs, inset shows an HR-TEM image of particle with spherical morphology. (b) HR-TEM image of a particle with facetted surface. (c) FFT pattern of the HR-TEM image of particle shown in (b). (d) Histogram of the particle size distribution of as-synthesized sample.

The TEM images of Si-NPs synthesized using the experimental conditions III are shown in Fig. 4.5. These images reveal that particles have almost spherical morphology. The lattice fringes clearly manifest the crystalline nature of Si-NPs (Fig. 4.5c). The white contrast in the dark field image of the sample (Fig. 4.5b) is coming from Si-NPs that exactly fulfill the Bragg condition, further establishing that particles are crystalline. From the lognormal fit of the particle size distribution of particle, the measured values of d_p and σ_g are 4.3 nm and 1.2, respectively (Fig. 4.5d).

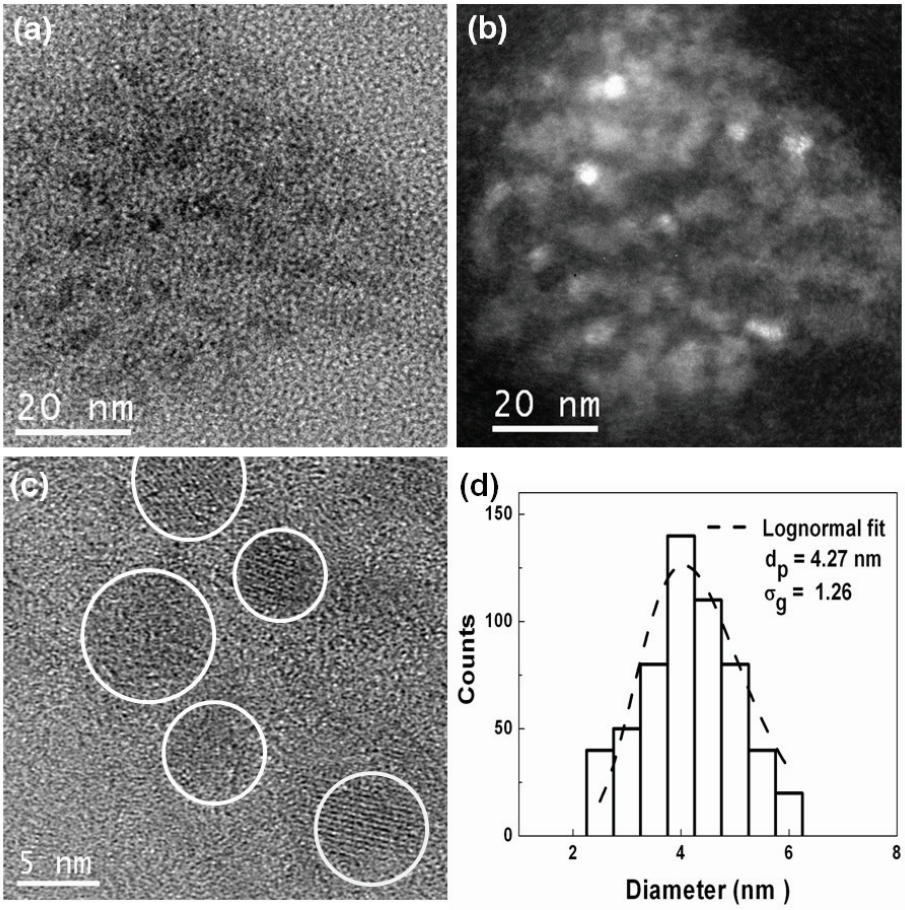

Fig. 4.5. (a) Bright field TEM image, (b) dark field TEM image, (c) HR-TEM image, and (d) histogram of the particle size distribution of as-synthesized Si-NPs.

4.1.2 Etching of Si-NPs

For the hydrosilylation reaction, the surface of Si-NPs must be H-terminated (see Sect. 3.1.3). As the surface of Si-NPs is covered with an oxide shell due to oxidation of particles in air, the particles are etched with HF in order to produce H-terminated surfaces. The mechanism of the formation of H-terminated silicon surface during HF etching is discussed in Sect. 3.1.2. If the particles are etched with a mixture containing HF and HNO_3, the size of the particles can also be reduced. During etching, the HF etches the oxide layer from the silicon surface and HNO_3 oxidizes the freshly etched silicon surface in parallel. Therefore, the size of Si-NPs can be tuned by varying the etching time. After etching, the particles were also washed with HF in order to make sure that H-terminated surface is produced. Schematic representations of etching of Si-NPs with

HF and with a mixture containing HF and HNO_3 are presented in Fig. 4.6. The details of the experimental procedure are given in Sect. 3.1.2.

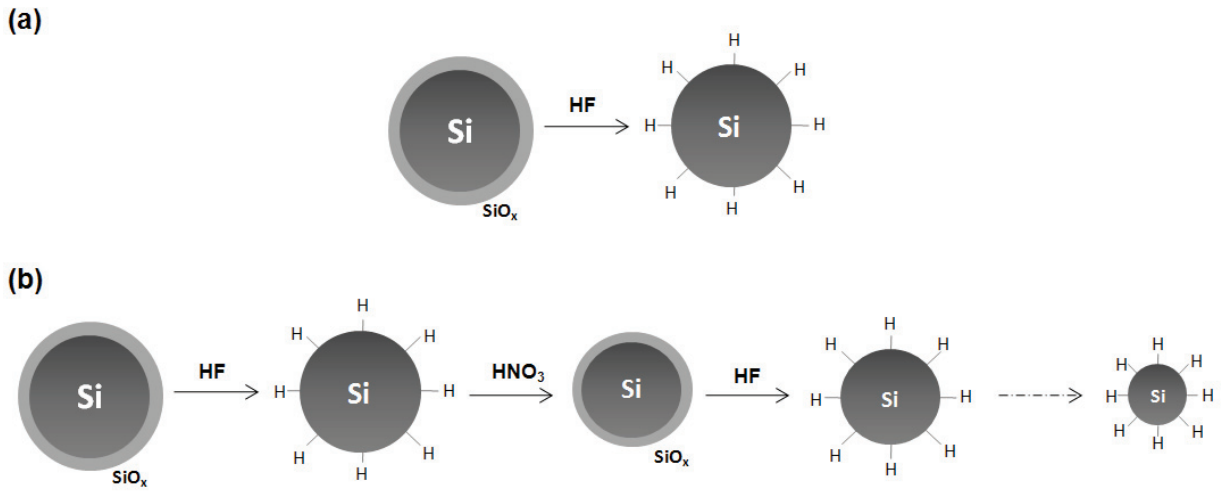

Fig. 4.6. (a) Schematic representation of etching of Si-NPs with HF, and (b) sequential size reduction of Si-NPs during the etching with HF and HNO_3 mixture.

The FTIR spectra of Si-NPs before and after HF etching are shown in Fig. 4.7. Etching of Si-NPs with HF and HNO_3 mixture gives almost the similar spectrum as obtained after HF etching. A schematic diagram of all vibration modes present in Si-NPs are shown in Fig. 8.1 of Appendix A [124]. The FTIR spectrum of as-synthesized Si-NPs shows signals from SiOSi stretching vibration around 1100 cm^{-1} [125-127], SiH_2O_2 stretching mode at 2205 cm^{-1} [128], $SiHO_3$ stretching mode at 2260 cm^{-1} [128], and $SiHO_3$ bending mode at 877 cm^{-1} [129]. These oxide modes in the spectrum of as-synthesized Si-NPs are present because the particles were stored in air for months. Small intensities of SiH_n (n = 1, 2, 3) stretching vibration around 2100 cm^{-1} [125, 130] are observed as well. This indicates that there are still some hydrogenated silicon present on Si-NPs surface that have not been attacked by oxygen. The appearance of the SiH_2 scissor mode at 908 cm^{-1} [125] together with the increased intensity of SiH_n stretching mode in the FTIR spectrum of the etched sample confirms that the etching process terminates the surface with hydrogen. A small intensity of SiOSi stretching mode is also observed in the spectrum of the etched particles, which likely arises due to brief air exposure of the sample before the FTIR measurement. The structure of this peak is significantly different from that of the as-synthesized sample. The SiOSi peak in the as-synthesized sample is very broad and consists of two peaks at 1060 cm^{-1} and 1190 cm^{-1}. Whereas the etched sample shows only one sharp peak around 1090 cm^{-1}. The

vibration energy of SiOSi vibration peak depends on the stoichiometry of silicon and oxygen in silicon oxide [127]. Therefore, the different peak positions of SiOSi vibration in etched and as-synthesized sample indicate the presence of SiO_x with different values of x. It is reported that in the initial stage of oxidation mostly surface oxides are formed, which is related to oxygen insertion between the first and second layer of the silicon surface. The surface oxide peak of the Si-OSi vibration lies around 1060 cm^{-1}. As the air exposure time increases, the bulk oxides are formed due to the diffusion of oxygen into the inner layers. The increased diffusion of oxygen causes the emergence of a bulk SiOSi peak at higher energy position (1180 cm^{-1}) along with the increased signal from surface oxides at 1060 cm^{-1} [125]. Hence, the formation of bulk oxides together with surface oxides in as-synthesized Si-NPs due to their long air exposure causes the broadening of the SiOSi peak. This result is in very good agreement with previous observations [131, 132].

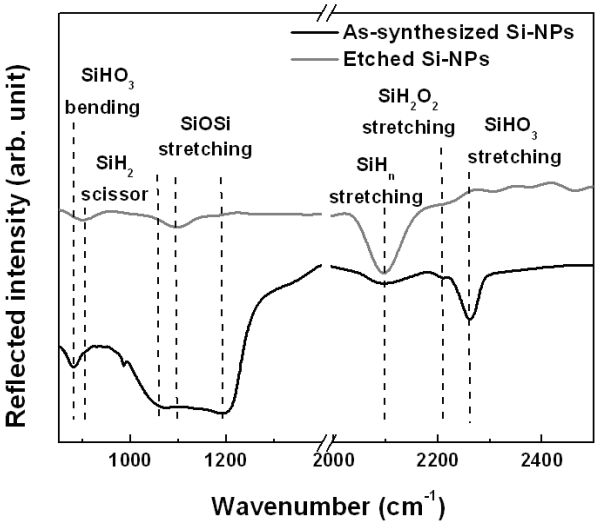

Fig. 4.7. FTIR spectra of as-synthesized and etched Si-NPs.

4.1.3 Surface functionalization of Si-NPs

After the etching, the surface of H-terminated (freshly etched) Si-NPs was terminated with organic molecules using photoinitiated/thermally induced hydrosilylation process (see Sect. 3.1.3 for experimental details). The hydrosilylation reaction occurs by homolytic cleavage of Si-H bonds on the surface of Si-NPs and the formation of Si-C bonds with the C=C bond of alkenes.

The surface functionalization of H-terminated Si-NPs using hydrosilylation with alkene is schematically illustrated in Fig. 4.8. The mechanism of hydrosilylation is discussed in Sect. 3.1.3.

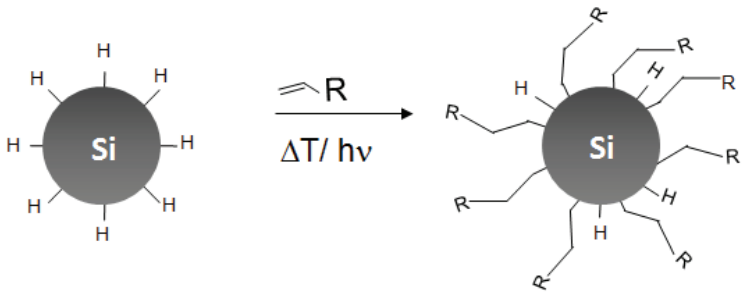

Fig. 4.8. A schematic representation of surface functionalization of H-terminated Si-NPs using photoinitiated/thermally induced hydrosilylation with alkene.

Figure 4.9 shows the FTIR spectra of dodec-1-ene functionalized Si-NPs together with dodec-1-ene molecules. Along with some characteristic peaks of dodec-1-ene molecules, a clear signal of SiH_n stretching vibration around 2100 cm^{-1} is seen in the spectrum of functionalized Si-NPs. This shows that not all Si-H bonds on the silicon surface were replaced by alkyl groups as the initially attached alkyl groups on the silicon surface provide an increasing steric hindrance for further attachment of organic molecules. Additionally, small intensities of SiOSi vibration mode around 1080 cm^{-1} and a $SiHO_3$ stretching vibration around 2260 cm^{-1} are observed in the spectrum. The oxides are supposed to form due to oxidation of Si-NPs surface during functionalization because of the moisture and dissolved oxygen present in the reactants. The CH_y stretching modes (C-CH_3 asymmetric stretching at 2958 cm^{-1}, C-CH_2 asymmetric stretching at 2925 cm^{-1} and C-CH_2 symmetric stretching at 2856 cm^{-1}) [133] originate from the attached alkyl ligands on silicon surface.

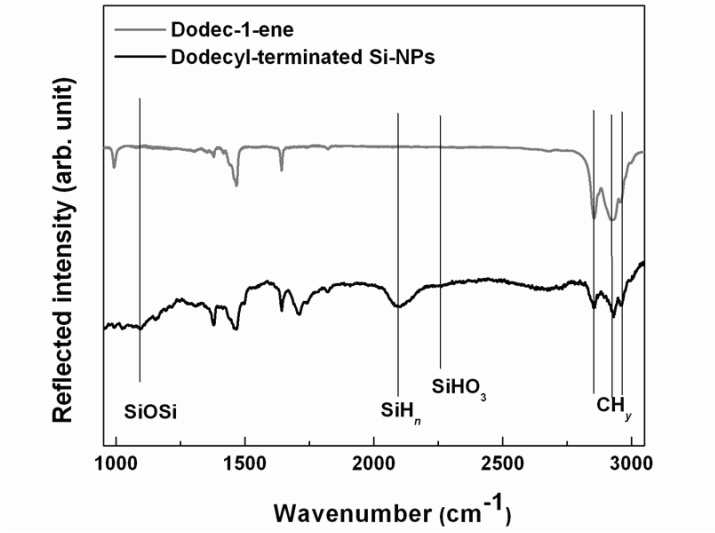

Fig. 4.9. FTIR spectra of pure dodec-1-ene and dodecyl-terminated Si-NPs.

The TEM investigations on Si-NPs (d_p ~ 52 nm, Fig. 4.2) were performed after HF etching and subsequent surface functionalization. Figure 4.10 shows the TEM pictures of functionalized Si-NPs. As can be seen clearly, the functionalized particles are non-agglomerated and highly crystalline. This indicates that the etching and functionalization process resolves the agglomeration of Si-NPs and do not affect their crystallinity. The particles are non-agglomerated because the organic molecules on silicon surface provide passivation against oxidation and steric hindrance against further agglomeration. The TEM picture in Fig. 4.10c clearly shows that all functionalized particles are not spherical in shape and have facetted/curved surface. The facetted surface in functionalized particles is seen due to presence of facetted particles in as-synthesized Si-NPs (see Fig. 4.2). It is also possible that HF etches the grain boundary of agglomerated Si-NPs that are formed due to agglomeration of particles inside the reaction chamber (see Fig. 4.2b), therefore, the resulting particles have the facetted/curved surface. Figure 4.10d shows the XRD pattern of functionalized Si-NPs. The data reveals that functionalized Si-NPs are crystalline in nature and have a diamond cubic structure. The calculated crystalline diameter of functionalized Si-NPs is 74.6±0.3 nm, which is almost similar to as-synthesized Si-NPs (d = 75.2±0.2 nm, Fig. 4.3). These results indicate that crystalline size and crystal structure of Si-NPs do not change after the surface functionalization in our experiments, further supporting that the crystalline core is not affected by etching and functionalization process.

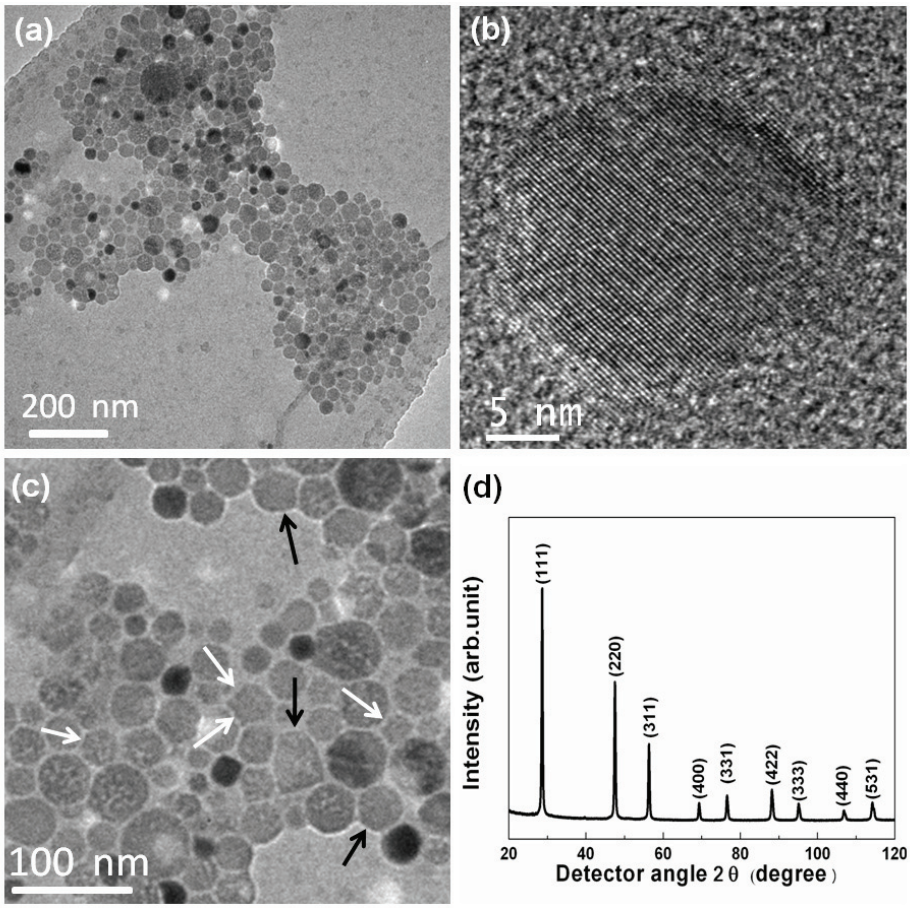

Fig. 4.10. (a) TEM image of dodec-1-ene functionalized Si-NPs. (b) The HR-TEM image shows the lattice fringes of functionalized Si-NPs. (c) The black and white arrows indicating the facetted and curved surface of functionalized Si-NPs, respectively. (d) XRD pattern of dodec-1-ene functionalized Si-NPs together with Miller indices of their Bragg peaks.

In another experiment, the as-synthesized Si-NPs (d_p ~ 13.2 nm, Fig. 4.4) were investigated after etching with HF and HNO_3 mixture and subsequent surface functionalization. Figure 4.11 shows the TEM images and size distribution of functionalized Si-NPs. It is clear that functionalized particles are non-agglomerated and process reduces the size of Si-NPs. Particles with diameter below 5 nm were also seen in the TEM image, which were not present in as-synthesized sample (inset Fig. 4.11a). The particle size distribution of treated Si-NPs is found to be very broad. The fitting of size distribution of functionalized Si-NPs with a lognormal function gives d_p of about 13 nm and σ_g of 1.53 (Fig. 4.11b). The wide size distribution may come from two reasons; (i) broad size distribution of as-synthesized sample, and (ii) inhomogeneous etching of Si-NPs. The probability of smaller particles to get etched faster is higher than bigger one because of their high surface to volume ratio. Together with some spherical particles, particles with

facetted and irregular surfaces are also observed (Fig. 4.11c-e). It is already shown above that etching of Si-NPs with HF results in non-agglomerated particles with facetted and curved surface. It is known from the literature that some crystallographic planes of silicon are etched faster compared to others due to difference in etching rate at different crystallographic directions [134]. Therefore, facetted/irregular surfaces are expected to form if particles are etched continuously using HF and HNO_3 mixture. The FFT of one HR-TEM image is shown in Fig. 4.11f with all Miller indices, representing the diamond structure of silicon. Analysis of the FFT image gives the lattice parameter of 0.557±0.003 nm, which is similar to the lattice parameter of the as-synthesized particles (see Fig. 4.4c). These results demonstrate that Si-NPs sustain their crystallinity and crystal structure during the size reduction.

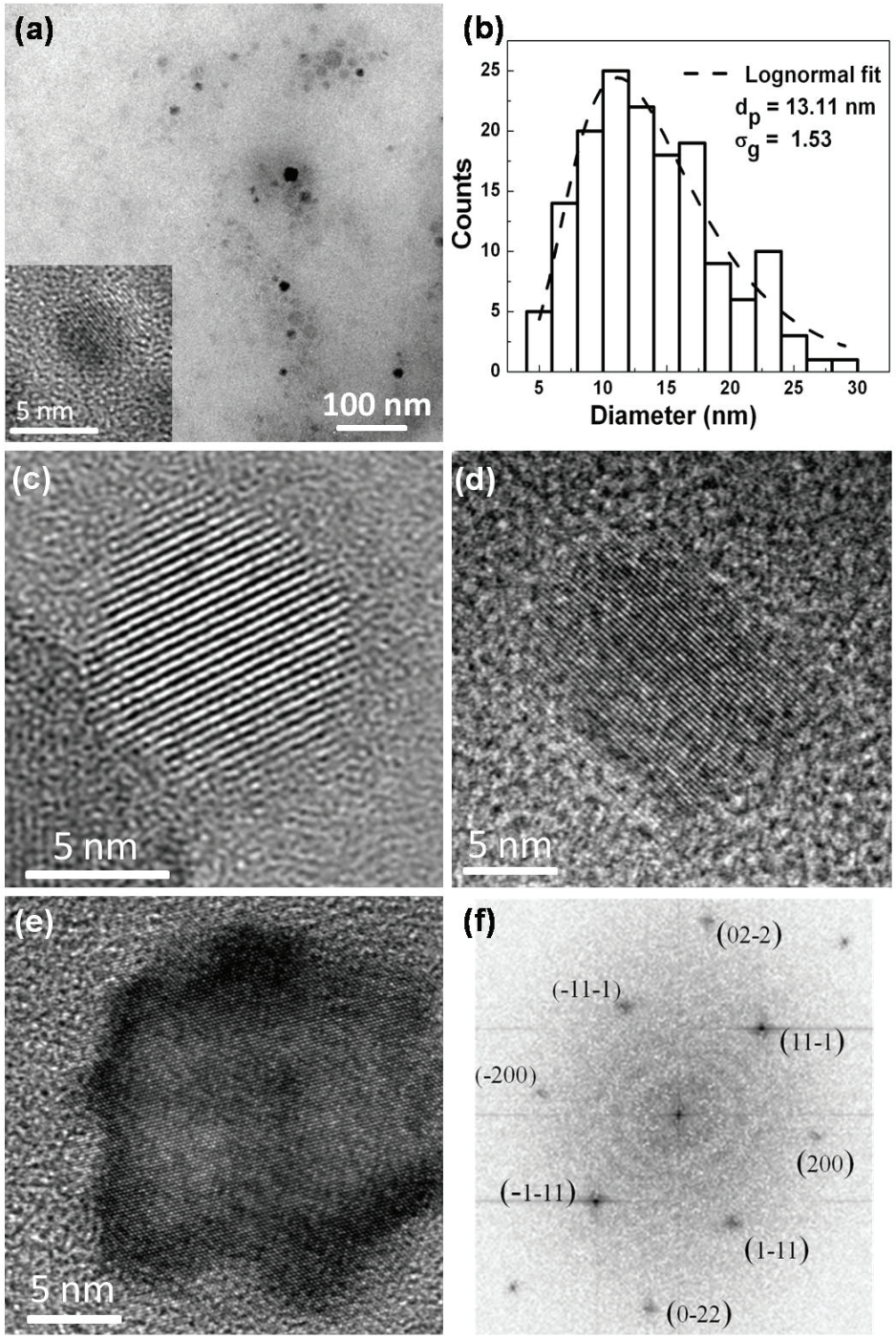

Fig. 4.11. (a) Bright field TEM image of dodec-1-ene functionalized Si-NPs, inset is the HR-TEM image showing particles with diameter less than 5 nm. (b) Histogram of particle size distribution of functionalized Si-NPs. (c) The HR-TEM images of functionalized particles showing the spherical particles. (d-e) Another HR-TEM images of functionalized Si-NPs showing irregular shapes of the particles. (f) FFT analysis of HR-TEM image of functionalized Si-NPs shown in (e).

4.2 Optical properties of Si-NPs

In this section, the influence of etching, surface re-oxidation and surface functionalization on the PL behavior of Si-NPs is examined.

4.2.1 Optical properties of etched Si-NPs

4.2.1.1 Influence of etching with HF

Because Si-NPs with diameter around 5 nm and less show PL emission in the visible range due to quantum confinement effect [114, 120], the particles with a mean diameter about 4.3 nm were examined in this study (see Fig. 4.5). The as-synthesized Si-NPs were etched with HF to remove oxides present on their surface. In order to address the changes in the PL properties of Si-NPs that are coming along with surface etching, the freshly etched sample was transported from the glove box to the spectrometer within an airtight glass bottle to avoid oxidation of particles. The FTIR spectra of as-synthesized and freshly etched Si-NPs are shown in Fig. 4.12. The complete disappearance of oxide related vibration modes of as-synthesized Si-NPs after etching confirms the oxide free surface of freshly etched sample.

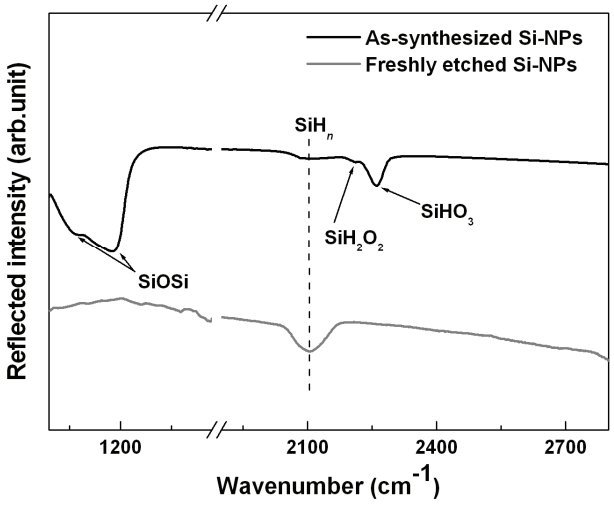

Fig. 4.12. FTIR spectra of as-synthesized and freshly etched Si-NPs.

Figure 4.13 illustrates the change in the PL emission spectrum of as-synthesized Si-NPs after etching with HF. For the sake of clarity, the PL of as-synthesized Si-NPs was increased by a factor of 4. It is observed that the emission spectrum of etched Si-NPs is slightly blue shifted compared to as-synthesized sample. The diameter of Si-NPs was calculated by using the modified equation for the relation between PL energy and Si-NPs size (equation 3.27). The calculated average diameter of as-synthesized Si-NPs is equal to 4.41 nm, which is in good agreement with that obtained from TEM (see Fig. 4.5d).

The PL spectrum of etched Si-NPs shows its maximum intensity around 740 nm, which suggests that the diameter of as-synthesized Si-NPs core is decreased to 4.05 nm after HF etching. The decrease in core diameter of Si-NPs can occur either by the re-oxidation of freshly etched Si-NPs or due to the dissolution of some silicon atoms along with the silicon oxide layer during the etching process. As no sign of surface oxides is observed in the FTIR spectrum of freshly etched sample (see Fig. 4.12), the re-oxidation of freshly etched Si-NPs can not be responsible for this shift. Additionally, the crystalline size of Si-NPs is not observed to change after etching with HF in our experiments as discussed above in Sect. 4.1.3. Therefore, it can be assumed that silicon atoms from the crystalline core are not dissolved during the etching process. Godefroo et al. [135] recently reported that the quantum confined wavefunction of Si-NPs is larger than their crystalline core diameter due to a leakage of the quantum confined wavefunction to their surrounding oxide shell. Therefore, the blue shift in the emission spectrum might originate from a confinement of the wavefunction to the silicon core after removal of the oxide shell.

The as-synthesized Si-NPs show a drastic increase in their PL intensity after HF etching (Fig. 4.13). The luminescence from as-synthesized Si-NPs can be hardly seen under the UV illumination, while after etching they start luminescing bright red (inset, Fig. 4.13). It is reported that PL intensity of Si-NPs is mainly limited by defect-mediated non-radiative excitons recombination. The non-radiative defect centers (such as vacancies and dangling bonds) are found to reside at Si/SiO_x interface [27, 136, 137]. When the concentration of non-radiative defects is large, there is high probability that the excitons are trapped there. Therefore, one of the main reasons for the increase in the PL intensity of etched sample could be due to the drastic decrease in defect concentrations because of the removal of the oxide layer and the saturation of dangling bonds with hydrogen.

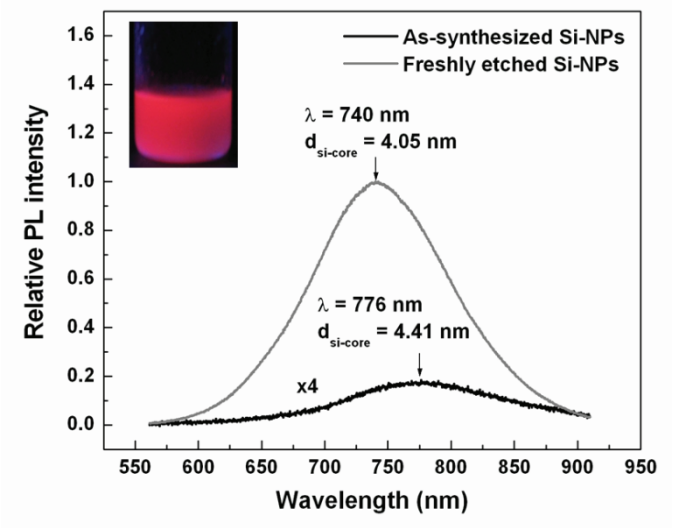

Fig. 4.13. PL spectra of as-synthesized and freshly etched Si-NPs. The PL intensity of as-synthesized sample is increased by a factor of 4. The wavelengths at which the maximum of PL spectra appear and calculated average particle diameters of Si-NPs from equation (3.27) are also shown. The inset shows a photograph of freshly etched Si-NPs in methanol dispersion under UV illumination.

In order to support this assertion, the EPR measurements on as-synthesized and etched Si-NPs were performed. The results of these measurements are shown in Fig. 4.14. For the as-synthesized sample, a broad resonance at $g \approx 2.006$ is observed, which originates from spectral contributions from different configurations of silicon dangling bonds [77]. The trivalent silicon atoms that are located at the Si/SiO_x interface (called P_b-centers) give a non-symmetrical signal in EPR [138, 139]. Also, the dangling bonds in a disordered environment (called *D*-centers) give rise to a symmetrical peak in EPR [140, 141]. The Si-NPs with diameter greater than 10 nm show non-symmetrical defect signal in EPR measurement, from which the contribution of P_b- and *D*-centers can be decomposed [77]. It is obvious that the shape the EPR spectrum of small as-synthesized Si-NPs is also not symmetrical, however, the defect line is less structured and a clear decomposition into contributions from P_b- and *D*-centers based on a line shape analysis is no longer possible. This can be attributed to a presumably strain-induced change of the interface between the Si-NP core and its oxide shell due to their small size [77]. The EPR spectrum of etched Si-NPs shows a strong decrease in defect signal intensity with respect to as-synthesized sample. In addition, the residual line is less structured and has a narrower linewidth, which corresponds to the linewidth that is typically observe for the *D*-center contribution of EPR spectra measured on larger Si-NPs. The drastic decrease in P_b-like silicon dangling bond states are ob-

served due to the removal of the oxide layer and the saturation of dangling bonds with hydrogen. The residual defect signal measured after HF etching is attributed to *D*-centers present in a sub-ensemble of Si-NPs with amorphous contributions. Thus, the drastic decrease in PL intensity of Si-NPs after HF etching can be significantly related to the decrease in of overall defects concentration.

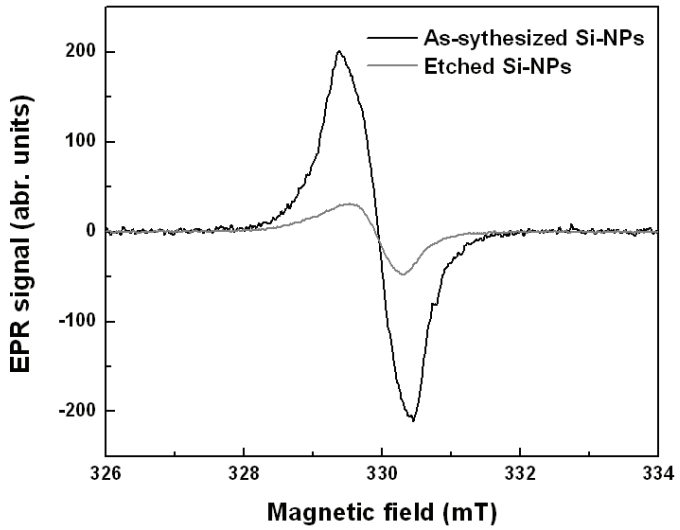

Fig. 4.14. EPR spectra of as-synthesized and etched Si-NPs.

4.2.1.2 Influence of etching with HF and HNO_3

In order to see the size dependent PL, the size of Si-NPs (d_p ~ 4.3 nm, Fig. 4.5) is reduced by etching them in a mixture containing HF and HNO_3. Different samples were prepared at various etching time. After the etching, the samples were washed with HF in order to make sure that no surface oxides remains on the surface. Figure 4.15a depicts the PL spectra recorded from different etched samples. It is clear that Si-NPs show a continuous blue shift in their emission spectra with increasing etching time. According to the quantum confinement model, the PL from Si-NPs blue shifts when the size of Si-NPs decreases [32, 114, 142-144]. Therefore, the blue shift in the emission spectra can be reliably correlated to the size reduction of Si-NPs during etching. It is observed that the color of emitted light evolves from red (731 nm) to green (556 nm) during the etching process (Fig. 4.15a,b), thereby endorsing the origin of red to green PL from the quantum confinement effects.

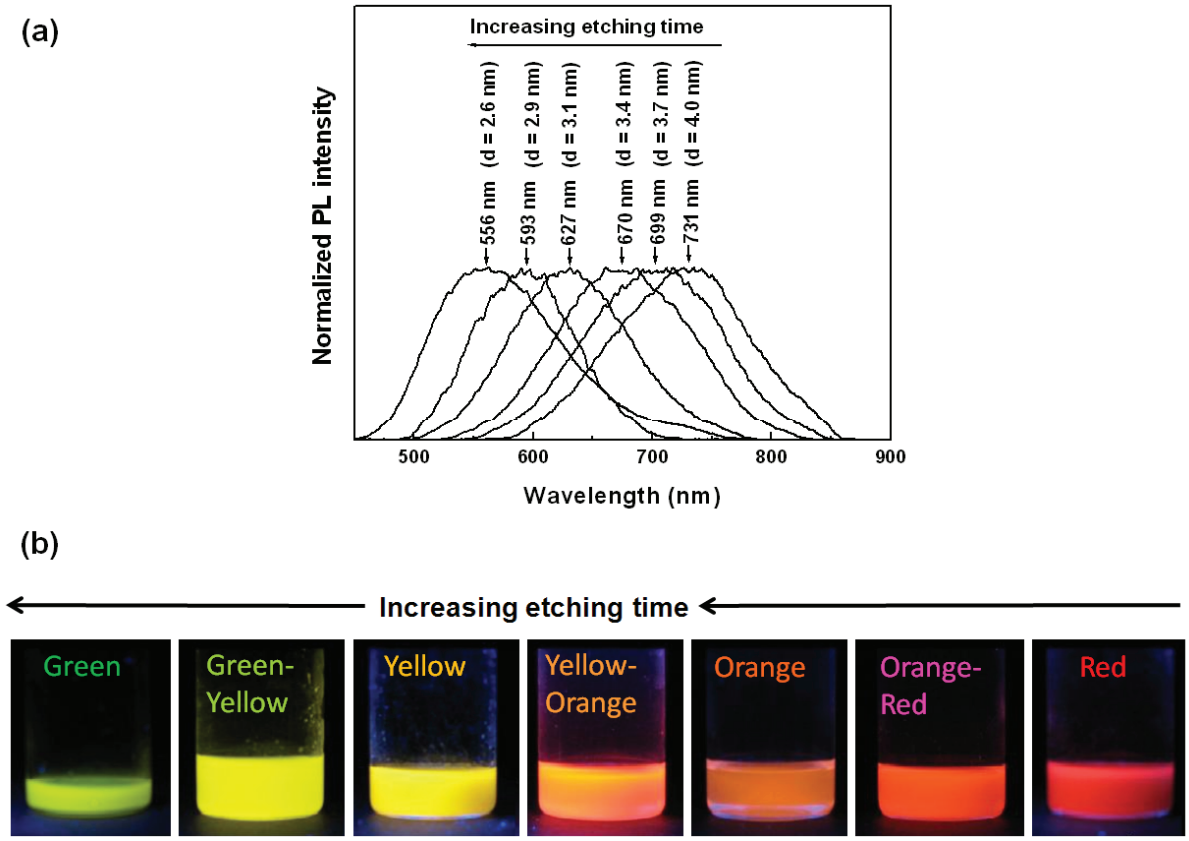

Fig. 4.15. (a) Normalized PL emission spectra of Si-NPs evolved during etching them with a mixture containing HF and HNO_3. The wavelength at which the peaks of PL spectra appear and the Si-NPs sizes they indicate according to equation (3.27) are also shown. (b) Sample photographs of freshly etched Si-NPs with increasing etching time. Samples are dispersed in methanol and illuminated with UV light.

As the production of large quantity of very small nanoparticle is very time consuming, the particles with diameter much larger than 5 nm are also used to synthesize luminescing Si-NPs. The particles with mean diameter about 13.2 nm were used in this study (see Fig. 4.4). The as-synthesized particles do not show any PL in the visible range owing to their large size. However, they start to luminesce very bright in the visible regime after few minutes of etching. Figure 4.16 depicts the emission spectra of Si-NPs produced at different etching time, and the pictures of chloroform dispersions of these particles in normal daylight and under UV illumination. It is observed that with increasing etching time, Si-NPs show a blue shift in their emission spectrum from red (spectrum A) to green (spectrum D). Surprisingly, upon further increasing the etching time, the green emitting Si-NPs show a red shift in their spectrum and emit in yellow-orange regime (spectrum E). The mechanism underlying in the change of the emission wavelength from

red to green with increasing etching time can be attributed to the size dependent band gap of silicon due to the quantum confinement effect. However, the red shift after green emission can not be explained by this effect. Since the particle size distribution of treated Si-NPs is very broad, as shown in Fig. 4.11b, it is likely that the emission from silicon comes from very small fraction of particles that contributes to quantum confinement effect. Therefore, the red shift in the spectrum can be speculated in terms of the formation of new size distribution of Si-NPs on increasing the etching time owing to complete disappearance of very small sized green luminescing nanoparticles and introduction of new particles in the quantum confinement regime.

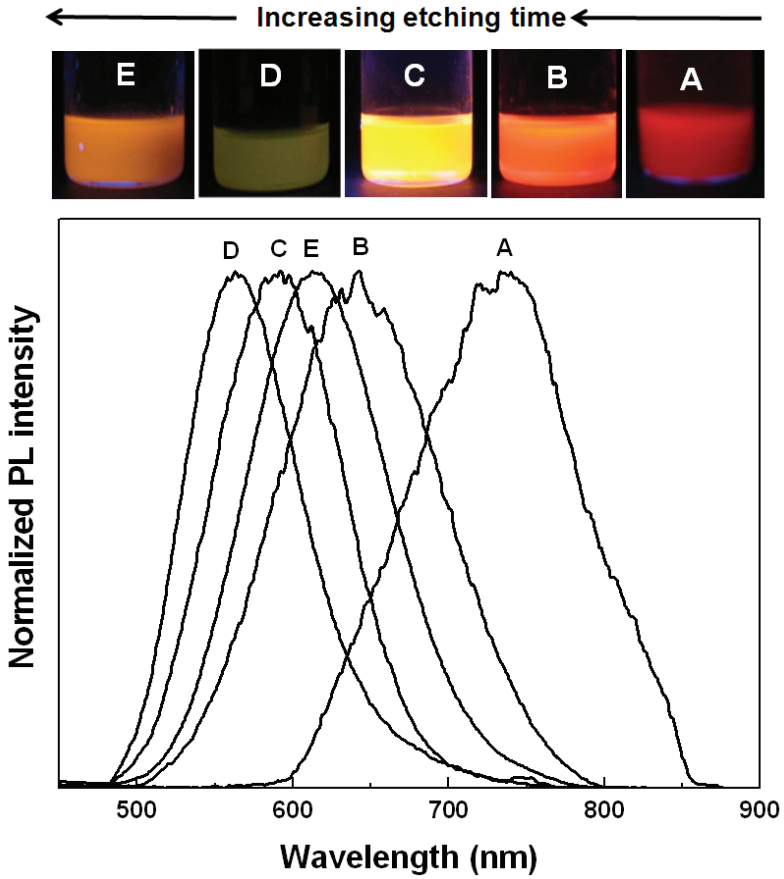

Fig. 4.16. (a) Normalized PL emission spectra, and (b) corresponding red (λ = 735 nm, etching time (t_{et}) = 2 min), orange (λ = 641 nm, t_{et} = 9 min), yellow (λ = 592 nm, t_{et} = 11 min), green (λ = 563 nm, t_{et} = 13 min) and yellow-orange (λ = 614 nm, t_{et} = 16 min) color from etched Si-NPs produced by etching them with a mixture containing HF and HNO_3.

4.2.1.3 Air stability of etched Si-NPs

Figure 4.17 demonstrates the evolution of the FTIR spectra of etched Si-NPs with air exposure time. The FTIR spectrum of freshly etched Si-NPs shows the presence of SiH_n stretching vibration mode at 2097 cm^{-1} along with the SiH_2 scissor mode/SiH_3 degenerate deformation vibration modes at 902 cm^{-1} [124, 125], indicating the H-terminated surface of Si-NPs. It is observed that the signature of SiOSi peak at 1096 cm^{-1} gradually intensified and became broader with time, which is accompanied by the diminishing intensity of SiH_n and SiH_2/SiH_3 vibration. Additionally, $SiHO_3$ bending mode at 877 cm^{-1} starts to emerge after 23 h of air exposure. After 46 h, the SiH_2/SiH_3 vibration disappeared almost completely and very weak signature of SiH_n is observed with dominant oxide related modes.

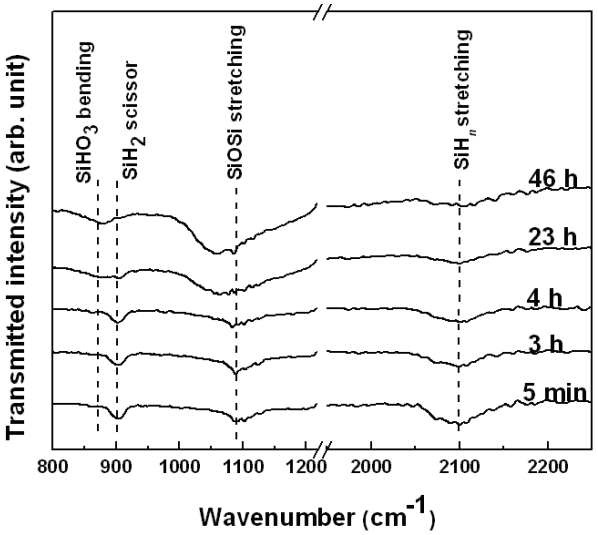

Fig. 4.17. Evolution of the FTIR spectra of etched Si-NPs as a function of air exposure time. The FTIR spectra are measured in the transmission mode.

In order to study the effect of surface oxidation on the PL property of etched Si-NPs, the freshly etched Si-NPs are stored in open air and the PL spectra are recorded at different air exposure times. It is observed that the PL of most of the etched Si-NPs is completely quenched after storage in air. As an example, the PL emission spectra of green emitting nanoparticles as a function of air exposure time are shown in Fig. 4.18. As the air exposure time increases, the PL peak of green emitting etched nanoparticles at 580 nm continuously shifts towards lower wavelength (blue shift) with decreasing PL intensity. As the oxidation proceeds, the oxides grow on the surface of Si-NPs (see Fig. 4.17). The growth of oxide shell on the surface of Si-NPs decreases the

size of the crystalline silicon core and therefore causes the blue shift according to quantum confinement effect. Pi et al. [28] and Prokes at al. [145] demonstrated that decrease in PL intensity of Si-NPs and porous silicon is associated with the increase in dangling bond concentration. Therefore, it is possible that the dangling bond concentrations are increasing during oxidation of etched Si-NPs and as a result the PL intensity decreases.

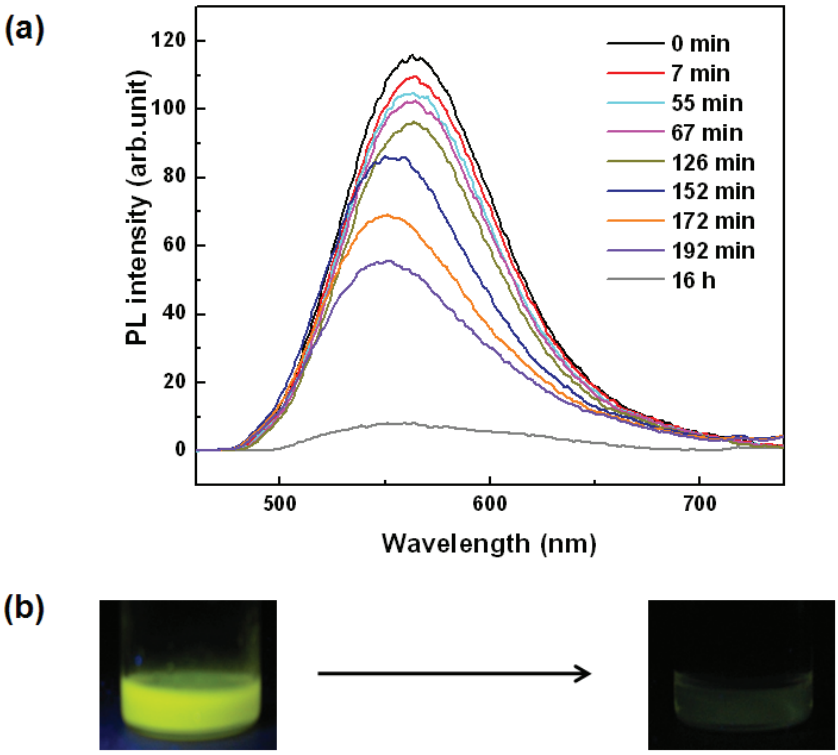

Fig. 4.18. (a) PL spectra of green emitting etched Si-NPs as a function of air exposure time. (b) Photographs of Si-NPs dispersion in methanol under UV illumination: Freshly etched (left) and after 1 day of air exposure (right).

Blue emission from Si-NPs was obtained after the oxidation of orange emitting etched Si-NPs with 620 nm emission (Fig. 4.19). Figure 4.19a shows the time dependent air oxidation behavior of orange emitting etched Si-NPs. The first spectrum was recorded after 5 minutes of air exposure. This spectrum shows a broad emission with its maximum at 620 nm and a shoulder at 450 nm (blue emission). Theoretical calculation suggests that it is possible to get blue emission from Si-NPs with diameter less than 2 nm [119]. Therefore, the peak at 450 nm can be originated from the crystalline silicon due to the presence of blue emitting Si-NPs together with Si-NPs with 620 nm emission. On the other hand, it is also reported that defects in the silica matrix (oxygen-deficient centers) are responsible for blue emission [136, 146-148]. As some oxy-

gen vacancies are present the silicon oxide layer shell around Si-NPs [28], therefore, the peak at 450 nm may also originates from these defects centers in the oxide shell after the oxidation of freshly etched Si-NPs. As the oxidation proceeds, the peak at 620 nm shows decrease in PL intensity with continuous blue shift, while the peak position at 450 nm was not influenced by the oxidation and shows an increase in PL intensity with time. The blue shift in the emission peak at 620 nm is consistent with a reduction of the silicon core size due to oxidation and therefore the emission mechanism is based on quantum size effect. Furthermore, the decrease in PL intensity could be well understood by the increase in non-radiative defect centers upon oxidation of Si-NPs [28, 145]. In contrast to the emission peak at 620 nm, the wavelength of the blue emission peak position is not affected by the oxidation. Therefore, the possibility of blue emission from the crystalline core due to quantum size effect can be ruled out. Thus, the blue PL in our sample must originate from the oxide-induced defects at the surface of Si-NPs. The increase in PL intensity was also observed for blue emission with increased oxidation time. We conclude that the blue luminescing defect centers accompany with increasing oxidation and thereof PL intensity also increases.

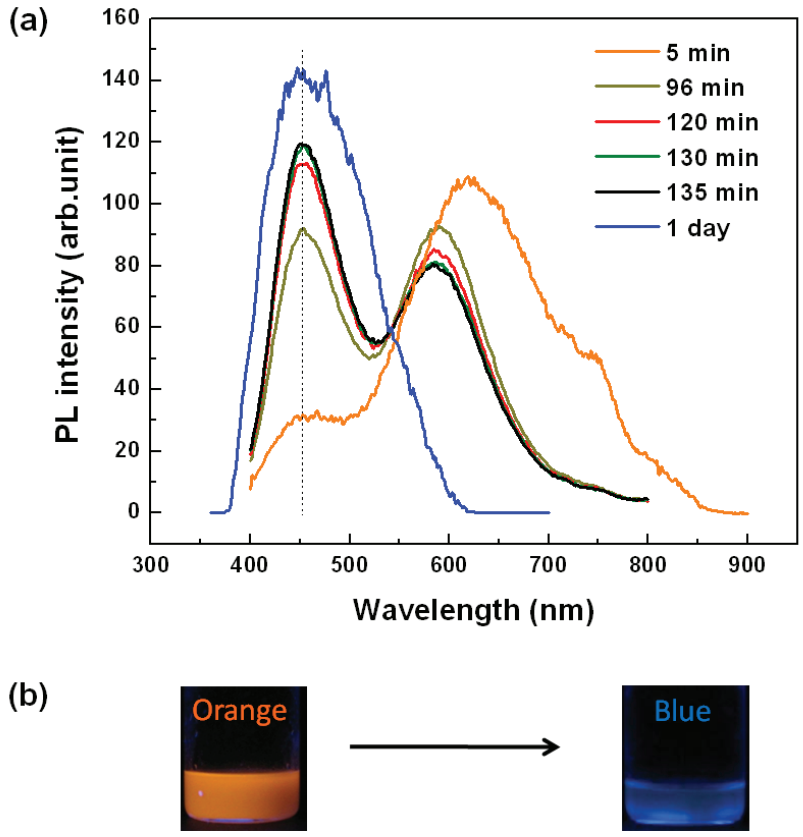

Fig. 4.19. (a) Evolution of the PL spectra of freshly etched Si-NPs as a function of air exposure time. (b) Picture of Si-NPs dispersion under UV illumination: Freshly etched (left) and after 1 day of air exposure (right). Note that the picture of freshly etched sample was taken at $t = 0$, whereas the first PL spectrum was recorded after 5 min of air exposure.

4.2.2 Optical properties of functionalized Si-NPs

4.2.2.1 Influence of surface functionalization

It is already shown in Sect. 4.1.3 that the functionalization of Si-NPs alters the surface properties of Si-NPs, while maintaining their size. Despite having similar size, a shift in the emission of functionalized Si-NPs with respect to freshly etched particles is observed. As an example, the PL spectra of green and red emitting freshly etched Si-NPs after their surface functionalization with dodec-1-ene are shown in Fig. 4.20. It can be clearly seen that green and red emitting freshly etched Si-NPs show red and blue shift after their surface functionalization, respectively. Based on these observations, various freshly etched Si-NPs with different emission wavelengths were prepared and shift in the PL emission is measured after their surface functionalization. In Fig.

4.21a, the measured shift is plotted as a function of the emission wavelength of etched Si-NPs. The pictures of the samples marked as A, B, C and D in Fig. 4.21a are also shown in Fig. 4.21b. It is observed that the nature of the shift is dependent on the emission wavelength of the freshly etched Si-NPs. Red to orange luminescent etched Si-NPs show blue shift in the spectrum after surface functionalization in contrast to green to yellow luminescent nanoparticles. According to Reboredo and Galli [53], the replacement of hydrogen with alkyl group on the Si-NP surface causes a change in HOMO and LUMO energy positions. Their calculation on small silicon clusters (Si_{20}, Si_{29}, Si_{66}, Si_{142}) suggests that the HOMO-LUMO band gap of alkyl terminated Si-NPs decreases with respect to H-terminated nanoparticles. Godefroo et al. [135] reported a leakage of quantum confined wavefunction of 3 nm diameter Si-NPs at the transition from silicon to silicon oxide, which causes an increase in its quantum confined wavefunction approximately by 1.9 nm. Therefore, the observation of red shift from green to yellow luminescent Si-NPs can be reliably explained by a decrease in the HOMO-LUMO band gap energy because of the replacement of hydrogen by the alkyl group on the silicon surface, and leakage of the wavefunction at the boundary of quantum confined silicon and organic layer. However, the origin of the blue shift from larger clusters (emitting from orange to red regime) is still unclear.

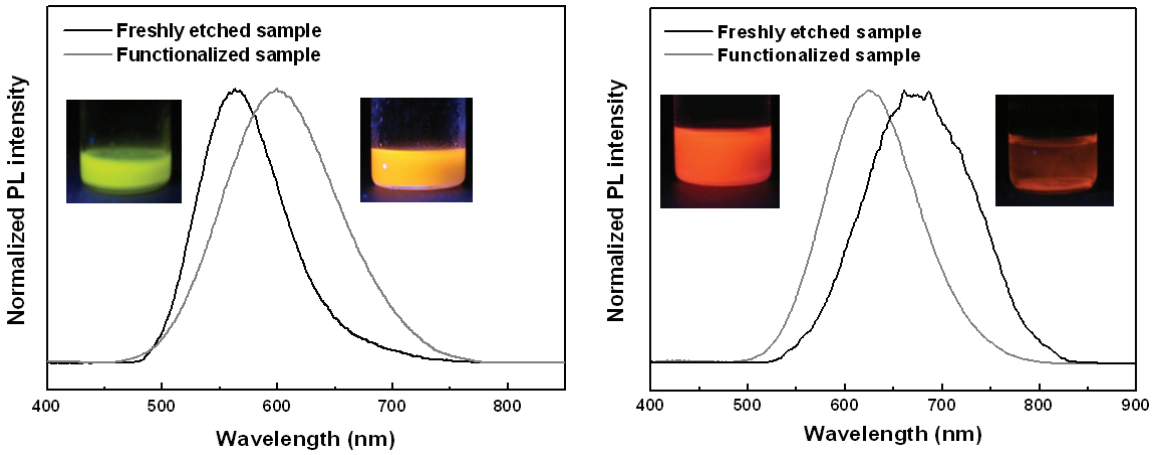

Fig. 4.20. Normalized PL spectra of freshly etched and dodec-1-ene functionalized sample: (a) Functionalization of green luminescing, and (b) red luminescing etched Si-NPs. The photographs of freshly etched and functionalized sample under UV illumination are also shown.

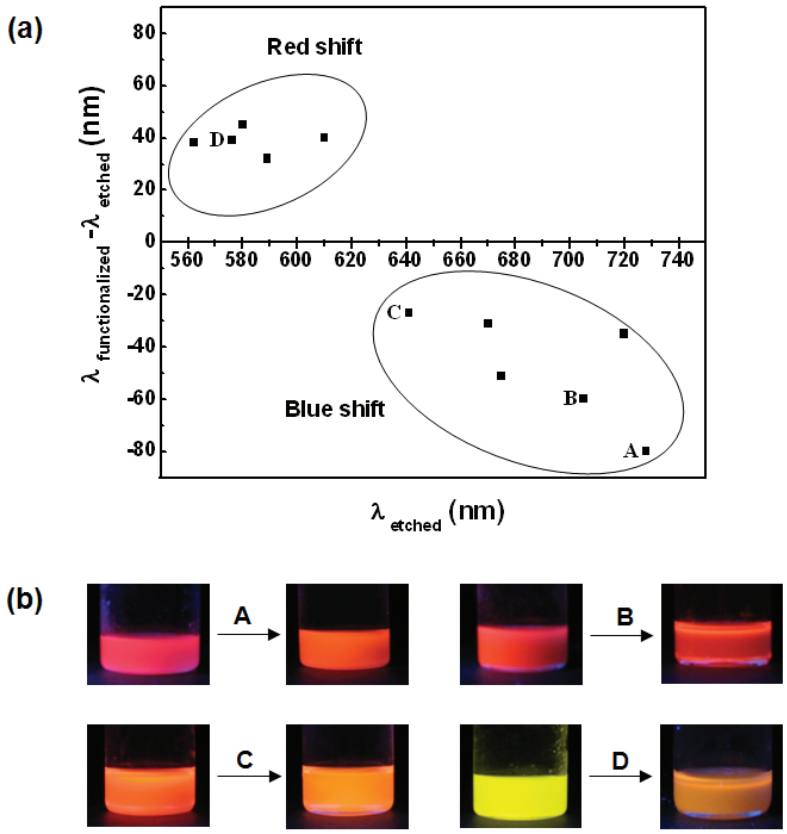

Fig. 4.21. (a) Shift in the emission wavelength of freshly etched Si-NPs after surface functionalization. (b) Sample photographs of freshly etched (at the tail of arrow) and functionalized (at the head of arrow) Si-NPs under UV illumination, corresponding to A, B, C and D data points of (a), showing change in their emission color.

4.2.2.2 Factors influencing the PL properties of functionalized Si-NPs

It is observed that the magnitude of shift in the emission wavelength of functionalized Si-NPs with respect to freshly etched sample can be altered. In order to study the factors influencing the shift, the PL emission of functionalized Si-NPs is measured by varying different reaction parameters during the surface functionalization. Note that all the results shown below are obtained after the surface functionalization of green-yellow emitting etched Si-NPs and in all the cases a red shift in their PL emission is observed. The PL results shown in one figure can not be compared with the others as the emission wavelength of green-yellow emitting freshly etched sample is not the same. All the PL measurements were performed using a diode laser with an excitation wavelength of 405 nm. Therefore, the second harmonic of the excitation wavelength is present as a sharp signal in the spectra shown below.

Figure 4.22a demonstrates the influence of functionalization temperature on the PL property of functionalized Si-NPs. The Si-NPs were functionalized at two different temperatures; 120°C and 160°C. The particles that undergo functionalization at 160°C emit at longer wavelength compared to that functionalized at 120°C. The particles functionalized at high temperature show relatively low intensity of remaining SiH_n vibrations in the FTIR spectrum compared to that treated at low temperature (Fig. 4.22b). Additionally, a high intensity of $SiHO_3$ stretching mode is observed for particles functionalized at 160°C. The intense $SiHO_3$ peak may originate from increased oxidation of Si-NPs surface with dissolved oxygen and moisture at elevated temperature during the surface functionalization. This result compares well with the findings of Nelles and co-workers [52]. They modified the surface of Si-NPs with oct-1-ene using thermally induced hydrosilylation process at 80°C and 140°C. They observed that Si-NPs functionalized at 140°C show higher surface coverage together with increased occurrence of oxides compared to the particles that were functionalized at 80°C.

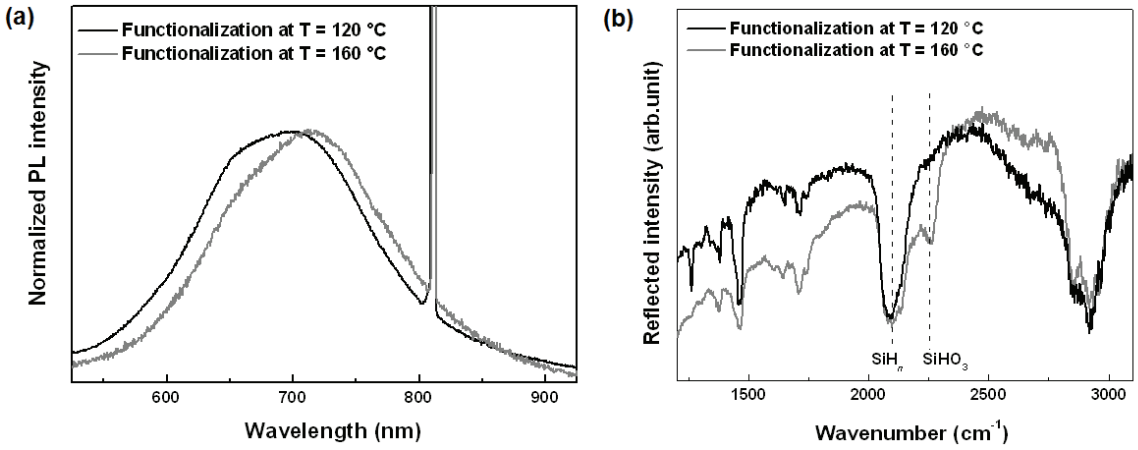

Fig. 4.22. (a) Normalized PL spectra and (b) FTIR spectra of Si-NPs functionalized with dodece-1-ene for 6 h at 120°C and 160°C.

In photoinitiated hydrosilylation, the effect of UV energy on the PL property of Si-NPs was examined by using two different UV wavelengths (366 nm and 254 nm) (Fig. 4.23a). The particles functionalized with high energy UV radiation (λ = 254 nm) show larger red shift in their emission spectrum compared to Si-NPs that were exposed at low energy (λ = 366 nm). The FTIR spectra of functionalized Si-NPs are presented in Fig. 4.23b. The particles functionalized at higher UV energy radiation show slightly lower intensity of unreacted SiH_n vibration and higher in-

tensity of $SiHO_3$ stretching mode compared to that exposed to low energy radiation, however, the difference is not big.

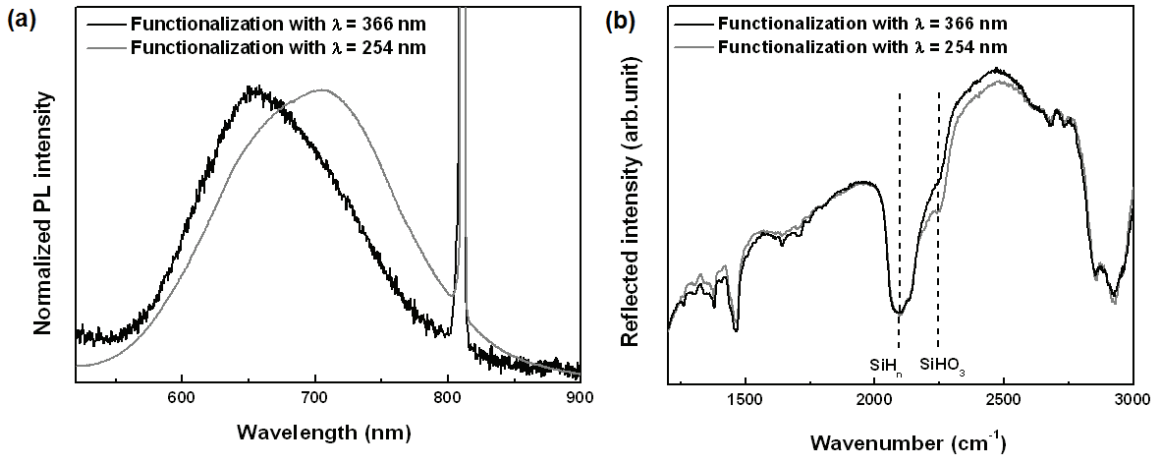

Fig. 4.23. (a) Normalized PL spectra, and (b) FTIR spectra of Si-NPs functionalized with dodece-1-ene for 6 h using 366 nm and 254 nm UV radiation.

Figure 4.24a shows the PL spectra of Si-NPs recorded after their surface functionalization using photoinitiated (λ = 254 nm) and thermally induced (T = 120°C) hydrosilylation. A significant difference in the emission spectra of both samples is observed. In case of thermally induced hydrosilylation, the red shift was about 83 nm higher than photoinitiated hydrosilylated sample. In the FTIR spectra (Fig. 4.24b), the particles that are functionalized using thermally induced hydrosilylation show relatively low intensity of remaining SiH_n vibration and high intensity of $SiHO_3$ stretching mode compared to photoinitiated hydrosilylated sample. The results agree with the work of Nelles et al. [52], who studied thermally and UV light mediated hydrosilylation of Si-NPs and obtained the lower functionalization efficiency for UV light mediated hydrosilylation.

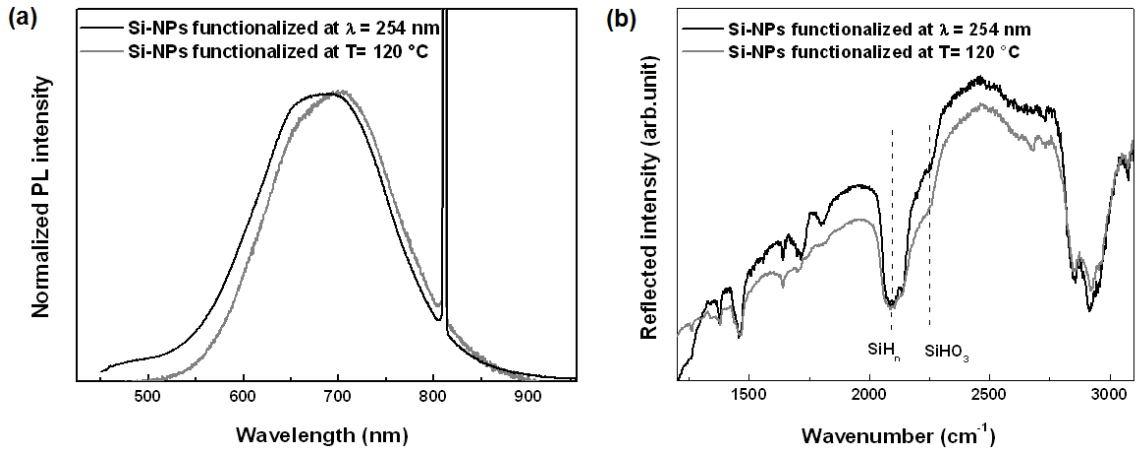

Fig. 4.24. (a) Normalized PL spectra, and (b) FTIR spectra of Si-NPs functionalized with dodece-1-ene for 6 h using photoinitiated (λ = 254 nm) and thermally induced (T = 120°C) hydrosilylation.

In another experiment, the functionalization of freshly etched Si-NPs was carried out using octadec-1-ene, dodec-1-ene, and a mixture of dodec-1-ene and octadec-1-ene (1/1 v/v). Figure 4.25a shows the PL spectra of functionalized Si-NPs. The functionalization was carried out using thermally induced hydrosilylation at a temperature of 120°C for 6 h. It is observed that the emission wavelength of particles with mixed surface functionalization lies between dodec-1-ene and octadec-1-ene functionalized Si-NPs. The FTIR spectra of the corresponding Si-NPs are shown in Fig. 4.25b. The peak from SiH_n stretching mode around 2090 cm^{-1} is present in all the spectra of functionalized Si-NPs due to the incomplete surface coverage of organic molecules on their surface. The relative intensity of SiH_n stretching vibration in case of octadec-1-ene functionalized Si-NPs is higher compared to dodec-1-ene, which is due to the large steric hindrance of the octadecyl molecule. The functionalized Si-NPs also show $SiHO_3$ stretching mode at 2245 cm^{-1}, which might stem due to little oxidation of Si-NPs during surface functionalization. The particles that undergo mixed surface functionalization show an intermediate behavior in the FTIR spectrum.

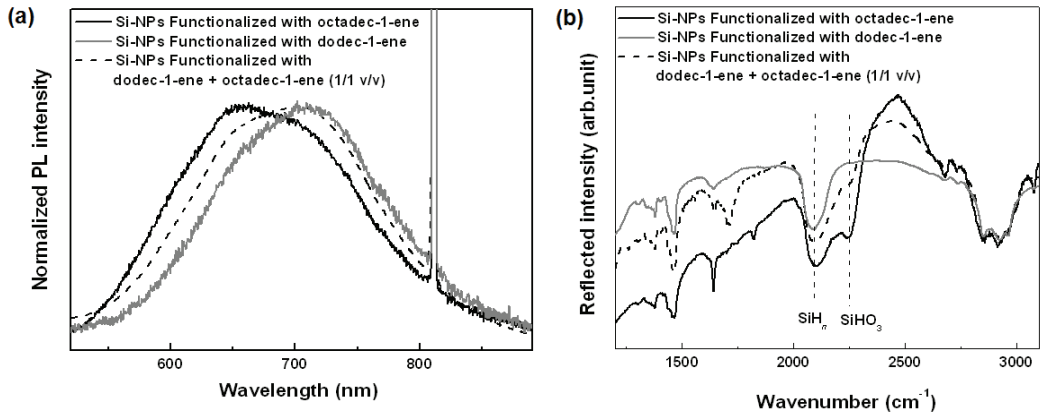

Fig. 4.25. (a) Normalized PL spectra, and (b) FTIR spectra of Si-NPs after their surface functionalization with octadec-1-ene, dodec-1-ene, and a mixture of octadec-1-ene and dodec-1-ene (1/1 v/v). Functionalization was done at 120°C for 6 h.

The effect of functionalization time on the PL spectra of functionalized Si-NPs is presented in Fig. 4.26. The functionalization was carried out at 120°C with dodec-1-ene for 6 h and 10 h. The Si-NPs functionalized for longer time show an increased shift in their emission spectrum compared to particles that were functionalized for shorter time (Fig. 4.26a). FTIR spectra of Si-NPs functionalized at different times (Fig. 4.26b) shows that the intensity of SiH_n vibration decreases with increasing functionalization time, which implies that more ligands on the silicon surface are grafted by reacting residual hydrogen present onto the surface. When the functionalization time was increased from 10 h to 14 h, no reasonable difference has been observed in their PL and FTIR spectra. This might be due to the saturation of Si-NPs surface for the further attachment of organic molecules.

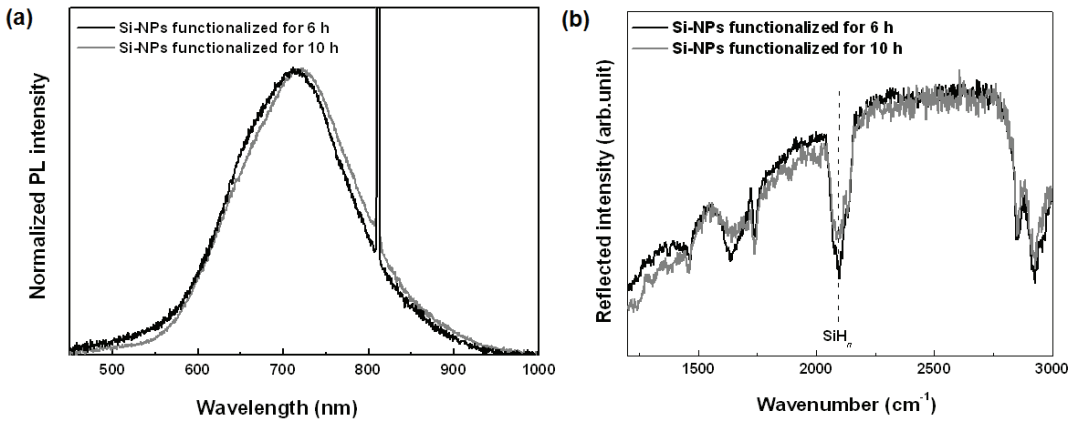

Fig. 4.26. (a) Normalized PL spectra, and (b) FTIR spectra of Si-NPs functionalized with dodece-1-ene using thermally induced (T = 120°C) hydrosilylation for 6 h and 10 h.

If we assume that Si-H bonds are only consumed in the formation of Si-C bonds during surface functionalization, we can compare the coverage of Si-NPs with organic ligands by comparing the amount (FTIR intensity) of unreacted SiH_n bonds with the initial amount (presuming that there is no significant oxidation that will consume SiH_n bonds). As the surface functionalization proceeds, the coverage of the Si-NPs surface with organic molecules increases (Fig. 4.26b). The organic molecules with longer carbon chain provide lower surface coverage compared to shorter alkenes because of high steric hindrance, and the particles that undergo mixed surface functionalization showed intermediate surface coverage (Fig. 4.25b). The Si-NPs show enhanced coverage of organic ligands on their surface at elevated temperature (Fig.4.22b) and high energy UV irradiation with 254 nm (Fig. 4.23b). Additionally, the thermally induced hydrosilylation process gives a higher surface coverage compared to the photoinitiated hydrosilylation (Fig. 4.24b). It is found that the functionalization of Si-NPs using thermally induced hydrosilylation gives the best surface coverage with dodec-1-ene at temperature 120°C and functionalization time of 10 h.

All the results shown above give us a hint that surface coverage plays a very prominent role in determining the PL property of functionalized Si-NPs. It is noteworthy that all the particles with higher surface coverage (reduced intensity of SiH_n vibration signal) showed an increased red shift in their emission spectrum compared to those having a lower coverage of ligands (higher intensity of SiH_n vibration signal). Despite this fact, no systematic correlation between the magnitude of the red shift and the surface coverage of Si-NPs is observed. As an educated guess, one can assume that there is a correlation between the increased size of the particle (core + shell) with higher surface coverage and the red shift. This assumption is supported by the fact that the wavefunction within the nanoparticles is not limited to the crystalline silicon core [135]. Additionally, it is observed that the shape of PL was also influenced by the reaction conditions. A further study is necessary to explore the anomalous PL behavior of functionalized Si-NPs.

4.2.2.3 Air stability of functionalized Si-NPs

In this study, the air stability of Si-NPs was examined after their surface functionalization with dodec-1-ene and different kind of esters (ethyl undecylenate (ETU), vinyl benzoate (VB) and

ethyl-2-methyl-4-pentenoate (EMP)) [149]. The chemical structures of these organic reagents are presented in Appendix A. To make a meaningful comparison, all the samples in this study were prepared under similar conditions. As the boiling point of the VB is very low (BP = 96°C), the functionalization of Si-NPs was performed at 80°C. The functionalization time was kept constant for 12 h. No extra effort was made to remove dissolved oxygen from the organic reagents. To investigate the stability of functionalized Si-NPs, the functionalized particles were exposed to air under ambient conditions after separating the particles from their respective alkenes by centrifugation and subsequent drying in vacuum.

The FTIR spectra of dodec-1-ene functionalized Si-NPs at different air exposure time are shown in Fig. 4.27a. In the spectrum of freshly functionalized Si-NPs, the peaks from SiH_n vibration mode at 2100 cm^{-1} and SiOSi vibration mode at 1060 cm^{-1} are present, suggesting incomplete surface coverage and oxidation of Si-NPs surface during functionalization process, respectively. Upon air exposure, the SiOSi vibration peaks at 1060 cm^{-1} and 1177 cm^{-1} show an increase in intensity with time. The lower energy peak (1060 cm^{-1}) can be attributed to bridge-bonded oxygen between the first and second layer of silicon atoms and the higher energy peak (1177 cm^{-1}) to bridge-bonded oxygen below the second layer of silicon atoms [150]. In addition to the broadening of SiOSi peak, the position of the Si-H stretching vibration peak shifts to higher energy due to backbonding of silicon with oxygen. As a result, two new features start to emerge at 2189 cm^{-1} and 2242 cm^{-1}, which can be assigned to Si-H stretching vibration in SiH_2O_2 and $SiHO_3$ configuration, respectively. Figure 4.27b shows the high resolution FTIR spectrum of Si-H vibration after 28 days of air exposure. It is clear that the Si-H vibration peak can be decomposed into four different Gaussian profile centered at 2096 cm^{-1}, 2161 cm^{-1}, 2189 cm^{-1}, and 2242 cm^{-1}, which correspond to SiH_2, SiH_3, SiH_2O_2, and $SiHO_3$, respectively [128, 130].

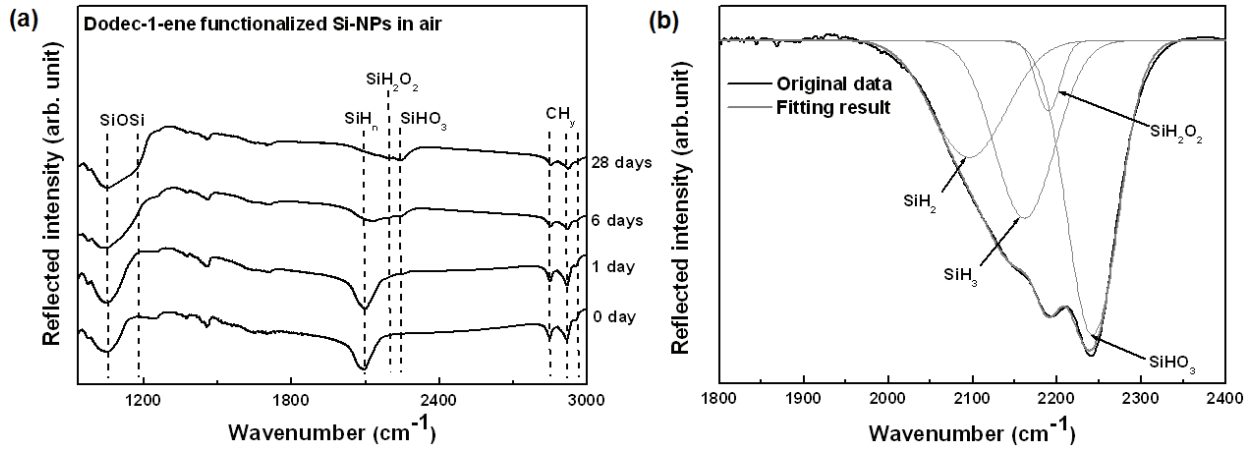

Fig. 4.27. (a) Evolution of the FTIR spectra of dodec-1-ene functionalized Si-NPs as a function of air exposure time. (b) Deconvolution of the SiH_n peak of dodec-1-ene functionalized Si-NPs after 28 days of air exposure.

Figure 4.28 shows the FTIR spectra of ETU, VB, and EMP functionalized Si-NPs together with the dodec-1-ene functionalized sample, recorded before and after 28 days of air exposure. The time dependent FTIR spectra of ETU, VB, and EMP functionalized Si-NPs in air are presented in Fig. 8.2–8.4 of Appendix A. Similar to dodec-1-ene functionalized Si-NPs, these particles also show a decrease in SiH_n vibrations and increase in SiOSi vibration upon oxidation. However, the relative increase in the broadening of the SiOSi vibration peak in ETU functionalized Si-NPs is small compared to dodec-1-ene functionalized Si-NPs. This shows that the formation of bridge-bonded oxygen below the second layer of silicon is mostly suppressed in ETU functionalized sample. In case of VB, relatively high concentrations of Si-H bonds that are not attacked by oxygen are observed after oxidation. In order to make a meaningful comparison between different samples with regard to their surface coverage and stability against oxidation, the efficiency of functionalization and their susceptibility towards oxidation is compared. The efficiency E_F of functionalized sample is calculated from the ratio of change in integrated intensity of SiH_n absorption (1950 cm^{-1} –2250 cm^{-1}) over the original intensity [52, 151],

$$E_F = \frac{A_0 - A_1}{A_0} \tag{4.1}$$

where A_0 and A_1 are the baseline to peak area of the reference sample and hydrosilylated sample, respectively. The efficiency E_F of ester functionalized Si-NPs is compared with respect to dodec-1-ene. The accuracy of this comparison relies on following assumptions as stated in Ref. [151];

(i) the unit intensities of SiH, SiH_2, SiH_3 bonds are similar, and (ii) the number of Si-H bonds that are consumed during the surface functionalization other than in the formation of Si-C bonds (e.g. in surface oxidation) are same in all the samples.

It is also necessary to define a measure for the relative susceptibility of different functionalized Si-NPs towards air oxidation. As discussed above, during the oxidation process the intensity of SiOSi vibration signal increases (due to formation of bridge-bonded oxygen) and the intensity of SiH_n vibration decreases (because increased backbonded oxygen shifts its vibration frequency to higher energies). Therefore, to make a qualitative comparison of the oxidation susceptibility of different functionalized samples, one can define the oxidation susceptibility index S_o as,

$$S_o = \frac{(A_{\mathrm{Si0Si}} / A_{\mathrm{SiH_n}})_{28\mathrm{days}}}{(A_{\mathrm{Si0Si}} / A_{\mathrm{SiH_n}})_{0\mathrm{days}}} \tag{4.2}$$

where A_{SiOSi} and A_{SiHn} are the baseline to peak area of SiOSi absorption (980 cm^{-1} –1200 cm^{-1}) and SiH_n absorption (1950 cm^{-1} –2250 cm^{-1}), respectively.

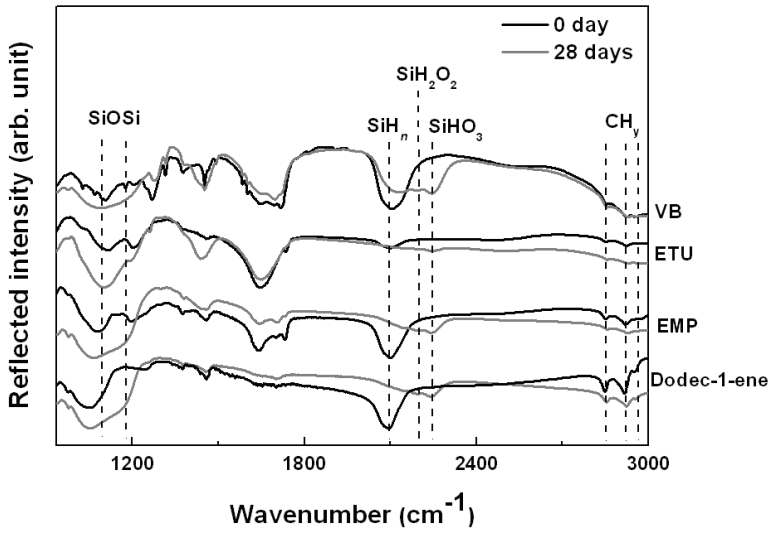

Fig. 4.28. FTIR spectra of dodec-1-ene, VB, EMP and ETU functionalized Si-NPs: Freshly functionalized sample (black curves) and after 28 days of surface oxidation in air (gray curves).

Table 4.1 summarizes the relative functionalization efficiency and oxidation susceptibility index of different functionalized samples. The relative functionalization efficiency of different organic reagent is compared with respect to dodec-1-ene. It is found that functionalization of Si-NPs with dodec-1-ene and ETU gives higher surface coverage compared to VB. Despite of

having the same functional groups, ETU, EMP and VB show very large differences in the surface coverage of Si-NPs. The methyl side group in EMP and the bulky benzyl group in VB are likely to hinder further reactions of remaining Si-H bonds on the Si-NPs surface and thus lead to a reduced functionalization efficiency. The functionalization efficiency of VB functionalized Si-NPs was found to be the lowest, which is expected due to large steric hindrance of the bulky benzyl group close to the silicon surface. Additionally, ester groups in attached VB molecules might further decreases the number of Si-H bonds available for functionalization by forming hydrogen bridge bonds with hydrogen atoms on the nanoparticle surface. With respect to the susceptibility of functionalized Si-NPs towards oxidation, the particles functionalized with the esters show better shielding than dodec-1-ene. It is possible that the polar attraction between attached ester groups suppresses the diffusion of oxygen and water molecules towards Si-NPs surface and therefore provides better passivation against oxidation. Despite the fact that the functionalization efficiency of VB is the worst, the oxidation susceptibility is found to be the lowest (S_o = 1.4), which is probably due to the presence of bulky benzyl group in VB molecules as it can provide an extra barrier for the diffusion of oxygen and water molecules towards the Si-NPs surface.

Table 4.1. Relative efficiency of functionalization of different organic reagents and the oxidation susceptibility index of functionalized Si-NPs with respect to the type of organic ligands on their surface.

Organic reagent	Relative efficiency of functionalization	Oxidation susceptibility index (S_o)
Dodec-1-ene	1	2.59
EMP	0.95	2.03
ETU	1.29	2.50
VB	0.66	1.40

It is clear from above results that functionalized Si-NPs show higher stability compared to H-terminated Si-NPs but their long term stability is limited because of incomplete surface coverage. With respect to the oxidation susceptibility, the VB functionalized Si-NPs is found to be the best. Since the VB molecules can polymerize at elevated temperatures [152, 153], a higher converge of organic molecules on the surface of Si-NPs can not be achieved using VB. There-

fore, dodec-1-ene and ETU molecules are the best choices as their surface coverage is higher than EMP and can be increased further by functionalization at elevated temperature.

4.2.2.4 Quantum yield of functionalized Si-NPs

It is well known from the literature that the QY of Si-NPs and porous silicon is very low. The QY of porous silicon was reported in the range of 1–10% for most of the samples [154, 155]. Sankaran et al. [156] prepared blue luminescing Si-NPs and reported the QY of their particles of about 30%. Mangolini et al. [157] reported QY of their functionalized Si-NPs maximum up to 70%, however, their particles emitting below 700 nm show poor QY (< 5%).

The procedure for the measurement of QY is described in Sect. 3.2.7. Two different type samples were examined in this study, namely sample “A” and sample “B”. Both the samples in this study were prepared by etching the as-synthesized Si-NPs in a mixture of HF and HNO_3 and successive functionalization in dodec-1-ene at 120°C for 10 h. Sample “A” was prepared by using particles with d_p of about 13.2 nm and σ_g of 1.4 (see Fig. 4.4). For sample “B”, particles with d_p of about 4.3 nm and σ_g of 1.2 were used (see Fig. 4.5). For the QY measurement, first the baseline measurement was performed by using pure dodec-1-ene. Thereafter, the spectrum of dodec-1-ene functionalized Si-NPs dispersed in dodec-1-ene was recorded. After subtracting the baseline from the sample spectrum, the resulting spectrum shows two peaks for the absorption and emission of Si-NPs as shown in Fig. 4.29a. Finally, the QY of functionalized Si-NPs was calculated using equations (3.33)–(3.35). The normalized emission spectra from both samples are shown in Fig. 4.29b. Both samples show emission in the orange regime. Sample “A” and “B” emit around 678 nm and 665 nm, respectively. The QY values of sample “A” and “B” was about 1.4% and 15.4%, respectively. Mangolini et al. [157] observed that the QY of their functionalized Si-NPs changes with the emission wavelength. However, this can not be the case here as the emitting wavelength of both samples does not differ much. Therefore, the low QY in sample “A” can be attributed to the broad size distribution of particles and very small fraction of particles emitting in the visible regime (see Fig. 4.11b). The large fraction of bigger particles in the ensemble can absorb the emission from small nanoparticles, thereby decreasing the overall QY. This phenomenon is called self absorption [158]. This explanation is supported by the fact that the QY of single nanoparticles is much higher than particles in ensemble [159].

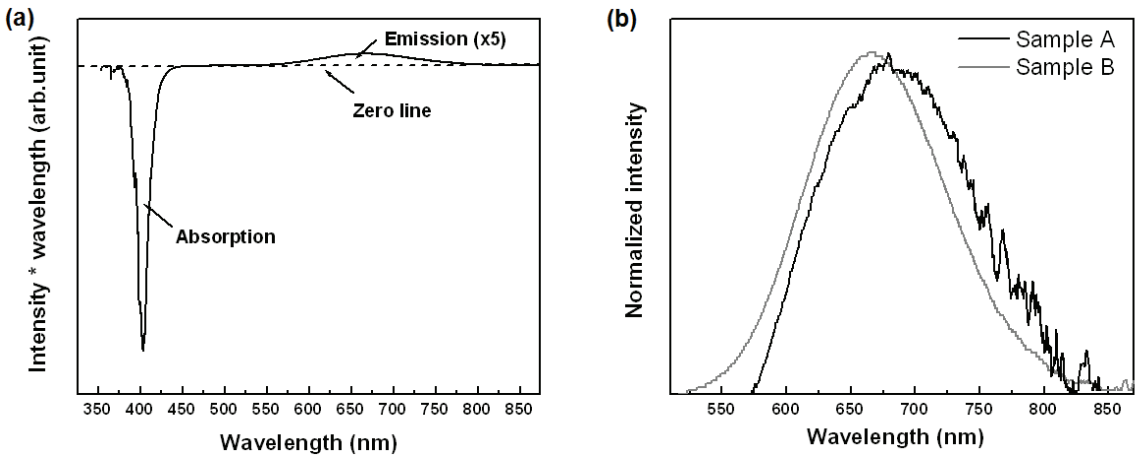

Fig. 4.29. (a) Sample measurement minus baseline measurement. (b) Normalized emission spectra of sample "A" and "B".

Due to very high QY, the functionalized Si-NPs show very bright luminescence upon excitation. It is easy to see luminescence from Si-NPs from extremely diluted concentration of particles in dispersion, which is completely transparent to human eyes as depicted in Fig.4.30.

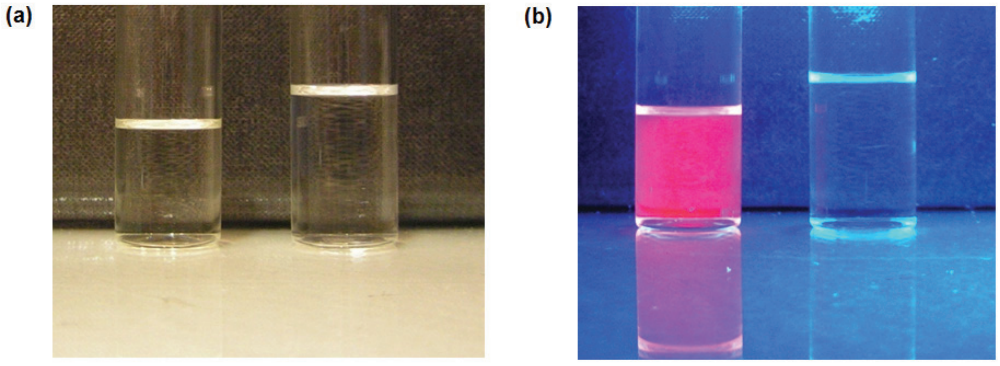

Fig. 4.30. Extremely diluted dispersion of dodec-1-ene functionalized Si-NPs in chloroform (left) and pure chloroform (right) in (a) normal daylight and (b) under UV illumination.

4.3 Electrical properties of Si-NPs

In our group, the size dependent electrical conductivity of as-synthesized Si-NPs has already been studied. It was observed that the electrical conductivity of as-synthesized Si-NPs decreases with decreasing size [160]. In this study, the influence of surface modification on the electrical conductivity of Si-NPs was examined. Due to the fact that small Si-NPs show very poor electrical conductivity, Si-NPs with a mean diameter of about 52 nm (see Fig. 4.2) were examined in this study. Thin pellets of Si-NPs were prepared by pressing the powder uniaxially and the electrical conductivity of pressed pellet was measured using impedance spectrometry (see Sect. 3.2.3 for details). The measurements were done under hydrogen atmosphere in order to avoid the oxidation of Si-NPs during the experiments.

The typical Nyquist diagram of the impedance measurements of Si-NPs in the temperature range between 100°C and 400°C is shown in Fig. 4.31. It is clear that the resistance of Si-NPs decreases with increasing temperature. All the samples under this study show similar behavior. The intercept of the semicircle at low frequency gives the total resistance (R_t), which can be converted into specific conductivity (σ) by,

$$\sigma = \frac{T_p}{R_t A_c} \tag{4.4}$$

where T_p is the thickness and A_c is the cross section area of the pellet.

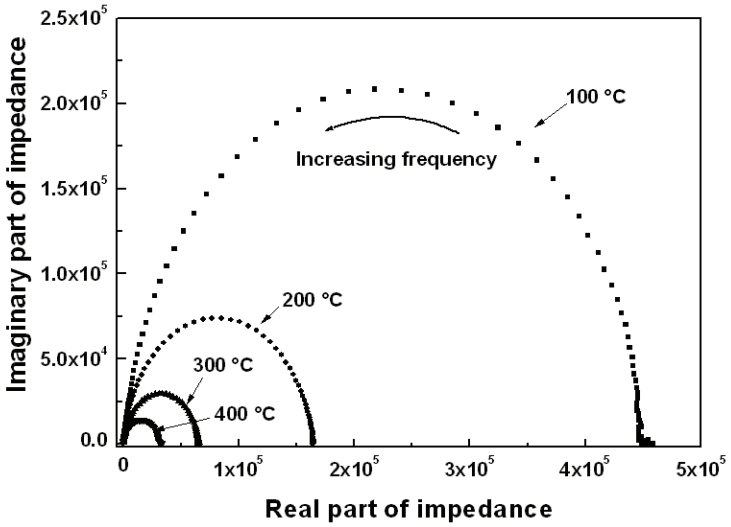

Fig. 4.31. The typical Nyquist diagram of the impedance measurements of Si-NPs at different temperatures.

Figure 4.32 shows the temperature dependent specific conductivity of as-synthesized Si-NPs. When the pellet is heated for the first time in hydrogen, the conductivity increases some orders of magnitude and remains significantly higher compared to the first measurement after the sample is cooled down. A less steep increase in the conductivity is observed during the second cycle compared to first measurement, however, pellet resembles its original conductivity. The third measurement shows exactly the same conductivity as observed in the second cycle. The difference in conductivity between first and second measurements can be attributed to annealing effects during the first cycle. This behavior is well known for powders and can be attributed to improved particle-particle contact during heating. It is observed from the XRD measurements that there was no growth of particles after the heating.

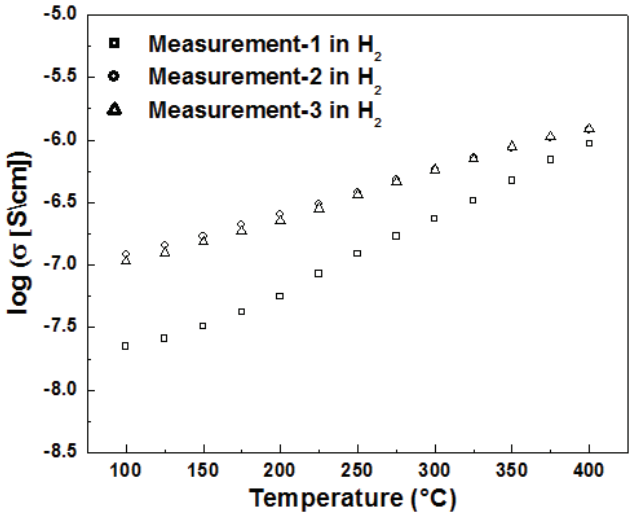

Fig. 4.32. Temperature dependent specific conductivity of as-synthesized Si-NPs.

In order to study the influence of surface modification on the electrical conductivity of Si-NPs, the electrical conductivity of as-synthesized Si-NPs was examined after HF etching, surface re-oxidation and surface functionalization. All the specific conductivity values shown below are taken from the second measurement cycle. The specific conductivities of different samples are compared at 100°C. A similar trend is observed at other temperatures too.

4.3.1 Influence of etching and surface re-oxidation

Figure 4.33a demonstrates the change in specific conductivity of as-synthesized Si-NPs after etching and surface re-oxidation. As can be seen, surface etching of Si-NPs increases their electrical conductivity almost by four orders of magnitude. As the crystallite size of as-synthesized Si-NPs is not influenced by etching with HF (as discussed in Sect. 4.1.3), the increase in conductivity of particles must originate only due to the removal of silicon oxide shell from the surface of Si-NPs. The removal of the oxide shell after etching, as evident by FTIR measurements (see Fig. 4.12), can increase the electron transport between Si-NPs due to decrease in resistance offered by highly resistive oxide layer.

The EPR measurements of as-synthesized and etched Si-NPs are shown in Fig. 4.33b. For the as-synthesized sample, the typical silicon dangling bond signal, composed of contributions from P_b-centers (represented by dashed black curve) and *D*-centers (represented by dotted

black curve), is observed. It is clear from the curve that the sum of these two contributions agrees nicely with the measured data (black solid curve). For the etched sample, the intensity of the defect signal is strongly reduced. This decrease in dangling bond concentration can be reliably correlated to the covalent attachment of H-atoms to the surface dangling bonds during the etching process. Interestingly, the relative contributions from the different dangling bond species have changed. In the spectrum of the etched Si-NPs, no measurable contribution from P_b-centers is observed, however, it has not a strong effect on the *D*-centers. The large concentration of dangling bonds on the surface of as-synthesized Si-NPs increases the probability that electrons are trapped there, therefore, it may lead to a decreased electrical conductivity. Hence, the decrease in overall dangling bond concentration of as-synthesized Si-NPs after etching may also enhance the electrical transport between Si-NPs.

The freshly etched Si-NPs were stored in air under ambient conditions and the electrical measurements were performed on these samples after 26 days and 188 days (Fig. 4.33a). A decrease in the conductivity of etched Si-NPs is observed due to their surface oxidation in air. The formation of oxide layer re-introduces the oxide barriers and therefore decreases the conductivity of Si-NPs. As the oxidation time increases, the conductivity of sample reduces further, which may be due to increased thickness of the oxide layer. Additionally during the oxidation of etched Si-NPs, the increased oxide layer reduces the core size of Si-NPs and therefore can also decrease the conductivity of particles by decreasing the volume ratio of silicon core and oxide layer. As if the volume ratio of silicon core and oxide layer decreases, the conduction electron has to travel comparatively larger distance in oxide layer compared to silicon core during the transportation process. It is clear from Fig. 4.33a that the conductivity of re-oxidized sample did not drop down to the conductivity of as-synthesized sample even after 188 days of surface oxidation. The EPR measurements of re-oxidized sample (Fig. 4.33c) confirm that the dangling bond concentration of re-oxidized sample is lower than as-synthesized sample. Therefore, one of the main reasons for the higher conductivity of re-oxidized sample is the lower dangling bond concentration. This observation do not concise with the observation of Pi et al. [28], where they found that oxidation of Si-NPs after HF etching results in increased dangling bond concentration compared to the oxidation of Si-NPs without HF etching. This discrepancy may arise due to difference in the synthesis method and oxidation time of the Si-NPs in both studies.

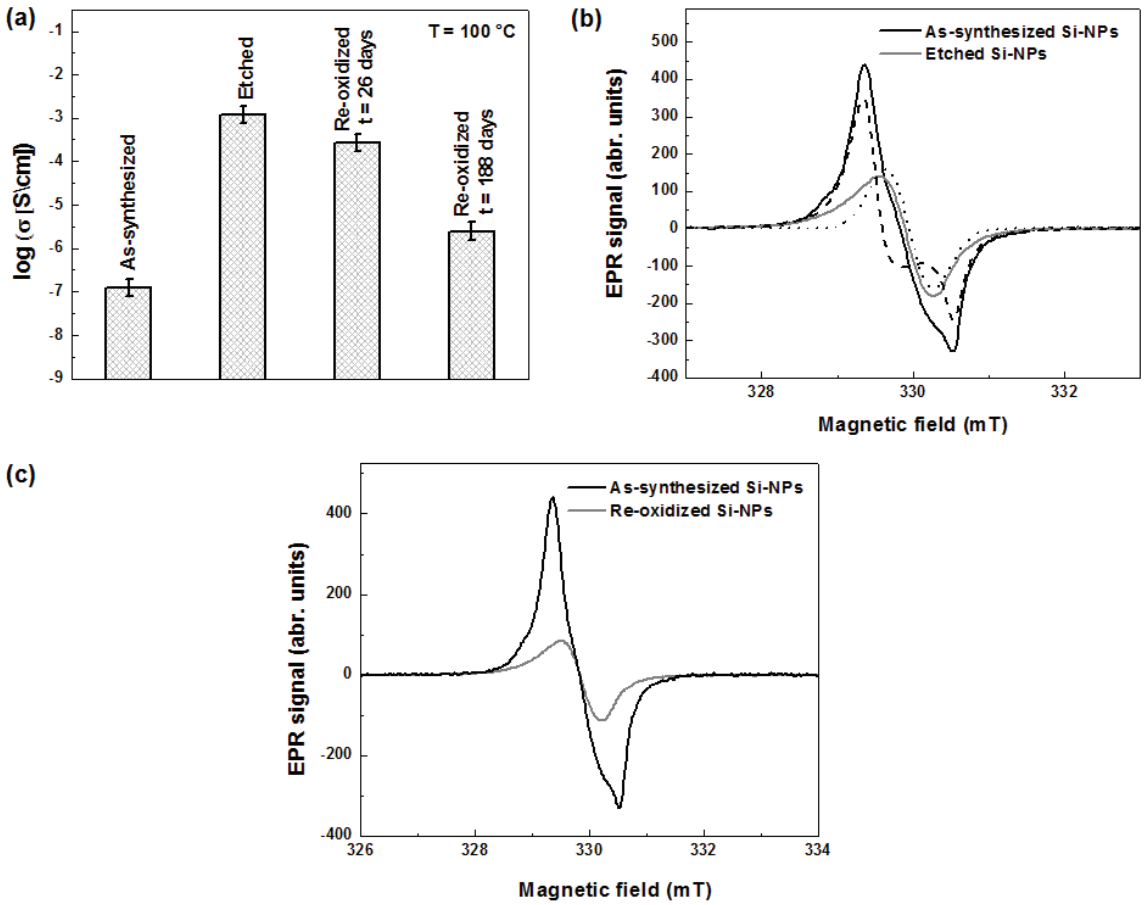

Fig. 4.33. (a) Specific conductivity of as-synthesized, etched and re-oxidized Si-NPs after 26 days and 188 days of surface oxidation in air. (b) EPR spectra of as-synthesized and etched Si-NPs. The measured spectrum of as-synthesized sample can be decomposed by computer simulation using the powder pattern of a paramagnetic state with axial symmetry (dashed line) and an isotropic contribution (dotted line). (c) EPR spectra of as-synthesized and re-oxidized Si-NPs. The EPR spectrum of re-oxidized sample was measured after 197 days of air oxidation of freshly etched sample.

4.3.2 Influence of surface functionalization

As the air oxidation of H-terminated Si-NPs deteriorates their electrical conductivity, the surface of freshly etched particles was functionalized with different alkenes (hex-1-ene (C_6), dec-1-ene (C_{10}), dodec-1-ene (C_{12}), tetradec-1-ene (C_{14}), and octadec-1-ene (C_{18})) via thermal induced hydrosilylation. The functionalization of Si-NPs with C_6 was accomplished at 80°C due to its low boiling point, whereas the functionalization with other alkenes was performed at 120°C. The functionalization was carried out for 10 h.

Figure 4.34a shows the specific electrical conductivity of functionalized Si-NPs together with as-synthesized and freshly etched sample. The measurements were performed under hydrogen atmosphere. It is observed that the conductivity of etched Si-NPs decreases after surface functionalization. During the surface functionalization, the organic molecules are attached on the surface of silicon and an organic shell around Si-NP is formed. The organic layer on the surface of Si-NP increases the barrier for the electron transport between particles and therefore decreases the electrical conductivity. Figure 4.34b demonstrates the change in dangling bond concentration of etched Si-NPs after surface functionalization with C_{12}. It is observed that the dangling bond concentration of Si-NPs decreases after the organic termination of Si-NPs. It is possible that the etched particles have degraded already to a certain extent before they were measured with EPR and therefore the functionalized particles show less dangling bonds concentration than freshly etched sample. Another explanation could be that the thermal treatment of Si-NPs during the surface functionalization has decreased the defect density.

While functionalization with alkenes from C_6 to C_{12} resulted in higher conductivity compared to the as-synthesized materials, samples functionalized with C_{14} and C_{18} showed very poor conductivity. As the length of organic ligands increases, the effective thickness of organic layer is expected to increase (Fig. 4.34c) and therefore lead to a decreased conductivity of Si-NPs. It is observed that the conductivity of Si-NPs decreases as the length of carbon chain increases from C_{12} to C_{18}, however, increasing the carbon length chain from C_6 to C_{12} show completely opposite behavior.

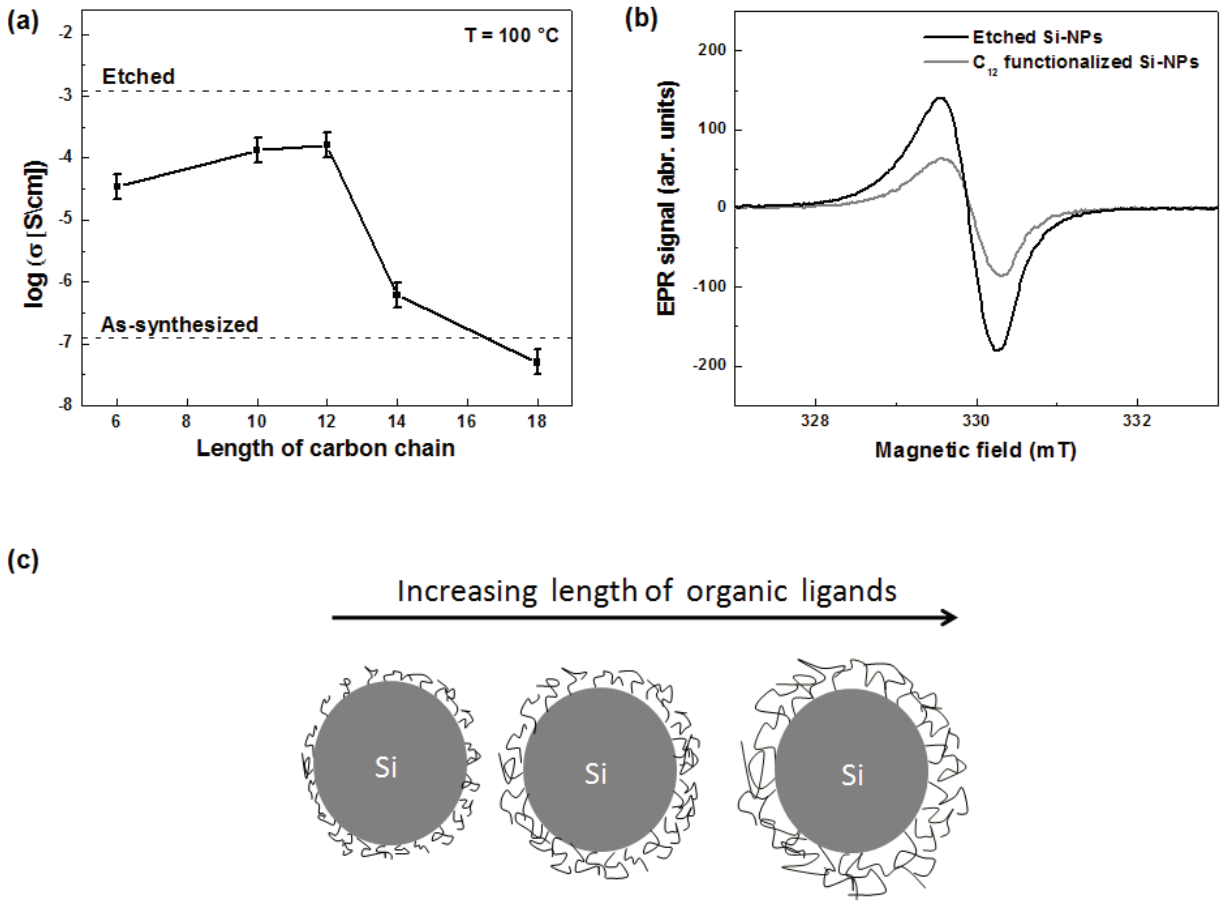

Fig. 4.34. (a) Specific conductivity of as-synthesized, etched and functionalized Si-NPs with different alkenes (C_6–C_{18}). (b) EPR spectra of etched and C_{12} functionalized Si-NPs. (c) Schematic illustration of increase in effective thickness of organic layer around Si-NPs with increasing carbon chain length.

In order to understand this anomalous behavior, the FTIR spectra of functionalized Si-NPs were analyzed. Figure 4.35 shows the FTIR spectra of different functionalized Si-NPs. It is observed that C_6 and C_{10} functionalized Si-NPs have relatively higher intensities of surface oxides (SiOSi and $SiHO_3$ stretching vibrations) compared to other functionalized samples. This is probably due to large number of remaining Si-H bonds and higher oxidation susceptibility of particles surface because of low steric hindrance of attached organic ligands. In Sect. 4.2.2.2, it is shown that the functionalization at low temperature results in lower surface coverage. This can explain the higher oxidation of C_6 functionalized Si-NPs compared to C_{10} because the functionalization with C_6 was carried out at lower temperature. The higher oxidation of C_6 functionalized Si-NPs compared to C_{10} and C_{12} functionalized sample increases the overall resistance of particle and therefore shows poor electrical conductivity.

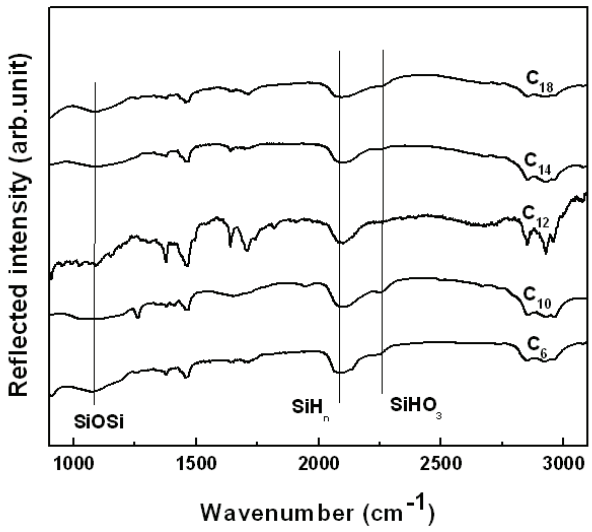

Fig. 4.35. FTIR spectra of C_6, C_{10}, C_{12}, C_{14} and C_{18} functionalized Si-NPs.

It has been observed that the electrical conductivity of zinc oxide (ZnO) increases in the presence of hydrogen [161-163]. In order to examine if there was any influence of hydrogen in the electrical conductivity of Si-NPs, the measurements were also performed in argon atmosphere. Almost no difference in the electrical conductivity of the samples is observed. As an example to illustrate, the electrical measurements performed on C_{12} functionalized particles in hydrogen and argon are shown in Fig. 4.36. A slight difference in the conductivity under both gaseous environments can be accounted to the experimental error in the measurements.

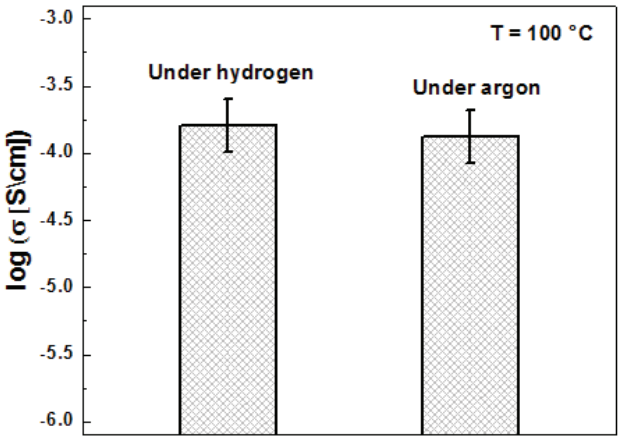

Fig. 4.36. Specific conductivity of C_{12} functionalized Si-NPs under hydrogen and argon.

The C_{12} functionalized Si-NPs show the highest conductivity among all n-alkyl terminated samples (Fig. 4.34a). In order to examine the stability of C_{12} functionalized Si-NPs in air,

the particles were exposed to air under ambient conditions. Figure 4.37a shows the FTIR spectra of freshly synthesized C_{12} functionalized Si-NPs and after 185 days of storage in air. A small increase in oxide vibrations (SiOSi and $SiHO_3$) together with a small decrease in SiH_n vibration is observed, indicating that the surface of particles is very stable against air oxidation. The electrical conductivity of stored sample was again measured and compared with freshly functionalized sample (Fig. 4.37b). Only a slight decrease in the electrical conductivity of functionalized particles is observed after six months of storage in open air.

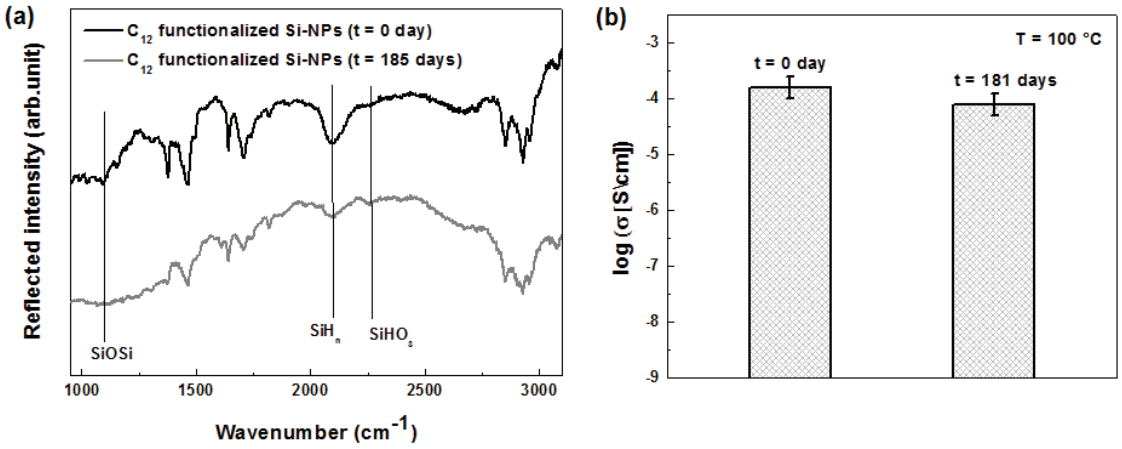

Fig. 4.37. (a) FTIR spectra, and (b) Specific conductivity of C_{12} functionalized Si-NPs before and after oxidation in air under ambient conditions.

4.4 Dispersion stability and ink-jet printing of Si-NPs

In this section, the stability of as-synthesized, etched and functionalized Si-NPs dispersion is examined. Additionally, it is shown that the functionalized Si-NPs can be used to print structures on a substrate.

4.4.1 Stability of Si-NPs dispersion

The particles with mean diameter of about 4.3 nm were examined in this study (see Fig. 4.5). The freshly etched Si-NPs are prepared by etching the as-synthesized Si-NPs in HF. It is shown earlier in Sect. 4.2.2.3 that ETU functionalized Si-NPs show the highest surface coverage compared to other alkenes under this study. Therefore, the surface functionalization of Si-NPs was carried out with ETU at 120°C for 10 h.

Figure 4.38a,b shows a schematic representation of as-synthesized, freshly etched and functionalized Si-NPs dispersion together with their dispersion stability in air under ambient conditions. It is observed that as-synthesized Si-NPs are very difficult to disperse because the particles are highly agglomerated (Fig. 4.38c). Additionally, the presence of oxide shell around the Si-NPs also limits the choice of dispersion medium for as-synthesized particles. It is seen that as-synthesized Si-NPs can be dispersed in de-ionized water but not without ultrasonic agitation. The dispersion of as-synthesized Si-NPs in de-ionized water is shown in Fig. 4.38b (vial “A”). The dispersion is visibly turbid due to presence of agglomerates. The average diameter of agglomerated as-synthesized Si-NPs measured using dynamic light scattering was about 117 nm (see Fig. 8.6a of Appendix A), which is about 28 times larger than their mean particle diameter. It is found that the zeta potential of the dispersion is not very high (< 40 mV, Fig. 8.6b of Appendix A), as a result a significant sedimentation of particles is observed after 2 hours. The etching of Si-NPs with HF removes the oxide layer and breaks the agglomeration of Si-NPs (see Fig. 4.12, Sect. 4.1.3). However, it is found that the etched Si-NPs also do not form a stable dispersion in solvents because of the re-oxidation of particle. Also, etched Si-NPs are aggregated due to formation of oxide layer around them (see Sect 4.1.1). As an example to demonstrate, the dispersion stability of etched Si-NPs in chloroform is shown in Fig. 4.38b (vial “B”). A significant

agglomeration of particle can be seen after 1 days of storage. The functionalization of freshly etched Si-NPs with organic molecules using hydrosilylation process provides passivation against surface re-oxidation. Additionally, the organic layer on the surface of Si-NPs provides steric hindrance for the further agglomeration of particles. The functionalized Si-NPs can be dispersed in organic solvent without any sonication due to presence of organic layer on their surface. In Fig. 4.38b (vial “C”), the dispersion of functionalized Si-NPs in ETU solvent is shown. However, it is seen that after separating the functionalized Si-NPs from their respective alkenes, the particles can be re-dispersed in a variety of organic solvents (such as chloroform, toluene, n-hexane etc.) and the dispersion is extremely stable. The functionalized Si-NPs form a clear dispersion due to presence of non-agglomerated particles (Fig. 4.38c). The preservation of a non-polar particle surface provides better dispersability and long-term stability in organic solvents. The average diameter of functionalized Si-NPs measured using dynamic light scattering was about 28 nm, which is bigger than the mean particle diameter of as-synthesized Si-NPs due to the coating with organic molecules and probably some remaining agglomeration. No reasonable change in hydrodynamic diameter of functionalized Si-NPs is observed after 1 week of storage (see Fig. 8.7 of Appendix A), indicating that the dispersion is stable with time and no sedimentation of functionalized Si-NPs was observed even after eight months (visible inspection). The functionalized Si-NPs can also be dispersed in aqueous solvents by using hydrophilic ligands [164].

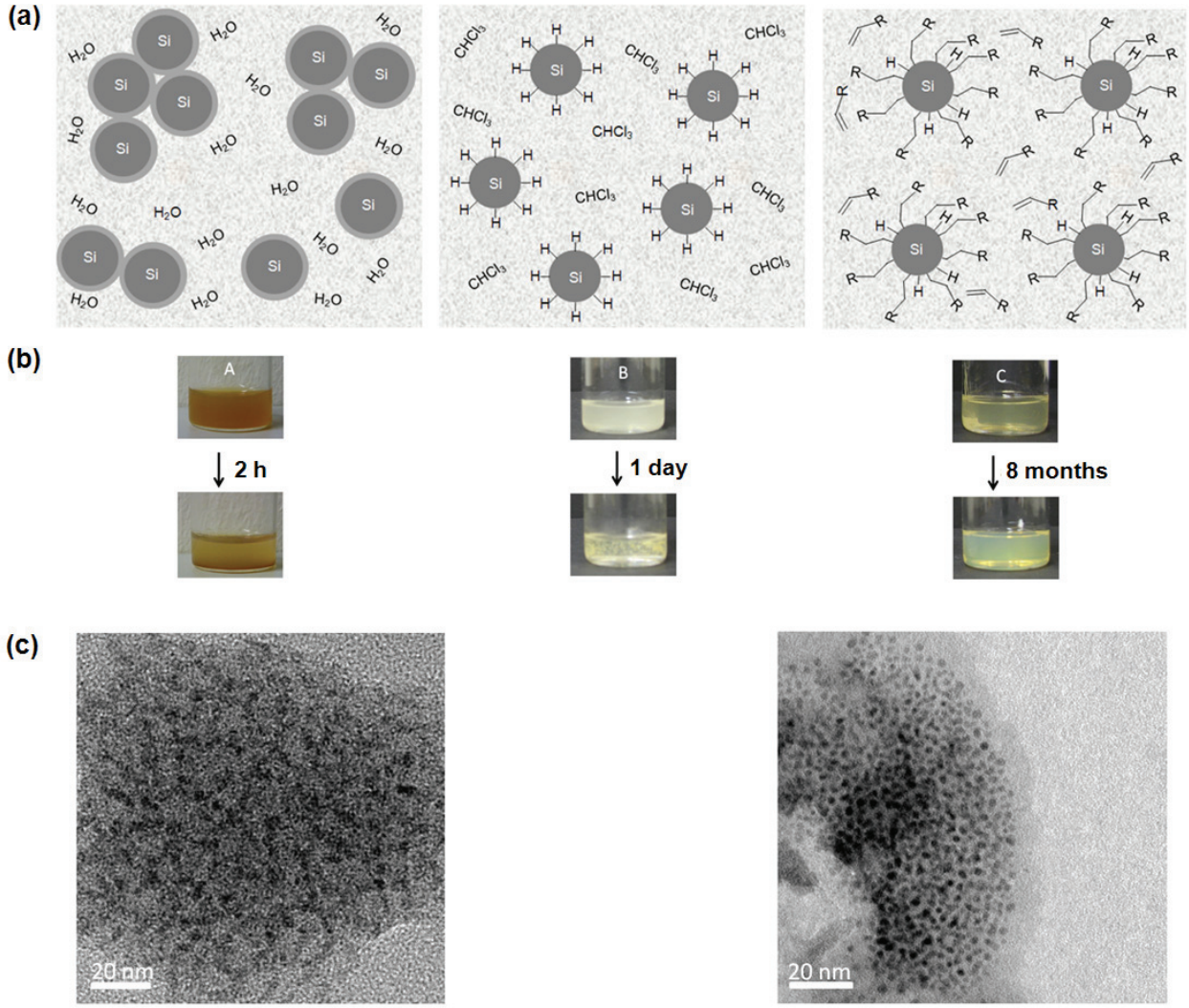

Fig. 4.38. (a) A schematic representation, and (b) the dispersion stability of as-synthesized (sample A), freshly etched (sample B) and functionalized Si-NPs (sample C) dispersion in deionized water, chloroform and ETU solvent, respectively. (c) Bright field TEM image of as-synthesized (left) and functionalized (right) Si-NPs.

4.4.2 Printing of functionalized Si-NPs

As the dispersion of functionalized Si-NPs is very stable, it can be used to print structures on a substrate. The printing of functionalized Si-NPs was performed using mask and ink-jet printing. As an example, the mask printed layer of yellow-orange and red luminescing functionalized Si-NPs on a glass substrate is shown in Fig. 4.39. These particles were prepared by etching of Si-NPs (d_p ~ 13.2 nm, Fig. 4.4) with a mixture of HF and HNO_3 for different times and subsequent

surface functionalization with ETU at 120°C for 10 h. Before printing, the functionalized particles were separated from their alkene solution by centrifugation. Thereafter, the particles were re-dispersed in methanol and the dispersion was poured drop by drop on a glass substrate using a mask. Thin layer of functionalized Si-NPs was formed on a glass substrate by subsequent drying of particles at room temperature.

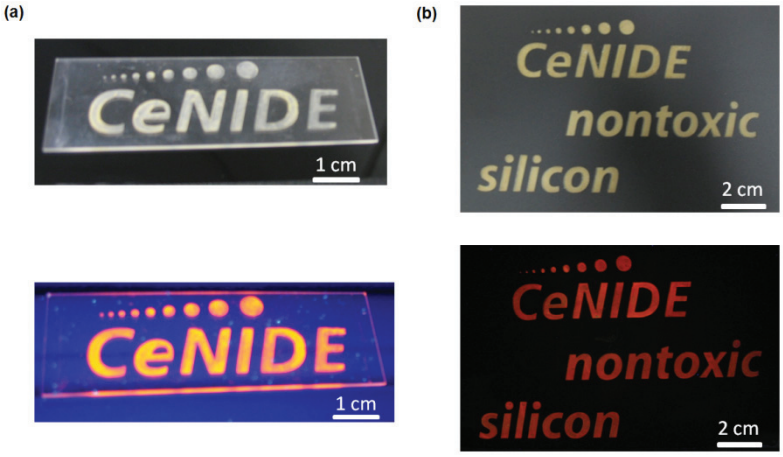

Fig. 4.39. Photographs of functionalized Si-NPs printed on a glass substrate using mask in normal daylight (top) and under UV illumination (bottom): (a) Using yellow-orange luminescing, and (b) red luminescing particles.

Printing technology like screen-printing and spin coating are not useful if the concentration of particles in the dispersion is very low. Additionally, these technologies need masks to write a well-defined pattern. Using ink-jet printing, the deposition of very small volume of suspensions in a well-defined pattern is possible and the direct structured deposition removes the need for masks leading to an efficient use of material. Moreover, ink-jet printing offers the deposition of nanoparticle dispersions with very low concentration due to the possibility of multilayer printing.

An ink with very low concentration of particles (~ 0.4 wt. %) was prepared, which show bright orange luminescence upon excitation with UV light (Fig. 4.40a). These particles were prepared by etching of Si-NPs (d_p ~ 4.3 nm, Fig. 4.5) with HF and subsequent surface functionalization with ETU at 120°C for 10 h. Nine layers of Si-NPs were printed from their ETU dispersion on the glass substrate in a layer-by-layer fashion using ink-jet printing (see Sect. 3.1.4 for details). After printing, the structure was completely invisible to the unaided eyes because of very high transparency of the printed thin film. However, when the printed structure was illuminated

with the UV light, the functionalized Si-NPs show visible luminescence. Figure 4.40b shows the picture of nine layers of a printed structure under UV illumination. The luminescence color of the printed structure can hardly be seen under UV illumination because of the high intensity of the reflected UV light. The PL emission spectra recorded from the printed structure and from the dispersion are shown in Fig. 4.40c. After printing one layer, the structure shows an emission peak at 575 nm, however, the one with nine printed layers shows a strong red shift in the spectrum and emits at about 660 nm. This phenomenon can be attributed to self-absorption within the emitting material [158]. In case of nine printed layers, the PL from small nanoparticles that emit at shorter wavelength is suppressed due to the absorption from bigger particles which then emit at higher wavelength. The probability of absorption of emission from small nanoparticles by big particles increases as it passes through many layers. Similarly in the PL spectrum of dispersion, the emission from the small nanoparticles at about 575 nm is suppressed by big particles and therefore it shows a main peak around 660 nm and a shoulder at 575 nm.

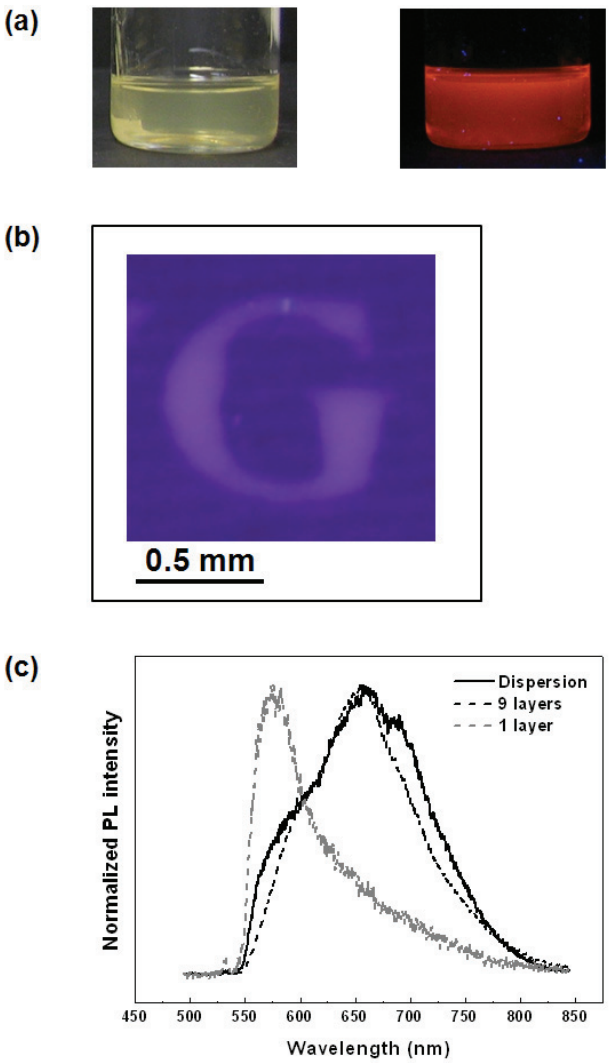

Fig. 4.40. (a) ETU functionalized Si-NPs dispersion in normal daylight (left) and under UV illumination (right). (b) Photograph of an ink-jet printed functionalized Si-NPs structure on glass substrate under UV illumination. (c) PL emission spectra from the dispersion, one ink-jet printed layer and nine ink-jet printed layers of functionalized Si-NPs.

The homogeneity and uniformity of printed Si-NPs films was analyzed by PL scanning. The structure "G" was scanned in two-dimensions using intensity integration from 500 nm to 850 nm and a two-dimensional intensity map was created. With this intensity mapping the concentration distribution of particles at different position in the printed structure was analyzed. Figure 4.41 shows the two-dimensional intensity profile of a printed "G" (consisting of nine layers) before and after annealing. The as-prepared structure does not show a homogenous distribution of particles over the entire structure as evidenced by a strong variation of the intensity within the pattern. The particles are mostly concentrated, where the structure is relatively wide. At a partic-

ular place, the concentration of particles is high at the center and decreases towards the edges. In addition to that the printed "G" has not well-defined edges. The inhomogeneity of the printed "G" is mainly due to the slow drying of the printed layers. For our experiments, the substrate was heated up to 60°C, which is the maximum possible temperature of the substrate heater used. This temperature is very low compared to the evaporation temperature of ETU solvent (BP = 258°C), therefore, the printed layers are still 'wet' even for longer delay times between the over printing. Therefore, the film was annealed in N_2 atmosphere at 300°C for 1 h. After annealing, the distribution of particles was more homogenous due to the evaporation of the solvent (Fig. 4.41b). It is known from the literature that the morphology of deposited particles depends on various factors, such as particles concentration and choice dispersion medium [165]. Therefore, by optimizing these parameters, more homogeneous and well defined pattern of Si-NPs can be obtained. After annealing, the thickness of the printed structure was measured using XP-200 profilometer (Ambios Technology) and found to be between 100–240 nm.

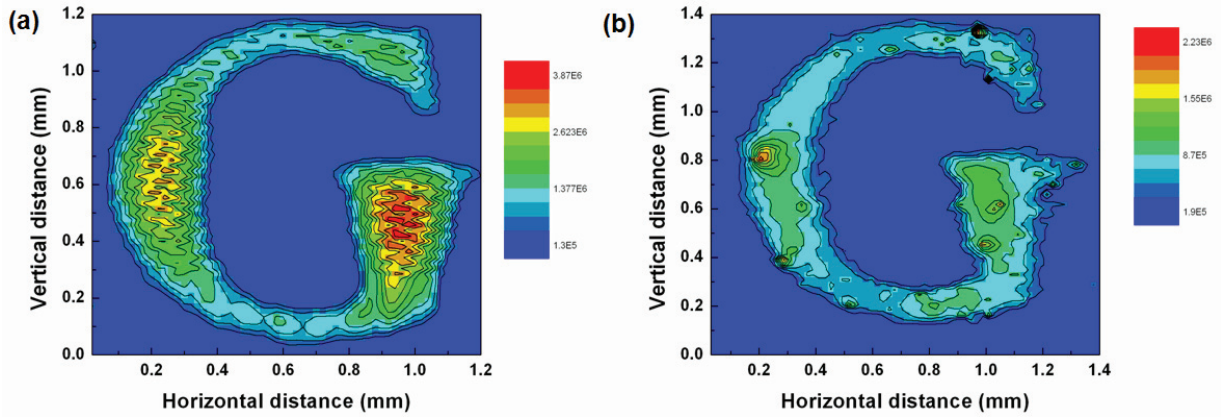

Fig. 4.41. Two-dimensional intensity maps of the printed structure "G" (a) before, and (b) after annealing.

4.5 Synthesis of cross-linked Si-NPs network

The particles are arranged in two- or three-dimensions after the printing, which can also be achieved by cross-linking of nanoparticles. The printing creates an artificial arrangement of particles, whereas the cross-linking of nanoparticles allows them to form interconnected particles. The cross-linked nanoparticles exhibit new properties, which are quite different from individual particles. It has been observed that the size of nanoparticles and the inter-particle spacing play a crucial role in controlling the properties of networked nanoparticles. For example, Storhoff et al. [63] observed that the optical property of cross-linked Au nanoparticles through DNA depends on the DNA linker length. Brust et al. [62], studied the electrical properties of Au nanoparticles cross-linked with dithiol. They observed a strong dependence of the electrical properties on the size of nanoparticles and the length of the spacer layer. Simon et al. [61] observed that the activation energy, which is needed for the hopping of the electron from one particle to another particle during the transportation process, increases after inserting the spacer molecule between $Pd_{561}phen_{36}O_{200}$ nanoparticles.

In this section, an approach to form Si-NPs network by the cross-linking of particles with organic spacer molecules is presented. The key idea is to use the bifunctional organic molecules, which can bind Si-NPs from both sides. Since alkyl terminated Si-NPs are obtained by hydrosilylation of H-terminated Si-NPs with alkene, the cross-linking of particles can be achieved via surface functionalization with bidental alkenes (such as 1,7-octadiene).

Figure 4.42 shows the simplified sketch of the formation of silicon-organic networks by the cross-linking of Si-NPs with bifunctional spacer molecules (1,7-octadiene). The presence of C=C bond at both end of 1,7-octadiene molecules allow them to bond with two Si-NPs and therefore this reaction leads to the formation of a three-dimensional network of particles interconnection through organic molecules (Fig. 4.42b). It should be noted that not all 1,7-octadiene molecules, after the attachment of Si-NPs from one side, can bind Si-NPs from another side due to large steric hindrance. It is also possible that C=C bond at both ends of 1,7-octadiene molecule are bonded to the same nanoparticle.

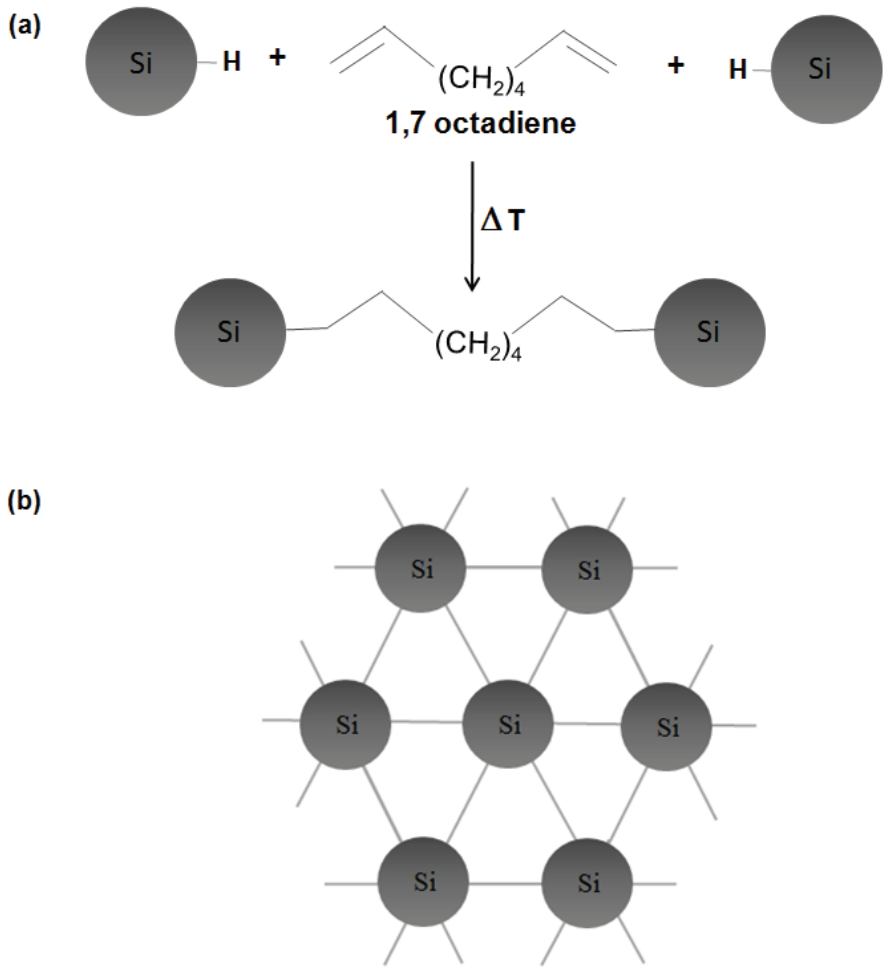

Fig. 4.42. Formation of silicon/organic networks by the cross-linking of Si-NPs with bifunctional spacer molecules: (a) A schematic illustration of the binding of two Si-NPs during the surface functionalization with 1,7-octadiene, and (b) a theoretical view of resulting cross-linked Si-NPs network in two-dimensions.

In order to increase the coverage of Si-NP, the smaller particles (d_p ~ 4.3 nm, Fig. 4.5) were used in this experiment. Due to low boiling point of 1,7-octadiene (BP = 121°C), the surface functionalization was carried out at 100°C for 10 h. In order to examine the differences originating due to use of bidental alkene, the surface functionalization of Si-NPs with monodental alkene (dodec-1-ene was used in this experiment) was also performed under similar conditions.

Figure 4.43 shows the dispersion of as-synthesized, freshly etched, dodec-1-ene functionalized, and 1,7-octadiene functionalized Si-NPs in normal daylight and under UV illumination. The luminescence from as-synthesized Si-NPs is very hard to see under UV illumination, however, they start to luminesce bright red after HF etching. The origin of intense luminescence

in etched Si-NPs has already been explained in Sect. 4.2.1.1. It can be seen clearly that both dodec-1-ene and 1,7-octadiene functionalized Si-NPs show visible luminescence under UV illumination, however, the color of emitting light is different. In contrast to the modification of Si-NPs with dece-1-ene, the functionalization with 1,7-octadiene results in the agglomeration of particles as revealed by visibly turbid dispersion and the sedimentation of large agglomerates at the bottom of the vial (indicated by arrow in Fig. 4.43d).

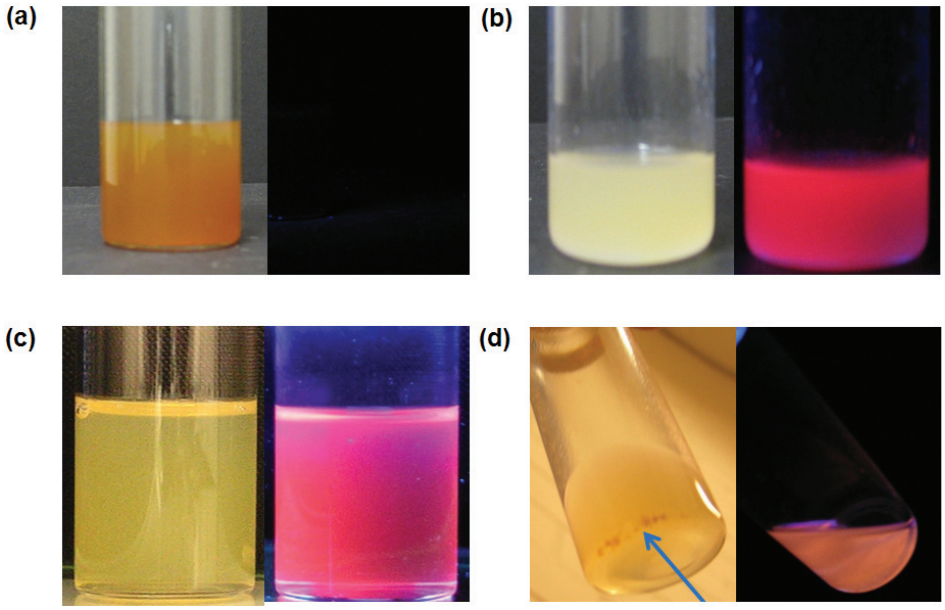

Fig. 4.43. Dispersion of (a) as-synthesized, (b) freshly etched, (c) dodec-1-ene functionalized, and (d) 1,7-octadiene functionalized Si-NPs in normal daylight (left) and under UV illumination (right). The as-synthesized and freshly etched particles are dispersed in methanol, whereas the functionalized particles are dispersed in their respective alkenes. The arrow in (d) shows the sedimented particles at the bottom of the vial.

In order to confirm that the functionalization of particles occurred and sedimentation is not observed due to the agglomeration of etched Si-NPs, TEM and FTIR investigations on these particles were performed. The particles were separated from their respective alkene by multiple centrifugations. After each centrifugation, the particles were re-dispersed in pure methanol. At the end, the particles were dried in vacuum in order to remove any physisorbed organic from their surface. Figure 4.44 shows the FTIR spectra of dodec-1-ene and 1,7-octadiene functionalized Si-NPs together with pure dodec-1-ene and 1,7-octadiene. As expected, the signature of unreacted SiH_n and SiOSi vibration is present in the spectra of both functionalized particles around 2100 cm^{-1} and 1085 cm^{-1}, respectively. The peak from $SiHO_3$ vibration around 2260 cm^{-}

[1] is also seen in the spectrum of dodec-1-ene functionalized Si-NPs. The signals from C=C stretching vibration at 1640 cm^{-1} [157] and –CH=CH_2 bending mode at 997 cm^{-1} [157] are completely absent in the spectrum of dodec-1-ene functionalized Si-NPs. The fact that we still see C=C stretching and –CH=CH_2 bending vibration in the spectrum of 1,7-octadiene functionalized Si-NPs are due to spacer molecules that are linked at only one side to the Si-NPs and still bear the C=C group at the opposite end. Thus, affirming that not all spacers contribute to the cross-linking of the particles.

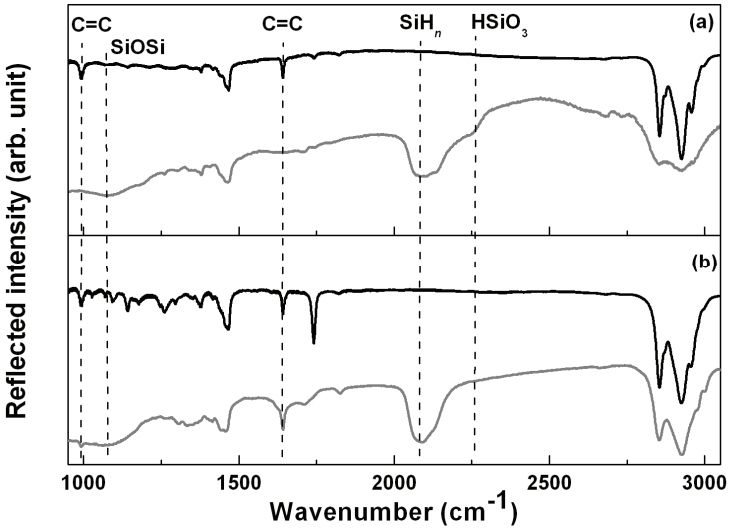

Fig. 4.44. FTIR spectra of pure alkene (black curve) and functionalized Si-NPs (gray curve): (a) Surface functionalization with dodec-1-ene, and (b) 1,7-octadiene.

The cross linking of 1,7-octadiene functionalized Si-NPs is also confirmed by TEM. Figure 4.45 shows the TEM pictures of dodec-1-ene and 1,7-octadiene functionalized Si-NPs. It can be seen clearly that the particles functionalized in dodec-1-ene are non-agglomerated, whereas functionalization with 1,7-octadiene results in highly agglomerated particles. Indeed, the individual particles are not visible in the TEM images because of the high degree of cross-linking. As from Fig. 4.45b one can only see the two-dimensional projection of cross-linked nanoparticles, the images from the samples are captured during the rotation of sample inside the TEM to see the extension of connecting nanoparticles in three-dimensions (Fig.4.46). The movie prepared by combining all consecutive images can be found in Ref. [166].

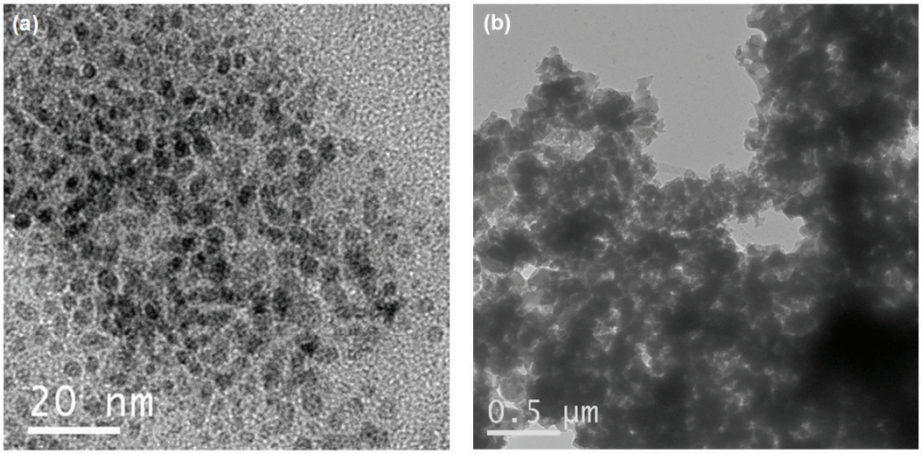

Fig. 4.45. Bright field TEM image of (a) dodec-1-ene, and (b) 1,7-octadiene functionalized Si-NPs.

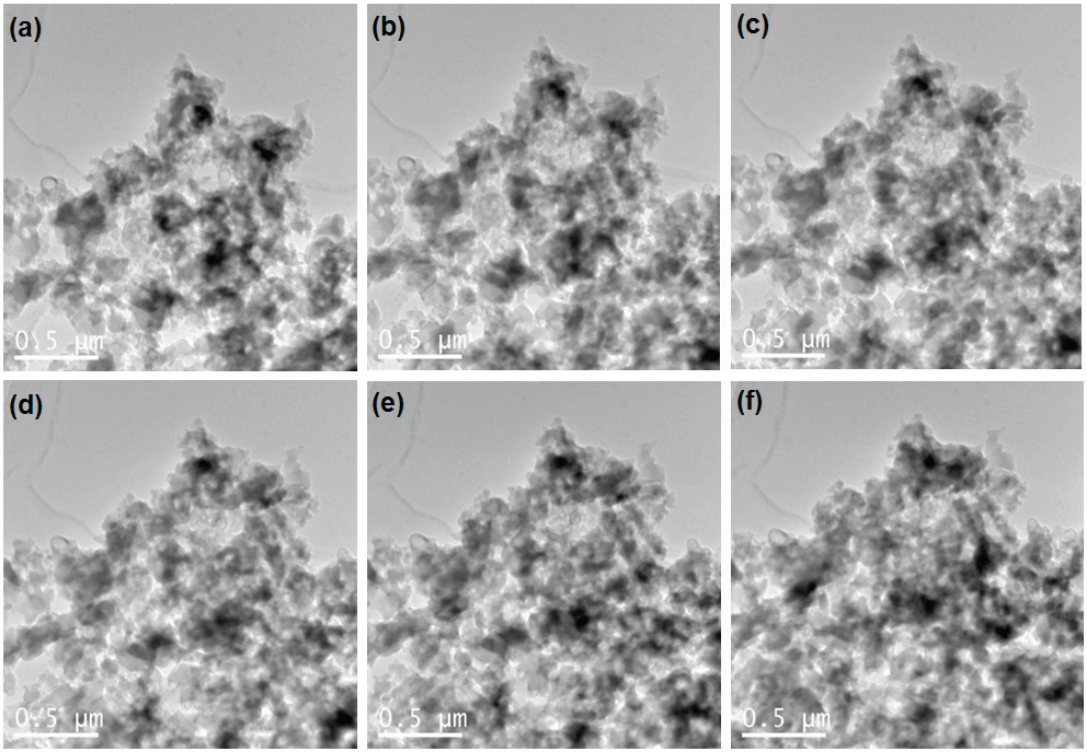

Fig. 4.46. Bright field TEM images of 1,7-octadiene functionalized Si-NPs. The images from (a) to (f) are taken by rotating the sample inside the TEM with increasing rotation angle.

The difference in emission color of dodec-1-ene and 1,7-octadiene functionalized Si-NPs is verified by PL measurements. Figure 4.47 shows the emission spectra of freshly etched, dodec-1-ene functionalized and 1,7-octadiene functionalized Si-NPs. It is observed that like other monofunctional alkenes including dodec-1-ene, functionalization of red emitting etched Si-

NPs with 1,7-octadiene also showed blue shift. However, the magnitude of shift and the structure of PL spectrum are quite different from dodec-1-ene functionalized Si-NPs. Further studies are needed to correlate the PL behavior of Si-NPs with their cross-linked structure.

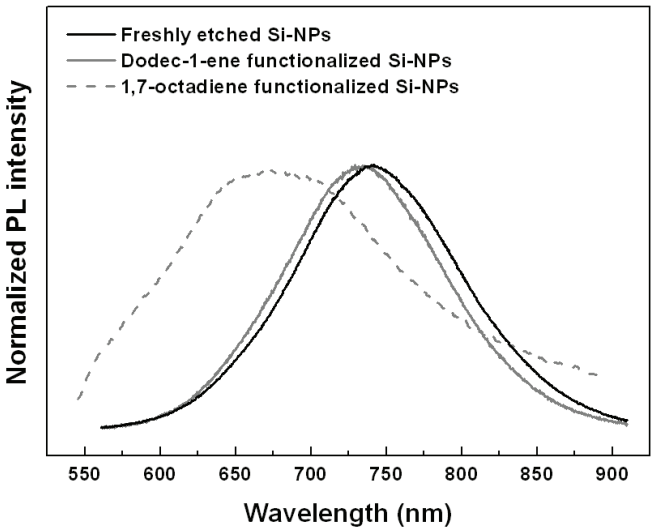

Fig. 4.47. Normalized PL spectra of freshly etched, dodec-1-ene functionalized and 1,7-octadiene functionalized Si-NPs.

5 Summary and conclusions

The discovery of efficient light emission from nanocrystalline silicon compared to bulk opened up the possibility to develop optoelectronic devices based on silicon [12, 167, 168]. However, it is observed that silicon is very prone to oxidation in the presence of air, which deteriorates its optical and electrical properties [25, 38-40]. To prevent oxidation, the surface of silicon can be passivated with organic molecules through Si-C bonds [78]. As surface plays a very important role in governing the properties of nanoparticles, modification of silicon nanoparticles (Si-NPs) surface may alter their properties. Therefore, a high technological interest exists to understand the influence of surface modification on the optical, electrical, and dispersion properties of Si-NPs for the realization of silicon based printable optoelectronic devices.

The main objective of the present work was to study the influence of surface modification on the optical, electrical and dispersion properties of Si-NPs. During this research, several interesting properties were explored, which are broadly associated with the surface chemistry of Si-NPs and defects on their surface. The results obtained in present research are briefly summarized below.

The Si-NPs, investigated in this thesis, are synthesized in a low-pressure microwave plasma reactor via pyrolysis of SiH_4. The as-synthesized particles are highly crystalline in nature and showed the presence of an amorphous oxide layer on their surface due to oxidation of particles in air. Additionally, due to collision of particles inside the reactor and surface oxidation of particles outside the reaction chamber, significant agglomeration of particles is seen. The surface of as-synthesized Si-NPs is passivated with organic molecules by etching them in hydrofluoric acid (HF) and subsequent surface functionalization with alkenes. Nearly complete removal of oxides from the surface of Si-NPs is observed after HF etching. TEM images showed that functionalization particles are mostly non-agglomerated, indicating that etching and functionalization processes resolve the agglomeration of Si-NPs.

It is observed that the as-synthesized Si-NPs with oxide layer have a high concentration of dangling bonds on their surface. The presence of these dangling bonds suppresses the radiative recombination of excitons and as a result as-synthesized Si-NPs show very weak photoluminescence (PL). A strong decrease in the dangling bond concentration of as-synthesized Si-NPs is observed after etching them with HF. This causes an increase in their PL intensity approximately by a factor of 20. It is seen that the etching of as-synthesized Si-NPs also contributes to a small blue shift in their spectrum ($\Delta\lambda$ = 36 nm). With increased etching of Si-NPs in a mixture of HF and HNO_3, a shift of the PL emission from red to green is obtained. This confirmed that red to green PL emission of Si-NPs is due to quantum confinement effects. The blue emission cannot obtained from further etching. It is found that surface oxidation of Si-NPs almost completely quenches the PL emission of most of Si-NPs after some time, which compares well with previous observations [25, 169]. However, during the oxidation of orange luminescing Si-NPs, material with blue photoluminescence is formed while the orange emission disappears. The peak of blue luminescence did not change its position during the oxidation and an increase in the PL intensity with increasing oxidation time is seen. These results indicate that the blue luminescence originates from defect states and not from the quantum confinement.

The stability of Si-NPs against surface oxidation was also examined in this study. The functionalized Si-NPs showed higher stability in air compared to freshly etched Si-NPs. However, incomplete surface coverage of Si-NPs with organic molecules limits their long-term stability. The particles functionalized with different organic substances showed different surface coverage and thus difference in long-term stability in air. The functionalization of Si-NPs using thermally induced hydrosilylation gives the best surface coverage with dodec-1-ene among all n-alkenes. The optimum temperature and time for the surface functionalization is found to be 120°C and 10 h. The Si-NPs terminated with ester groups showed higher stability against oxidation in air compared to dodec-1-ene. Additionally, it is seen that the use of reactants with bulky organic groups further decreases the oxidation susceptibility of the particles.

The functionalized Si-NPs show bright and stable PL for months (visible inspection). Also, the functionalized Si-NPs show high quantum yield (~15%). However, it is seen that functionalization process does not stabilize the original luminescence from freshly etched Si-NPs. The particles emitting in orange to red and yellow to green regime show a blue and red shift after

their surface functionalization, respectively. It is observed that the magnitude of the spectral shift can be altered by changing the coverage of organic molecules on the Si-NPs surface. The particles with high surface coverage show higher shift compared to particles with low surface coverage. Because a high surface coverage of organic molecules is needed to generate Si-NPs with long-term stability, materials that emit in the red to yellow range can be stabilized with this process, but stable materials with green emission are not achieved due to switching of the nature of shift (red/blue) in the orange-yellow region. Stable blue emission is obtained from the oxidation of orange emitting etched Si-NPs.

The electrical conductivity of as-synthesized Si-NPs (d_p ~ 52 nm) is found to be very low ($\sigma \sim 10^{-7}\ \Omega^{-1}\text{cm}^{-1}$ at 100°C). Etching of particles with HF increases their electrical conductivity by four orders of magnitude ($\sigma \sim 10^{-3}\ \Omega^{-1}\text{cm}^{-1}$ at 100°C). However, the freshly etched Si-NPs do not show stable conductivity in air due to surface oxidation. A decrease in the electrical conductivity of etched Si-NPs is seen with increasing oxidation time. The conductivity of oxidized Si-NPs is found to be higher than as-synthesized samples even after six months of exposure to air. It is observed that the functionalization of freshly etched Si-NPs also decreases their electrical conductivity. Additionally, the conductivity of functionalized Si-NPs can be tuned by changing the length of organic ligands. Among all n-alkenes, the functionalization of Si-NPs with dodec-1-ene exhibits the highest conductivity. Furthermore, the electrical conductivity of dodec-1-ene functionalized Si-NPs is found to be very stable in air.

It is seen that the stability of as-synthesized Si-NPs dispersion is limited due to the presence of big agglomerates and surface oxides. Etching and functionalization of Si-NPs causes the de-agglomeration of particles and the presence of organic molecules allows them to form stable dispersion in a variety of organic solvents. The stable dispersion of functionalized Si-NPs is used to print structure on glass substrate.

For the cross-linking of Si-NPs, functionalization of particle surface with bifunctional organic molecules is proposed. The bifunctional organic molecules can be bonded to the particles through both functional groups and therefore can cause a cross-linked network. In this work, successful cross-linked Si-NPs structure is accomplished by functionalization of particles using 1,7-octadiene.

In conclusion, the inadequacy of PL stability, poor electrical property and limited number of choice of dispersion medium for as-synthesized Si-NPs preclude them for practical applications. The etched Si-NPs show improved optical and electrical properties, however, these particles are not stable in air due to surface oxidation. In contrast, the functionalized Si-NPs show very good and stable photoluminescence, electrical, and dispersion properties. Therefore, they are a good candidates for future printable optoelectronic device applications.

The present research work provides a path for the production of highly stable Si-NPs ink with tunable optical and electrical properties, and paves the way for the application of silicon based low cost printable optoelectronics.

6 Recommendations for future work

The knowledge gained from this work can be utilized to extend the research in Si-NPs in various directions. Some of the research recommendations are listed below.

As discussed in this thesis, the PL emission of functionalized Si-NPs can be tuned by changing the organic ligands on their surface. In future, the effect of organic ligands on the PL life time and quantum yield can be examined. Additionally, it has been observed that the quantum yield of CdSe/ZnSe core-shell structures capped with organic molecules depends on the length of organic ligands on their surface [170]. If similar effects are observed in Si-NPs, particles with improved quantum yields can be prepared.

In this work, it was found that the electrical conductivity of Si-NPs can be tuned by changing the functional group on their surface. Additionally, it was demonstrated that Si-NPs can be cross linked to each other using bifunctional organic molecules. The cross linking of Si-NPs could result in the enhanced electrical conductivity compared to particles that are not linked to each other, as then the electrons do not have to cross the tunneling barrier while moving from one particle to another. The use of conductive spacer layers can further enhance the electron transport between particles. Furthermore, the use of connecting molecules with different spacer length can also influences the electrical conductivity of cross-linked particles. It would be interesting to explore all these features.

In the research presented here, it was shown that highly stable ink from functionalized Si-NPs with tunable optical and electrical properties can be prepared. Additionally, it was shown that these particles can be used to print the structures on a substrate. It is known from literature that the morphology of deposited particles depends on various factors, such as particle concentration and choice of the dispersion medium [165]. Because the performance of a printed device depends on the quality of the printed layer, the optimization of different parameters influencing

the quality of the printed layer is very important. These studies need to be performed in future for the realization of Si-NPs based printable optoelectronic devices.

7 References

1. C. N. Rao; G. U. Kulkarni; P. J. Thomas; P. P. Edwards, Size-dependent chemistry: Properties of nanocrystals. Chem. Eur. J. **2002,** 8, 28.
2. M. Hirasawa; T. Orii; T. Seto, Size-dependent crystallization of Si nanoparticles. Appl. Phys. Lett. **2006,** 88, 093119.
3. R. Waser, Nanoelectronics and information technology. Wiley VCH **2003**.
4. Nanoscience and nanotechnologies: Opportunities and uncertainties. The Royal Society & The Royal Academy of Engineering, Nanoscience and Nanotechnologies **July 2004**.
5. Higher-capacity lithium-ion batteries. Technology Review **June 22, 2006**.
6. Discovery and applications of photocatalysis — Creating a comfortable future by making use of light energy. Japan Nanonet Bulletin **May 12, 2005**.
7. Nanotechnology: Enabling technologies for Australian innovative industries. Paper prepared by an independent working group for the Prime Minister's Science, Engineering and Innovation Council (PMSEIC), Australian Government. **11 March, 2005**.
8. ScienceDaily, New nanotechnology products hitting the market at the rate of 3-4 per week. **April 25, 2008**.
9. M. Jaroniec, Silicon beyond the valley. Nat. Chem. **2009,** 1, 166.
10. S. Niesar; R. Dietmueller; H. Nesswetter; H. Wiggers; M. Stutzmann, Silicon/organic semiconductor heterojunctions for solar cells. Phys. Status Solidi A **2009,** 206, 2775.
11. C.-Y. Liu; Z. C. Holman; U. R. Kortshagen, Hybrid solar cells from P3HT and silicon nanocrystals. Nano Lett. **2009,** 9, 449.
12. L. Canham, Gaining light from silicon. Nature **2000,** 408, 411.
13. N. M. Park; T. S.Kim; S. J. Park, Band gap engineering of amorphous silicon quantum dots for light-emitting diodes. Appl. Phys. Lett. **2001,** 78, 2575.
14. F. Erogbogbo; K. T. Yong; I. Roy; G. Xu; P. N. Prasad; M. T. Swihart, Biocompatible luminescent silicon quantum dots for imaging of cancer cells. ACS Nano **2008,** 2, 873.
15. T. S.-Iwayama; S. Nakao; K. Saitoh, Visible photoluminescence in Si+ implanted thermal oxide films on crystalline Si. Appl. Phys. Lett. **1994,** 65, 1814.

16. T. S.-Iwayama; K. Fujita; S. Nakao; K. Saitoh; T. Fujita; N. Itoh, Visible photoluminescence in Si+ implanted silica glass. J. Appl. Phys. **1994,** 75, 7779.

17. T. S.-Iwayama; S. Nakao; K. Saitoh; N. Itoh, Photoluminescence from nanoparticles of silicon embedded in an amorphous silicon dioxide matrix. J. Phys. Condens. Matter **1994,** 6, L601.

18. J. Zou; R. K. Baldwin; K. A. Pettigrew; S. M. Kauzlarich, Solution synthesis of ultrastable luminescent siloxane-coated silicon nanoparticles. Nano Lett. **2004,** 4, 1181.

19. J. P. Wilcoxon; G. A. Samara, Tailorable, visible light emission from silicon nanocrystals. Appl. Phys. Lett. **1999,** 74, 3164.

20. J. P. Wilcoxon; G. A. Saara; P. N. Provencio, Optical and electronic properties of Si nanoclusters synthesized in inverse micelles. Phys. Rev. B **1999,** 60, 2704.

21. J. R. Heath, A liquid-solution-phase synthesis of crystalline silicon. Science **1992,** 258, 1131.

22. R. A. Bley; S. M. Kauzlarich, A low-temperature solution phase route for the synthesis of silicon nanoclusters. J. Am. Chem. Soc. **1996,** 118, 12461.

23. R. D. Tilley ; J. H. Warner; K. Yamamoto; I. Matsui; H. Fujimori, Micro-emulsion synthesis of monodisperse surface stabilized silicon nanocrystals. Chem. Commun. **2005,** 1833.

24. J. H. Warner; A. Hoshino; K. Yamamoto; R. D. Tilley, Water-soluble photoluminescent silicon quantum dots. Angew. Chem. Int. Ed. **2005,** 117, 4626.

25. X. Li; Y. He; S. S. Talukdar; M. T. Swihart, Process for preparing macroscopic quantities of brightly photoluminescent silicon nanoparticles with emission spanning the visible spectrum. Langmuir **2003,** 19, 8490.

26. L. Mangolini, Non-thermal plasma synthesis and passivation of luminescent silicon nanocrystals. University of Minnesota **2007**.

27. B. Gelloz; A. Kojima; N. Koshida, Highly efficient and stable luminescence of nanocrystalline porous silicon treated by high-pressure water vapor annealing. Appl. Phys. Lett. **2005,** 87, 031107.

28. X. D. Pi; L. Mangolini; S. A. Campbell; U. Kortshagen, Room-temperature atmospheric oxidation of Si nanocrystals after HF etching. Phy. Rev. B **2007,** 75, 085423.

29. C. Garcia; B. Garrido; P. Pellegrino; R. Ferre; J. A. Moreno; J. R. Morante; L. Pavesi; M. Cazzanelli, Size dependence of lifetime and absorption cross section of Si nanocrystals embedded in SiO_2. Appl. Phys. Lett. **2003,** 82, 1595.

30. D. I. Kovalev; I. D. Yaroshetzkii; T. Muschik; V. P. Koch; F. Koch, Fast and slow visible luminescence bands of oxidized porous Si. Appl. Phys. Lett. **1994,** 64, 214.

31. Z. Kang; Y. Liu; C. H. A. Tsang; D. D. D. Ma; X. Fan; N. Wong; S. Lee, Water-soluble silicon quantum dots with wavelength-tunable photoluminescence. Adv. Fun. Mater. **2009,** 21, 661.

32. M. V. Wolkin; J. Jorne; P. M. Fauchet; G. Allan; C. Delerue, Electronic states and luminescence in porous silicon quantum dots: The role of oxygen. Phys. Rev. Lett. **1999,** 82, 197.

33. H. Mizuno; H. Koyama; N. Koshida, Oxide-free blue photoluminescence from photochemically etched porous silicon. Appl. Phys. Lett. **1996,** 69, 3779.

34. Q. Chen; X. J. Li; Y. B. Jia; J. S. Zhu; Z. Yuheng, The role of SiO_2 in the blue luminescence in hydrothermally prepared porous silicon. J. Phys.: Condens. Matter **1997,** 9, L151.

35. M. Zhu; G. Chen; P. Chen, Green/blue light emission and chemical feature of nanocrystalline silicon embedded in silicon-oxide thin film. Appl. Phys. A **1997,** 65, 195.

36. Y. S. Kim; K. Y. Suh; H. Yoon; H. H. Lee, Stable blue photoluminescence from porous silicon. J. Electrochem. Soc. **2002,** 149, C50.

37. X. Li; Y. He; M. T. Swihart, Surface functionalization of silicon nanoparticles produced by laser-driven pyrolysis of silane followed by HF-HNO_3 etching. Langmuir **2004,** 20, 4720.

38. A. R. Stegner; R. N. Pereira; K. Klein; R. Lechner; R. Dietmueller; M. S. Brandt; M. Stutzmann; H. Wiggers, Electronic transport in phosphorus-doped silicon nanocrystal networks. Phys. Rev. Lett. **2008,** 100, 026803.

39. L. Gilles; G. Jiong; H. Friedrich, Effect of passivation and aging on the photoluminescence of silicon nanocrystals. Appl. Phys. Lett. **2001,** 79, 4028.

40. J. Nelles; D. Sendor; F.-M. Petrat; U. Simon, Electrical properties of surface functionalized silicon nanoparticles. J. Nanopart. Res. **2010,** 12, 1367.

41. M. A. Brook, Silicon in organic, organometallic, and polymer chemistry. Wiley: New York **2000**.

42. S. Patai; Z. Rappoport, The chemistry of organic silicon compound. John Wiley and Sons: New York **1989**.

43. M. R. Linford; P. Fenter; P. M. Eisenberger; C. E. D. Chidsey, Alkyl monolayers on silicon prepared from 1-alkenes and hydrogen-terminated silicon. J. Am. Chem. Soc. **1995,** 117, 3145.

44. B. Fabre; G. P. Lopinski; D. D. M. Wayner, Functionalization of Si(111) surfaces with alkyl chains terminated by electrochemically polymerizable thienyl units. Chem. Commun. **2002**, 2904.

45. J. M. Buriak; M. P. Stewart; T. W. Geders; M. J. Allen; H. C. Choi; J. Smith; D. Raftery; L. T. Canham, Lewis acid mediated hydrosilylation on porous silicon surfaces. J. Am. Chem. Soc. **1999,** 121, 11491.

46. R. Boukherroub; S. Morin; D. D. M. Wayner; D. J. Lockwood, Thermal route for chemical modification and photoluminescence stabilization of porous silicon. Phys. Status Solidi A **2000,** 182, 117.

47. R. Boukherroub; S. Morin; P. Sharpe; D. D. M. Wayner, Insights into the formation mechanisms of Si−OR monolayers from the thermal reactions of alcohols and aldehydes with Si(111)−H. Langmuir **2000,** 16, 7429.

48. R. Boukherroub; D. D. M. Wayner, Controlled functionalization and multistep chemical manipulation of covalently modified Si(111) surfaces. J. Am. Chem. Soc. **1999,** 121, 11513.

49. J. M. Schmeltzer; L. A. Porter; M. P. Stewart; J. M. Buriak, Hydride abstraction initiated hydrosilylation of terminal alkenes and alkynes on porous silicon. Langmuir **2002,** 18, 2971.

50. M. P. Stewart; J. M. Buriak, Exciton-mediated hydrosilylation on photoluminescent nanocrystalline silicon. J. Am. Chem. Soc. **2001,** 123, 7821.

51. J. M. Buriak; M. J. Allen, Lewis acid mediated functionalization of porous silicon with substituted alkenes and alkynes. J. Am. Chem. Soc. **1998,** 120, 1339.

52. J. Nelles; D. Sendor; A. Ebbers; F. Petrat; H. Wiggers; C. Schulz; U. Simon, Functionalization of silicon nanoparticles via hydrosilylation with 1-alkenes. Colloid. Polym. Sci. **2007,** 285, 729.

53. F. A. Reboredo; G. Galli, Theory of alkyl-terminated silicon quantum dots. J. Phys. Chem. B **2005,** 109, 1072.

54. H. H. Lee; K. S. Chou; K. C. Huang, Inkjet printing of nanosized silver colloids. Nanotech. **2005,** 16, 2436.

55. C. Ingrosso; J. Y. Kim; E. Binetti; V. Fakhfouri; M. Striccoli; A. Agostiano; M. L. Curri; J. Brugger, Drop-on-demand inkjet printing of highly luminescent CdS and CdSe@ZnS nanocrystal based nanocomposites. Microelectron. Eng. **2009,** 86, 1124.

56. W. Cui; W. Lu; Y. Zhang; G. Lin; T. Wei; L. Jiang, Gold nanoparticle ink suitable for electric-conductive pattern fabrication using in ink-jet printing technology. Colloids Surf. A **2007,** 358, 35.

57. I.-K. Shim; Lee, Y.; K. J.Lee; J. Joung, An organometallic route to highly monodispersed silver nanoparticles and their application to ink-jet printing. Mater. Chem. Phys. **2008,** 110, 316.

58. H.-W. Lin; W.-H. Hwu; M.-D. Ger, The dispersion of silver nanoparticles with physical dispersal procedures. J. Mater. Process. Technol. **2008,** 206, 56.

59. H.-H. Lee; Chou, K.-S.; Huang, K.-C., Inkjet printing of nanosized silver colloids. Nanotech. **2005,** 16, 2436.

60. M. Harting; J. Zhang; D. R. Gamota; D. T. Britton, Fully printed silicon field effect transistors. Appl. Phys. Lett. **2009,** 94, 193509.

61. U. Simon; R. Flesch; H. Wiggers; G. Schön; G. Schmid, Chemical tailoring of the charging energy in metal cluster arrangements by use of bifunctional spacer molecules J. Mater. Chem. **1998,** 8, 517.

62. M. Brust; D. Bethell; D. J. Schiffrin; C. J. Kiely, Novel gold-dithiol nano-networks with non-metallic electronic properties. Adv. Mater. **1995,** 7, 795.

63. J. J. Storhoff; A. A. Lazarides; R. C. Mucic; C. A. Mirkin; R. L. Letsinger; G. C. Schatz, What controls the optical properties of DNA-linked gold nanoparticle assemblies? J. Am. Chem. Soc. **2000,** 122, 4640.

64. H. Bönnemann; N. Waldofner; H. G. Haubold; T. Vad, Preparation and characterization of three-dimensional Pt nanoparticle networks. Chem. Mater. **2002,** 14, 1115.

65. L. Pavesi; D. J. Lockwood, Silicon photonic. Springer **2004**.

66. L. T. Canham, Silicon quantum wire array fabrication by electrochemical and chemical dissolution of wafers. Appl. Phys. Lett. **1990,** 57, 1046.

67. L. T. Canham, Luminescence bands and their proposed origins in highly porous silicon. Phys. Status Solidi B **1995,** 190, 9.

68. L. T. Canham; M. R. Houlton; W. Y. Leong; C. Pickering; J. M. Keen, Atmospheric impregnation of porous silicon at room temperature. J. Appl. Phys. **1991,** 70, 422.

69. A. G. Cullis; L. T. Canhan, Visible light emission due to quantum size effects in highly porous crystalline silicon. Nature **1991,** 353, 335.

70. V. Lehmann; U. Gösele, Porous silicon formation: A quantum wire effect. Appl. Phys. Lett. **1991,** 58, 856.

71. S. Veprek, Electronic and mechanical properties of nanocrystalline composites when approaching molecular size. Thin Solid Films **1997,** 297, 145.

72. Z.Kang; Y. Liu; C. H. A. Tsang; D. D. D. Ma; X. Fan; N. Wong; S. Lee, Water-soluble silicon quantum dots with wavelength-tunable photoluminescence. Adv. Fun. Mater. **2009,** 21, 661.

73. M. Dovrat; N. Arad; X. H. Zhang; S. T. Lee; A. Sa'ar, Cathodoluminescence and photoluminescence of individual silicon nanowires. Phys. Status Solidi A **2007,** 204, 1512.

74. J. S. Biteen; D. Pacifici; N. S. Lewis; H. A. Atwater, Enhanced radiative emission rate and quantum efficiency in coupled silicon nanocrystal-nanostructured gold emitters. Nano Lett. **2005,** 5, 1768.

75. R. J. Walters; J. Kalkman; A. Polman; H. A. Atwater; M. J. A. de Dood, Photoluminescence quantum efficiency of dense silicon nanocrystal ensembles in SiO_2. Phys. Rev. B **2006,** 73, 132302.

76. L. Gilles; G. Jiong; H. Friedrich, Effect of passivation and aging on the photoluminescence of silicon nanocrystals. Appl. Phys. Lett. **2001,** 79, 4028.

77. A. R. Stegner; R. N. Pereira; R. Lechner; K. Klein; H. Wiggers; M. Stutzmann; M. S. Brandt, Doping efficiency in freestanding silicon nanocrystals from the gas phase: Phosphorus incorporation and defect-induced compensation. Phys. Rev. B **2009,** 80, 165326.

78. F. Hua; M. T. Swihart; E. Ruckenstein, Efficient surface grafting of luminescent silicon quantum dots by photoinitiated hydrosilylation. Langmuir **2005,** 21, 6054.

79. J. Nelles; D. Sendor; M. Bertmer; A. Ebbers; F. M. Petrat; U. Simon, Surface chemistry of n-octane modified silicon nanoparticles analysed by IR, ^{13}C CPMAS NMR and EELS. J. Nanosci. Nanotechnol. **2007,** 7, 2818.

80. R. Lechner; A. R. Stegner; R. N. Pereira; R. Dietmueller; M. S. Brandt; A. Ebbers; M. Trocha; H. Wiggers; M. Stutzmann, Electronic properties of doped silicon nanocrystal films. J. Appl. Phys. **2008,** 104, 053701.

81. H. Sirringhaus; T. Kawase; R. H. Friend; T. Shimoda; M. Inbasekaran; W. Wu; E. P. Woo, High-resolution inkjet printing of all-polymer transistor circuits. Science **2000,** 290, 2123.

82. C. N. Hoth; S. A. Choulis; P. Schilinsky; C. J. Brabec, High photovoltaic performance of inkjet printed polymer: Fullerene blends. Adv. Mater. **2007,** 19, 3973.

83. V. Wood; M. J. Panzer; J. Chen; M. S. Bradley; J. E. Halpert; M. G. Bawendi; V. Bulović, Inkjet-printed quantum dot–polymer composites for full-color AC-driven displays. Adv. Mater. **2009,** 21, 2151.

84. L. Mangolini; U. Kortshagen, Plasma-assisted synthesis of silicon nanocrystal inks. Adv. Mater. **2007,** 19, 2513.

85. M. T. Swihart, Silicon nanoparticles: Vapor-phase synthesis of nanoparticles. Curr. Opin. Colloid Interface Sci. **2003,** 8, 127.

86. B. Schwade; P. Roth, Simulation of nano-particle formation in a wall-heated aerosol reactor including coalescence. J. Aerosol Sci. **2003,** 34, 339.

87. B. Giesen; H. Wiggers; A. Kowalik; P. Roth, Formation of Si-nanoparticles in a microwave reactor: Comparison between experiments and modelling J. Nanopart. Res. **2005,** 7, 29.

88. D. Woiki; A. Kunz; P. Roth, Chemical reactions of aerosol precursors. J. Aerosol Sci. Suppl. **2000,** 1, 212.

89. J. E. McDonald, Homogeneous nucleation of vapor condensation. II. Kinetic aspects. Am. J. Phys. **1963,** 31, 31.

90. W. C. Hinds, Aerosol technology: Properties, behavior, and measurement of airborne particles. Wiley-Interscience **1999**.

91. M. Winterer, Nanocrystalline ceramics - Synthesis and structure. Springer **2002**.

92. S. Tsantilis; S. E. Pratsinis, Soft- and hard-agglomerate aerosols made at high temperatures. Langmuir **2004,** 20, 5933.

93. IUPAC, Stability constants of metal ion complexes: Part A. Pergamon Press: Oxford **1982**.

94. L. J. Warren, The measurement of pH in acid fluoride solutions and evidence for the existence of $(HF)_2$. Anal. Chim. Acta **1971,** 53, 199.

95. D. M. Knotter, Etching mechanism of vitreous silicon dioxide in HF-based solutions. J. Am. Chem. Soc. **2000,** 122, 4345.

96. G. W. Trucks; K. Raghavachari; G. S. Higashi; Y. J. Chabal, Mechanism of HF etching of silicon surfaces: A theoretical understanding of hydrogen passivation. Phys. Rev. Lett. **1990,** 65, 504.

97. E. Sacher; A. Yelon, Comment on ``Mechanism of HF etching of silicon surfaces: A theoretical understanding of hydrogen passivation". Phys. Rev. Lett. **1991,** 66, 1647.

98. J. Fritz; E. B. Cooper; S. Gaudet; P. K. Sorger; S. R. Manalis, Electronic detection of DNA by its intrinsic molecular charge. Proc. Natl. Acad. Sci. **2002,** 99, 14142.

99. A. B. Sieval; A. L. Demirel; J. W. M. Nissink; M. R. Linford; J. H. van der Maas; W. H. de Jeu; H. Zuilhof; E. J. R. Sudhölter, Highly stable Si-C linked functionalized monolayers on the silicon (100) surface. Langmuir **1998,** 14, 1759.

100. T. Strother; W. Cai; X. Zhao; R. J. Hamers; L. M. Smith, Synthesis and characterization of DNA-modified silicon (111) surfaces. J. Am. Chem. Soc. **2000,** 122, 1205.

101. T. He; J. He; M. Lu; B. Chen; H. Pang; W. F. Reus; W. M. Nolte; D. P. Nackashi; P. D. Franzon; J. M. Tour, Controlled modulation of conductance in silicon devices by molecular monolayers. J. Am. Chem. Soc. **2006,** 128, 14537.

102. R. C. Anderson; R. S. Muller; C. W. Tobias, Chemical surface modification of porous silicon. J. Electrochem. Soc. **1993,** 140, 1393.

103. V. M. Dubin; C. Vieillard; F. Ozanam; J. N. Chazalviel, Preparation and characterization of surface-modified luminescent porous silicon. Phys. Status Solidi B **1995,** 190, 47.

104. J. M. Buriak, Organometallic chemistry on silicon and germanium surfaces. Chem. Rev. **2002,** 102, 1271.

105. L. C. P. M. de Smeta; A. V. Pukina; Q.-Y. Suna; B. J. Evesb; G. P. Lopinskib; G. M. Vissera; H. Zuilhofa; E. J. R. Sudhöltera, Visible-light attachment of Si-C linked functionalized organic monolayers on silicon surfaces. Appl. Surf. Sci. **2005,** 252, 24.

106. L. C. P. M. de Smet; H. Zuilhof; E. J. R. Sudhölter; L. H. Lie; A. Houlton; B. R. Horrocks, Mechanism of the hydrosilylation reaction of alkenes at porous silicon: Experimental and computational deuterium labeling studies. J. Phys. Chem. B **2005,** 109, 12020.

107. N. Y. Kim; P. E. Laibinis, Derivatization of porous silicon by grignard reagents at room temperature. J. Am. Chem. Soc. **1998,** 120, 4516.

108. S. B. Fuller, A fast flexible ink-jet printing method for patterning networks of neurons in culture. Massachusetts Institute of Technology **2000**.

109. L. Lutterotti; S. Matthies; H. R. Wenk, MAUD: A friendly Java program for material analysis using diffraction. ICUr: Newsletter of the CPD **1999,** 21, 14. Program available at http://www.ing.unitn.it/~maud/.

110. U. Kaiser, Characterisation of thin SiC films and low-dimensional structures in SiC using advanced transmission electron microscopy. Friedrich Schiller University of Jena **2002**.

111. E. Barsoukov; J. R. Macdonald, Impedance spectroscopy: theory, experiment, and applications. Wiley-InterScience **2005**.

112. H. Günzler; H.-U. Gremlich, IR spectroscopy: An introduction. Wiley-VCH **2002**.

113. M. Brustolon; E. Giamello, Electron paramagnetic resonance: A practitioners toolkit. Wiley InterScience **2009**.

114. C. Meier; A. Gondorf; S. Luttjohann; A. Lorke; H. Wiggers, Silicon nanoparticles: Absorption, emission, and the nature of the electronic bandgap. J. Appl. Phys. **2007,** 101, 103112.

115. M. S. Hybertsen, Absorption and emission of light in nanoscale silicon structures. Phys. Rev. Lett. **1994,** 72, 1514.

116. G. Allan; C. Delerue; M. Lannoo, Nature of luminescent surface states of semiconductor nanocrystallites. Phys. Rev. Lett. **1996,** 76, 2961.

117. J. Valenta; R. Juhasz; J. Linnros, Photoluminescence spectroscopy of single silicon quantum dots. Appl. Phys. Lett. **2002,** 80, 1070.

118. K. Kimura, Blue luminescence from silicon nanoparticles suspended in organic liquids. J. Cluster Sci. **1999,** 10, 359.

119. C. Delerue; G. Allan; M. Lannoo, Theoretical aspects of the luminescence of porous silicon. Phys. Rev. B **1993,** 48, 11024.

120. G. Ledoux; O. Guillois; D. Porterat; C. Reynaud; F. Huisken; B. Kohn; V. Paillard, Photoluminescence properties of silicon nanocrystals as a function of their size. Phys. Rev. B **2000,** 62, 15942.

121. L. Mangolini; D. Jurbergs; E. Rogojina; U. Kortshagen, Plasma synthesis and liquid-phase surface passivation of brightly luminescent Si nanocrystals. J. Lumin. **2006,** 121, 327.

122. J. Knipping; H. Wiggers; B. Rellinghaus; P. Roth; D. Konjhodzic; C. Meier, Synthesis of high purity silicon nanoparticles in a low pressure microwave reactor. J. Nanosci. Nanotechnol. **2004,** 4, 1039.

123. A. Weibel; R. Bouchet; F. Boulc'h; P. Knauth, The big problem of small particles: A comparison of methods for determination of particle size in nanocrystalline anatase powders. Chem. Mater. **2005,** 17, 2378.

124. G. Lucovsky; R. J. Nemanich; J. C. Knights, Structural interpretation of the vibrational spectra of a-Si: H alloys. Phy. Rev. B **1979,** 19, 2064.

125. G. J. Kluth; M. Roya, Oxidation mechanism of the ammonium-fluoride-treated Si(100) surface. J. Appl. Phys. **1996,** 80, 5408.

126. G. Lucovsky; J. Yang; S. S. Chao; J. E. Tyler; W. Czubatyj, Oxygen-bonding environments in glow-discharge-deposited amorphous silicon-hydrogen alloy films. Phy. Rev. B **1983,** 28, 3225.

127. P. G. Pai; S. S. Chao; Y. Takagi; G. Lucovsky, Infrared spectroscopic study of SiO_x films produced by plasma enhanced chemical vapor deposition. J. Vac. Sci. Technol. A **1986,** 4, 689.

128. M. Niwano; J.-I. Kageyama; K. Kurita; K. Kinashi; I. Takahashi; N. Miyamoto, Infrared spectroscopy study of initial stages of oxidation of hydrogen-terminated Si surfaces stored in air. J. Appl. Phys. **1994,** 76, 2157.

129. D. V. Tsu; G. Lucovsky; B. N. Davidson, Effects of the nearest neighbors and the alloy matrix on SiH stretching vibrations in the amorphous SiO_r:H ($0<r<2$) alloy system. Phys. Rev. B **1989,** 40, 1795.

130. D. C. Marra; E. A. Edelberg; R. L. Naone; E. S. Aydil, Silicon hydride composition of plasma-deposited hydrogenated amorphous and nanocrystalline silicon films and surfaces. J. Vac. Sci. Technol. A **1998,** 16, 3199.

131. D. Gräf; M. Grundner; R. Schulz; L. Mühlhoff, Oxidation of HF-treated Si wafer surfaces in air. J. Appl. Phys. **1990,** 68, 5155.

132. M. R. Houston; R. Maboudian, Stability of ammonium fluoride-treated Si(100). J. Appl. Phys. **1995,** 78, 3801.

133. W. Simons, The sadtler handbook of infrared spectra. Heyden & Son, Philadelphia **1978**.

134. K. E. Bean, Anisotropic etching of silicon. IEEE Trans. Electron. Devices **1978,** 25, 1185.

135. S. Godefroo; M. Hayne; M. Jivanescu; A. Stesmans; M. Zacharias; O. I. Lebedev; G. Van Tendeloo; V. V. Moshchalkov, Classification and control of the origin of photoluminescence from Si nanocrystals. Nat. Nano **2008,** 3, 174.

136. S. M. Prokes; O. J. Glembocki, Role of interfacial oxide-related defects in the red-light emission in porous silicon. Phy. Rev. B **1994,** 49, 2238.

137. B. G. Fernandez; M. Lopez; C. Garcia; A. P. Rodriguez; J. R. Morante; C. Bonafos; M. Carrada; A. Claverie, Influence of average size and interface passivation on the spectral emission of Si nanocrystals embedded in SiO_2. J. Appl. Phys. **2002,** 91, 798.

138. E. Poindexter; P. Caplan; B. Deal; R. Razouk, Interface states and electron spin resonance centers in thermally oxidized (111) and (100) silicon wafers. J. Appl. Phys. **1981,** 52, 879.

139. A. Stesmans; V. V. Afanas'ev, Electron spin resonance features of interface defects in thermal (100)Si/SiO_2. J. Appl. Phys. **1998,** 83, 2449.

140. M. Stutzmann; D. K. Biegelsen, Microscopic nature of coordination defects in amorphous silicon. Phys. Rev. B **1989,** 40, 9834.

141. E. San Andrés; A. del Prado; I. Mártil; G. González; F. L. Martínez; D. Bravo; F. J. López; M. Fernández, Physical properties of plasma deposited SiO_x thin films. Vacuum **2002,** 67, 525.

142. M. A. Green, Crystalline silicon photovoltaic cells. Adv. Mater. **2001,** 13, 1019.

143. L. Guo; E. Leobandung; S. Y. Chou, A silicon single-electron transistor memory operating at room temperature. Science **1997,** 275, 649.

144. S. Coe; W. K. Woo; M. Bawendi; V. Bulovic, Electroluminescence from single monolayers of nanocrystals in molecular organic devices. Nature **2002,** 420, 800.

145. S. M. Prokes; W. E. Carlos; V. M. Bermudez, Luminescence cycling and defect density measurements in porous silicon: Evidence for hydride based model. Appl. Phys. Lett. **1992,** 61, 1447.

146. R. Tohmon; Y. Shimogaichi; H. Mizuno; Y. Ohki; K. Nagasawa; Y. Hama, 2.7-eV luminescence in as-manufactured high-purity silica glass. Phys. Rev. Lett. **1989,** 62, 1388.

147. S. Munekuni; T. Yamanaka; Y. Shimogaichi; R. Tohmon; Y. Ohki; K. Nagasawa; Y. Hama, Various types of nonbridging oxygen hole center in high-purity silica glass. J. Appl. Phys. **1990,** 68, 1212.

148. L. Skuja, Isoelectronic series of twofold coordinated Si, Ge, and Sn atoms in glassy SiO_2: A luminescence study. J. Non-Cryst. Solids **1992,** 149, 77.

149. S. Kluge, Funktionalisierung von silizium-nanopartikeln für lumineszierende silizium-quantendots. University of Duisburg-Essen **2009**.

150. H. Ibach; H. D. Bruchmann; H. Wagner, Vibrational study of the initial stages of the oxidation of Si(111) and Si(100) surfaces. Appl. Phys. A **1982,** 29, 113.

151. M. P. Stewart; E. G. Robins; T. W. Geders; M. J. Allen; H. C. Choi; J. M. Buriak, Three methods for stabilization and functionalization of porous silicon surfaces via hydrosilylation and electrografting reactions. Phys. Status Solidi A **2000,** 182, 109.

152. G. F. Santee; R. H. Marchessault; H. G. Clark; J. J. Kearny; V. Stannett, The polymerization of vinyl benzoate. Die Makromolekulare Chemie **1964,** 73, 177.

153. M. Litt; V. Stannett, Remarks on the polymerization of vinyl benzoate. Die Makromolekulare Chemie **1960,** 37, 19.

154. W. L. Wilson; P. F. Szajowski; L. E. Brus, Quantum confinement in size-selected, surface-oxidized silicon nanocrystals. Science **1993,** 262, 1242.

155. L. Brus, Luminescence of silicon materials: Chains, sheets, nanocrystals, nanowires, microcrystals, and porous silicon. J. Phys. Chem. **1994,** 98, 3575.

156. R. M. Sankaran; D. Holunga; R. C. Flagan; K. P. Giapis, Synthesis of blue luminescent Si nanoparticles using atmospheric-pressure microdischarges. Nano Lett. **2005,** 5, 537.

157. L. Mangolini; D. Jurbergs; E. Rogojina; U. Kortshagen, High efficiency photoluminescence from silicon nanocrystals prepared by plasma synthesis and organic surface passivation. Phys. Status Solidi C **2006,** 3, 3975.

158. R. Wang; J. Peng; F. Qiu; Y. Yang; Z. Xie, Simultaneous blue, green, and red emission from diblock copolymer micellar films: a new approach to white-light emission. **Chem. Commun. 2009**, 6723.

159. G. M. Credo; M. D. Mason; S. K. Buratto, External quantum efficiency of single porous silicon nanoparticles. Appl. Phys. Lett. **1999,** 74, 1978.

160. I. Plümel, Thesis (to be published). University of Duisburg-Essen.

161. L.-Y. Chen; W.-H. Chen; J.-J. Wang; F. C.-N. Hong; Y.-K. Su, Hydrogen-doped high conductivity ZnO films deposited by radio-frequency magnetron sputtering. Appl. Phys. Lett. **2004,** 85, 5628.

162. S. Hartner; M. Ali; C. Schulz; M. Winterer; H. Wiggers, Electrical properties of aluminum-doped zinc oxide (AZO) nanoparticles synthesized by chemical vapor synthesis. Nanotech. **2009,** 20, 445701.

163. K. Shigemi; N. Mikihiko; W. Takahiro; H. Takashi, Enhanced conductivity of zinc oxide thin films by ion implantation of hydrogen atoms. Appl. Phys. Lett. **1994,** 64, 2876.

164. S. Sato; M. T. Swihart, Propionic-acid-terminated silicon nanoparticles: Synthesis and optical characterization. Chem. Mater. **2006,** 18, 4083.

165. J. Park; J. Moon, Control of colloidal particle deposit patterns within picoliter droplets ejected by ink-jet printing. Langmuir **2006,** 22, 3506.

166. Link of the video can be found at http://www.uni-due.de/ivg/vg/forschung/fo_na.shtml.

167. K. D. Hirschman; L. Tsybeskov; S. P. Duttagupta; P. M. Fauchet, Silicon-based visible light-emitting devices integrated into microelectronic circuits. Nature **1996,** 384, 338.

168. L. Pavesi; L. D. Negro; C. Mazzoleni; G. Franzo; F. Priolo, Optical gain in silicon nanocrystals. Nature **2000,** 408, 440.

169. X. D. Pi; R. W. Liptak; J. D. Nowak; N. P. Wells; C. B. Carter; S. A. Campbell; U. Kortshagen, Air-stable full-visible-spectrum emission from silicon nanocrystals synthesized by an all-gas-phase plasma approach. Nanotechnol. **2008,** 19, 245603.

170. A. S. Blum; M. H. Moore; B. R. Ratna, Quantum dot fluorescence as a function of alkyl chain length in aqueous environments. Langmuir **2008** 24, 9194.

8 Appendix A

Table 8.1. Properties of bulk silicon.

Property	Value
Molar mass (g/mol)	28.0855
Density (g/cm^3) at 25°C	2.3290
Melting point (°C)	1414
Boiling point (°C)	3265
Band gap (eV)	1.17

Table 8.2. Properties of hex-1-ene

Property	Value	Chemical structure
Molecular formula	C_6H_{12}	
Molar mass	84.1608	
Density (g/cm^3) at 25°C	0.673	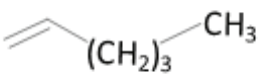
Melting point (°C)	-140	
Boiling point (°C)	63	

Table 8.3. Properties of dec-1-ene

Property	Value	Chemical structure
Molecular formula	$C_{10}H_{20}$	
Molar mass	140.27	
Density (g/cm^3) at 25°C	0.7408	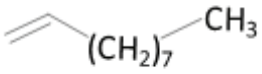
Melting point (°C)	-66	
Boiling point (°C)	181	

Table 8.4. Properties of dodec-1-ene

Property	Value	Chemical structure
Molecular formula	$C_{12}H_{24}$	
Molar mass	168.31	
Density (g/cm^3) at 25°C	0.759	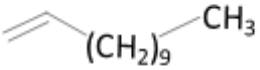
Melting point (°C)	-35	
Boiling point (°C)	213	

Table 8.5. Properties of tetradec-1-ene

Property	Value	Chemical structure
Molecular formula	$C_{14}H_{28}$	
Molar mass	196.37	
Density (g/cm^3) at 25°C	0.77	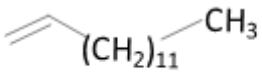
Melting point (°C)	-13	
Boiling point (°C)	251	

Table 8.6. Properties of octadec-1-ene

Property	Value	Chemical structure
Molecular formula	$C_{18}H_{36}$	
Molar mass	252.48	
Density (g/cm^3) at 25°C	0.789	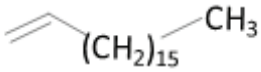
Melting point (°C)	17	
Boiling point (°C)	315	

Table 8.7. Properties of ethyl undecylenate

Property	Value	Chemical structure
Molecular formula	$C_{13}H_{24}O_2$	
Molar mass	212.33	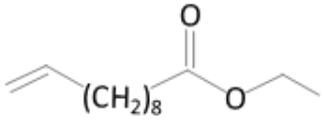
Density (g/cm^3) at 25°C	0.879	
Melting point (°C)	-38	
Boiling point (°C)	259	

Table 8.8. Properties of vinyl benzoate

Property	Value	Chemical structure
Molecular formula	$C_9H_8O_2$	
Molar mass	148.16	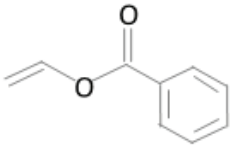
Density (g/cm^3) at 25°C	1.07	
Boiling point (°C)	96	

Table 8.9. Properties of ethyl-2-methyl-4-pentenoate

Property	Value	Chemical structure
Molecular formula	$C_8H_{14}O_2$	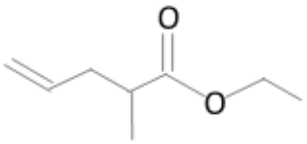
Molar mass	142.20	
Density (g/cm^3) at 25°C	0.873	
Boiling point (°C)	155	

Table 8.10. Properties of 1,7-octadiene

Property	Value	Chemical structure
Molecular formula	C_8H_{14}	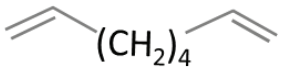
Molar mass	110.2	
Density (g/cm^3) at 25°C	0.746	
Melting point (°C)	-70	
Boiling point (°C)	121	

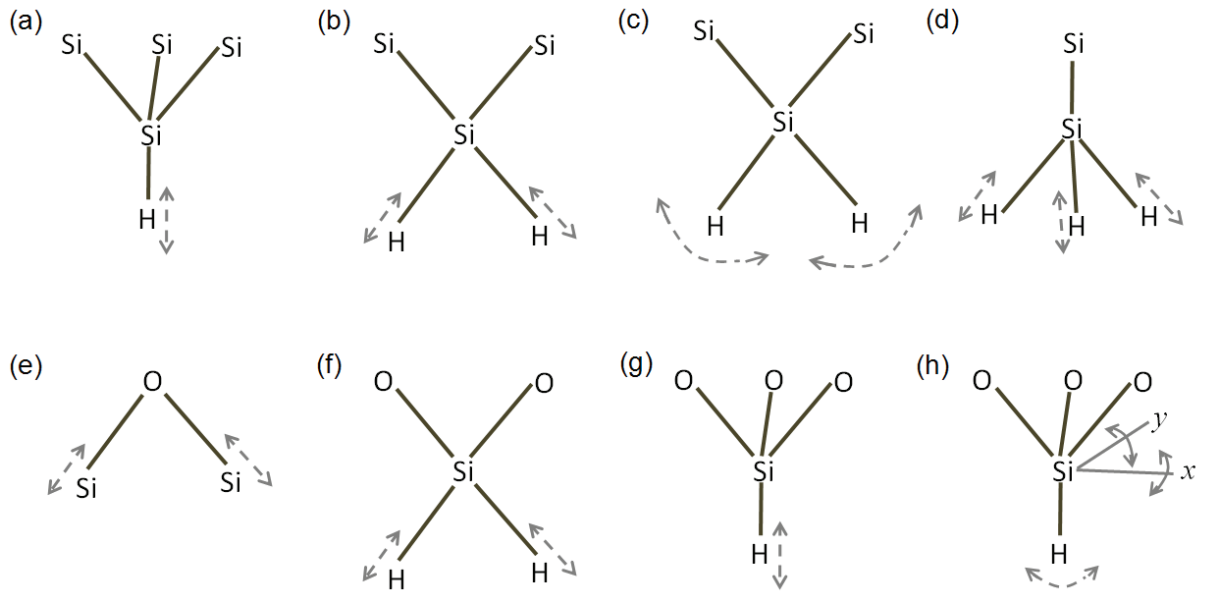

Fig. 8.1. Schematic representation of (a) SiH stretching, (b) SiH_2 stretching, (c) SiH_2 scissor, (d) SiH_3 stretching, (e) SiOSi stretching, (f) SiH_2O_2 stretching, (g) $SiHO_3$ stretching, and (h) $SiHO_3$ bending vibration modes. The arrow shows the vibration directions of atoms. In stretching and scissor vibration modes, there is a change in the bond length and bond angle, respectively. Whereas, bending mode is the rotation of the SiH group about either *x* or *y* axis.

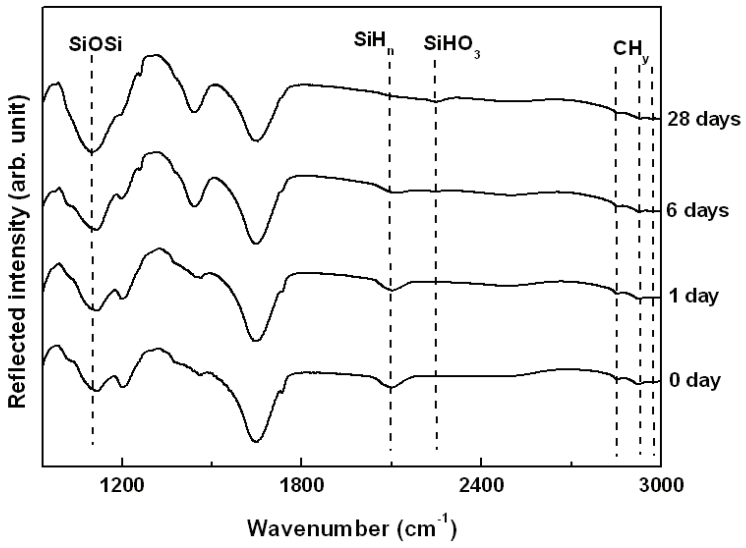

Fig. 8.2. Evolution of the FTIR spectra of ethyl undecylenate functionalized Si-NPs as a function of air exposure time.

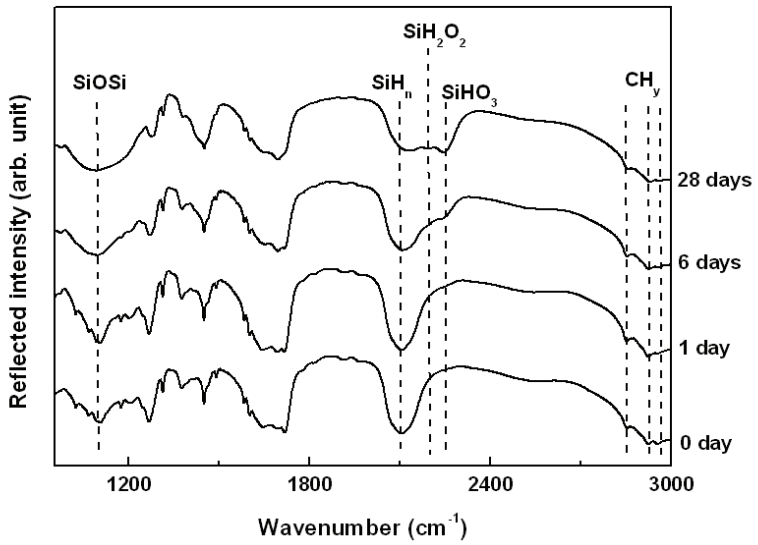

Fig. 8.3. Evolution of the FTIR spectra of vinyl benzoate functionalized Si-NPs as a function of air exposure time.

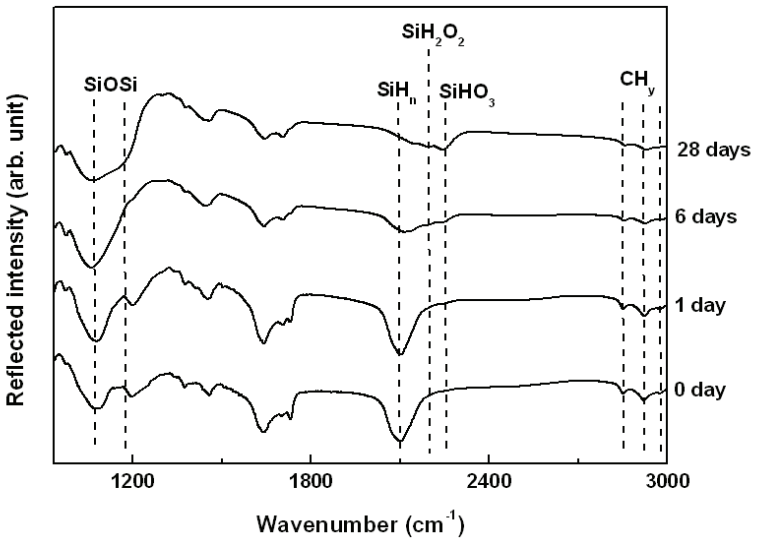

Fig. 8.4. Evolution of the FTIR spectra of ethyl-2-methyl-4-pentenoate functionalized Si-NPs as a function of air exposure time.

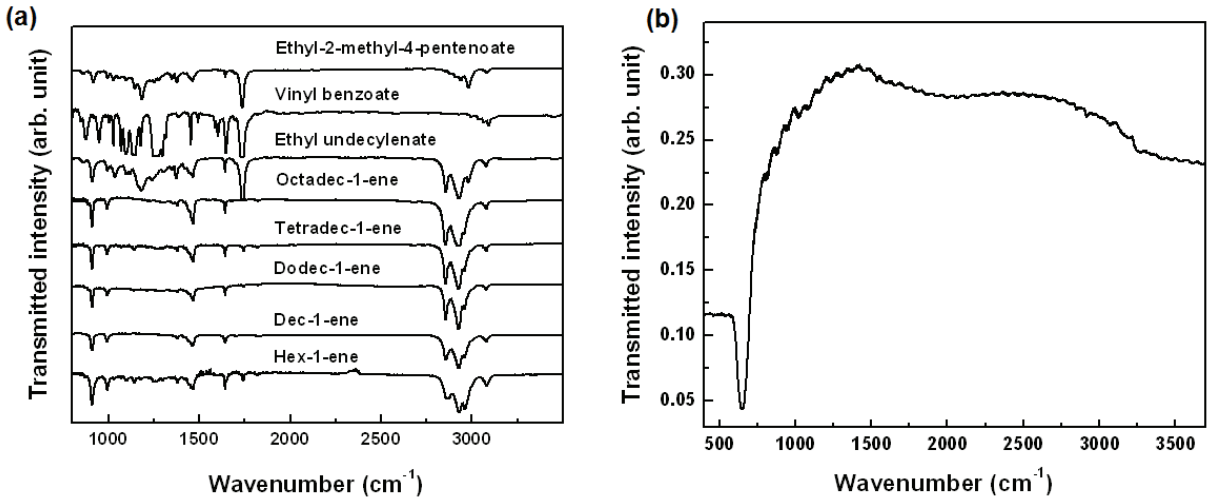

Fig. 8.5. FTIR spectra of (a) pure alkenes, and (b) zinc selenide (ZnSe). The FTIR of ZnSe shows high transmission of the infrared light in the measured range (900 cm^{-1}–3300 cm^{-1}). The spectra of all alkenes are measured in the transmission mode by spreading a thin layer of alkene between two ZnSe windows.

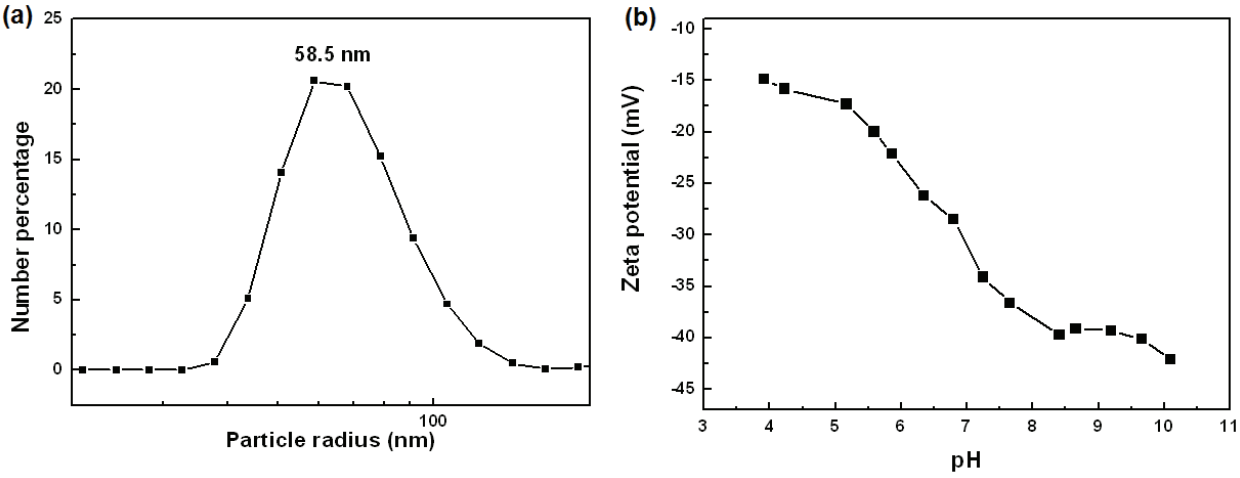

Fig. 8.6. (a) Particle size distribution, and (b) zeta potential of as-synthesized Si-NPs dispersion in de-ionized water. The particle size distribution was measured using dynamic light scattering. The measurements were performed using Malvern Zetasizer Nano-ZS instrument.

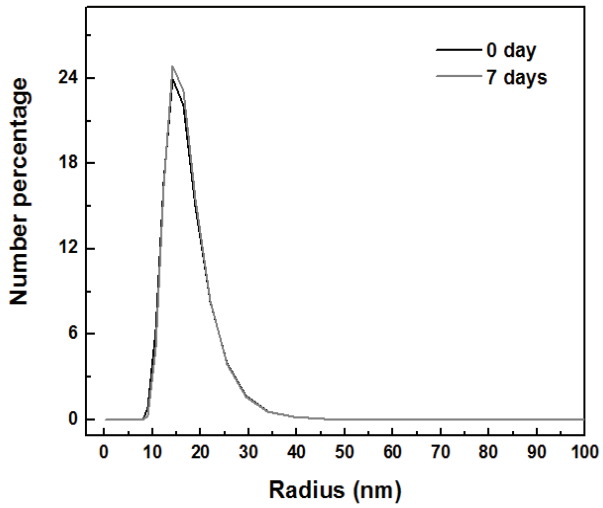

Fig. 8.7. Particle size distribution of ETU functionalized Si-NPs measured using dynamic light scattering.

List of own publications

Peer reviewed articles

1. **A. Gupta**, M. T. Swihart and H. Wiggers

   Luminescent colloidal dispersion of silicon quantum dots from microwave plasma synthesis: Exploring the photoluminescence behavior across the visible spectrum.

   Adv. Funct. Mater., 19 (2009), 696–703 (**featured on cover page of the journal**).

2. **A. Gupta** and H. Wiggers,

   Surface chemistry and photoluminescence property of functionalized silicon nano-particles.

   Physica E, 41 (2009), 1010 – 1014.

3. **A. Gupta**, F. Erogbogbo, M. T. Swihart and H. Wiggers

   Photoluminescence behavior of silicon nanocrystals: Role of surface chemistry and size.

   Mat. Res. Soc. Symp. Proc., 1145 (2009), MM10 – 04.

4. **A. Gupta**, A. Chuvilin, S. Mohanan, Z. Zhang, U. Kaiser and U. Herr

   Investigation of the Microstructure of Co/Cu/Co/NiMn Spin Valve Systems.

   Sci. Adv. Mater., 1 (2009), 198 – 204.

5. **A. Gupta**, S. Mohanan, M. Kinyanjui, A. Chuvilin, U. Kaiser and U. Herr

   Influence of nano-oxide layer on the magnetotransport properties of NiMn/Co/Cu/Co spin valve sensors.

   J. Appl. Phys., 107 (2010), 093910.

6. **A. Gupta** and H. Wiggers

   Influence of etching and surface functionalization on the optical property of luminescing phosphorus doped silicon nanoparticles.

   J. Optoelectron. Adv. Mater., 12 (2010), 518 – 522.

7. **A. Gupta**, S. Kluge, C. Schulz and H. Wiggers

   Enhanced long-term stability of functionalized silicon nanoparticles using esters.

   Mat. Res. Soc. Symp. Proc., 1207 (2010), N02 – 03.

8. A. Abdali, B. Moritz, **A. Gupta**, H. Wiggers and C. Schulz

   Hybrid microwave-plasma hot-wall reactor for synthesis of silica nanoparticles under well-controlled conditions.

   J. Optoelectron. Adv. Mater., 12 (2010), 440 – 444.

9. **A. Gupta** and H. Wiggers.

   Influence of reaction parameters on the photoluminescence properties of free standing functionalized silicon nanocrystals.

   Mat. Res. Soc. Symp. Proc., 1260 (2010), T06 – 05.

10. **A. Gupta** and H. Wiggers

    Freestanding silicon quantum dots: Origin of red and blue luminescence

    Nanotechnol., 22 (2011), 055707.

11. **A. Gupta**, P. Ifeacho, C. Schulz and H. Wiggers

    Synthesis of tailored WO_3 and WO_x ($2.9 < x < 3$) nanoparticles by adjusting the combustion conditions in a $H_2/O_2/Ar$ premixed flame reactor.

    Proc. Combust. Inst., 33 (2011) 1883 – 1890.

12. **A. Gupta**, A.S.G. Khalil, M. Offer, M. Geller, M. Winterer, A. Lorke and H. Wiggers

    Synthesis and ink-jet printing of highly luminescing silicon nanoparticles for printable electronics.

    J. Nanosci. Nanotechnol., 11 (2011) 5028–5033.

13. **A. Gupta**, S. Hartner and H. Wiggers

    Influence of surface chemistry on the electrical properties of silicon nanoparticles.

    Submitted.

Conference articles

1. **A. Gupta**, C. Schulz and H. Wiggers

   Optical properties of silicon nanoparticles: Influence of etching, surface oxidation and surface functionalization.

   Nanotech., 2 (2010), 53 – 56.

   ISBN: 978-1-4398-3402-2

2. **A. Gupta**, A. S. G. Khalil, M. Winterer and H. Wiggers

   Stable colloidal dispersion of luminescing silicon nanoparticles for ink-jet printing.

   Nanotech., 2 (2010), 538 – 541 .

   ISBN: 978-1-4398-3402-2

3. S. Hartner, **A. Gupta** and H. Wiggers

   Electrical properties of functionalized nanoparticles.

   Nanotech., 1 (2010), 376 – 378.

   ISBN: 978-1-4398-3401-5

4. H. Grimm, N. Petermann, **A. Gupta** and H. Wiggers

   Synthesis of highly-doped silicon and germanium nanoparticles in a low-pressure plasma-reactor for thermoelectric and solar applications.

   Nanotech., 1 (2010), 410 – 412.

   ISBN: 978-1-4398-3401-5

5. **A. Gupta**, S. Hartner and H. Wiggers

   Optical and electrical properties of silicon nanoparticles.

   3rd International Nanoelectronics Conference (INEC), 2010, pp. 616 – 617.

   DOI: 10.1109/INEC.2010.5424734

6. **A. Gupta**, A. S. G. Khalil, M. Winterer and H. Wiggers

   Stable colloidal dispersions of silicon nanoparticles for the fabrication of films using inkjet printing technolog.

   3rd International Nanoelectronics Conference (INEC), 2010, pp. 1018 – 1019.

   DOI: 10.1109/INEC.2010.5425068

7. A. S. G. Khalil, S. Hartner; M. Ali, **A. Gupta**, H. Wiggers and M. Winterer

   Stable aqueous dispersions of ZnO nanoparticles for ink-jet printed gas sensors.

   3rd International Nanoelectronics Conference (INEC), 2010, pp. 440 – 441.

   DOI: 10.1109/INEC.2010.5424503

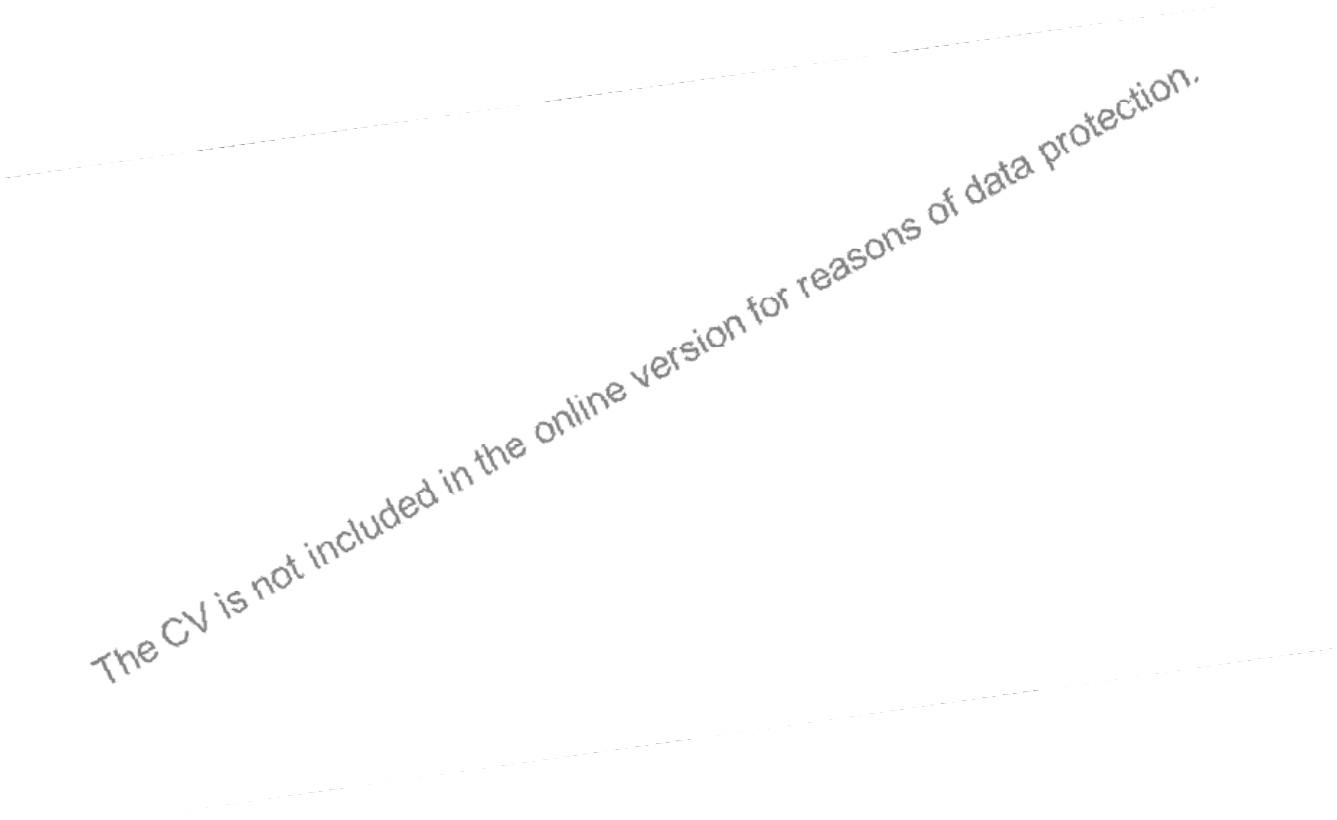
The CV is not included in the online version for reasons of data protection.